

Aus dem Josef Lissner Laboratory for Biomedical Imaging
des Instituts für Klinische Radiologie
der Ludwig-Maximilians-Universität München

Direktor: Prof. Dr. med. Dr. h.c. Maximilian F. Reiser, FACR, FRCR

Quantitative Analysis of Diffusion-weighted Magnetic Resonance Imaging in the Spine

Dissertation zum Erwerb des Doktorgrades der Humanbiologie an der
Medizinischen Fakultät der Ludwig-Maximilians-Universität zu München

vorgelegt von
Andreas Ferdinand Biffar
aus
Heidelberg (Deutschland)

2010

Mit Genehmigung der Medizinischen Fakultät der Universität München

Berichterstatter:

Prof. Dr. med. Dr. h.c. Maximilian F. Reiser, FACR, FRCR

2. Berichterstatter:

Prof. Dr. Manfred Seiderer

Mitberichterstatter:

Prof. Dr. Volkmar Jansson

Prof. Dr. Axel Stäbler

Mitbetreuung durch die promovierten Mitarbeiter:

Prof. Dr. med. Dr. h.c. Maximilian F. Reiser, FACR, FRCR

PD Dr. med. Andrea Baur-Melnyk

Dr. rer. nat. Olaf Dietrich

Dekan:

Prof. Dr. med. Dr. h.c. Maximilian F. Reiser, FACR, FRCR

Tag der mündlichen Prüfung:

17.12.2010

Contents

1	Introduction	1
2	The Spine	5
2.1	Vertebrae	6
2.2	Bone Marrow	8
2.3	Intervertebral Disc	9
2.4	Vertebral Compression Fractures	10
2.5	MRI of the Spine	12
3	Diffusion-Weighted Imaging – DWI	17
3.1	Diffusion – Theoretical Background	17
3.2	Diffusion-weighted Imaging	22
3.2.1	Derivation of the DWI Signal	22
3.3	Applications of DWI	27
3.3.1	Pulse Sequences	27
3.3.2	DWI of the Brain	28
3.3.3	DWI of the Body	31
4	MR Signal Theory	37
4.1	Gradient-Echo Signal	37
4.2	Spoiled Gradient Echo	40
4.3	Steady-state Free Precession	41
4.3.1	SSFP-FID and SSFP-Echo	41
4.3.2	Balanced SSFP Sequence	51
4.4	Formation of the SSFP Signal in the Presence of Diffusion	51
5	DW-SSFP in Vertebral Fractures	65
5.1	Patient Collective	66
5.2	Morphological Imaging	67

5.3	T_1 Quantification	68
5.4	T_2 Quantification	73
5.5	T_2^* Quantification	77
5.6	ADC Quantification	79
5.7	Fat and Water Quantification	83
5.8	Signal Simulations	94
5.9	Signal Analysis	105
6	Summary	119
	Zusammenfassung	123
	Bibliography	138
	Curriculum Vitae	139
	Danksagung	143

Chapter 1

Introduction

Acute vertebral fractures are a common clinical finding in elderly patients with an estimated incidence of 1.4 million cases in Europe in 2000 [1]; a 50-year-old woman has a 16 % lifetime risk of experiencing a vertebral fracture [2]. Vertebral fractures occur when a vertebral body breaks in an area that is weakened by another disease process. Osteoporosis and osseous tumors (primary and metastatic) are the two most common causes of weakened bone leading to vertebral fractures. The majority of the vertebral fractures is caused by osteoporosis. In 2003, 7.8 million Germans (6.5 million women) were affected by osteoporosis. Of them, 4.3 % experienced at least one clinical fracture and only 21.7 % were treated with an antiosteoporotic drug. The total direct costs attributable to osteoporosis amounted to €5.4 billion [3]. In patients with an underlying malignant disease, vertebral metastases can be found in 5 to 10 % of all cases [4]. This subject becomes even more involved considering the fact that 10 % of the vertebral fractures detected in patients with osteoporosis are of malignant origin. On the other hand, 25 % of the fractures in patients with a known malignancy are of osteoporotic origin [5, 6].

One of the most important imaging techniques to examine vertebral fractures in clinical practice is magnetic resonance imaging (MRI). Yet, the differential diagnosis between an osteoporotic or malignant origin of vertebral fractures based on the contrast of conventional MRI sequences is a complicated task. Both entities are characterized by an easily confusable appearance on MR images, i.e. a hypointense signal on T_1 -weighted images and a hyperintense signal on T_2 -weighted or STIR images. Hence, a differentiation between both entities is often only possible by means of their morphological appearance. However, these distinguishing attributes are not always sufficiently pronounced to permit a definite diagnosis [7, 8, 9]. In the past, it was shown, that the application of diffusion-weighted MRI (DWI) in the spine presents

a promising technique to differentiate between benign osteoporotic and malignant lesions.

In general, DWI provides a contrast that reflects the degree of self-diffusion of water molecules in a tissue. Since the beginning of the 1990's, DWI has been successfully applied for the early diagnosis of ischemia in the central nervous system (CNS) [10, 11]. Outside of the CNS, the application of DWI is more challenging and only during recent years the emergence of improved MRI systems and faster imaging pulse sequences has led to an intensified use of DWI outside of the brain. A brief review of DWI with a special focus on DWI in the body is given in chapter 3. In the case of vertebral fractures, it was shown qualitatively [12, 13, 14] as well as quantitatively [15, 16, 17] that based on the different diffusion characteristics of benign and malignant lesions a differential diagnosis might be possible. The diffusion coefficients in lesions caused by malignant infiltrations are significantly lower than in benign osteoporotic lesions. This difference can be explained by the structure of the cancerous tissue, containing a dense network of tumor cells, which restricts the self-diffusion of the water molecules. In benign lesions the interstitial volume in the edema is expected to be increased, leading to an increase of the self-diffusion in the lesion.

A sequence type used for DWI that has been shown to be extremely valuable for the differential diagnosis of vertebral compression fractures is a particular type of a diffusion-weighted steady state free precession sequence, the DW-PSIF sequence [12]. In contrast to a simple diffusion-weighted spin echo sequence, the signal of the DW-PSIF sequence is a combination of many echoes with different diffusion sensitivities. Thus, the diffusion weighting of the DW-PSIF sequence cannot easily be determined, but depends on the relaxation times, T_1 , T_2 and T_2^* , and on the sequence parameters. This makes the exact quantification of the apparent diffusion coefficient very difficult and to date a complete understanding of the underlying signal mechanism is lacking. Contradictory results have been published with regard to the qualitative assessment of the DW-PSIF sequence in the spine [18, 19]. In contrast to most other tissues in the human body, the signal in vertebral bodies is not dominated by a single proton component, but represents a mixture of a fat and a water signal, which are of the same order of magnitude. Hence, the diffusion-weighted signal in vertebral bodies is very sensitive to the exact distribution pattern of its constituents and the setting of the sequence parameters. In order to understand the signal mechanism of the DW-PSIF sequence in fractured and non-fractured vertebral bodies it is necessary to determine the relaxation times and diffusion coefficients of both components as well as the fat and water fraction.

The aim of this thesis was to study the signal behavior of the DW-PSIF sequence

in vertebral fractures and to decode the complex mechanism responsible for the observed contrast, that permits an excellent differential diagnosis between benign and malignant lesions. As a first step, the theoretical derivation of the signal function of the DW-PSIF sequence is briefly reviewed, see chapter 4. Using the signal function of the DW-PSIF, signal simulations are performed to investigate the sensitivity of the signal to the various physical as well as to the sequence parameters.

In chapter 5 we try to understand the actually measured DW-PSIF signal in the spine using the model derived before. In a patient collective of 40 patients with malignant and benign osteoporotic vertebral fractures all parameters relevant for the DW-PSIF signal are quantified. Since the signal is a combination of the fat and water signal, all parameters are determined for both components separately.

Based on these measurements, the signal in both types of lesions and in normal-appearing vertebral bone marrow is simulated. DW-PSIF measurements are compared with the simulations to verify the theoretical results in-vivo and to identify the main factors responsible for the observed contrast on DW-PSIF images.

Chapter 2

The Spine

The spine or vertebral column is located in the dorsal part of the torso. It consists of vertebrae, the sacrum and the intervertebral discs. It has the following important functions:

- It serves as a support for the torso. Since the body load increases from the cervical to the lumbar part, the vertebral bodies become wider and thicker in the lower part of the spine.
- The intervertebral discs located between the vertebral bodies balance the pressure that acts on them due to the body weight.
- The vertebral column as a whole entity allows moving the torso in different directions.
- Within the vertebral column resides the spinal canal containing the spinal cord, which is thus protected against injuries from outside.

The composition of the spine is formed by the vertebrae which are stacked upon each other and separated by the intervertebral discs. There are four regions of the spine, see Fig. 2.1:

- cervical (neck)
- thoracic (chest/trunk)
- lumbar (lower back)
- sacral (pelvic)

The cervical spine is made up of seven cervical vertebrae. The main function of the cervical spine is to support the weight of the head. The cervical spine has the greatest range of motion, partly because of two specialized vertebrae, the atlas and the axis, that move with the skull. Cervical vertebrae are the smallest of the vertebrae.

The main function of the thoracic spine together with the ribs is to protect the organs of the chest, especially the heart and lung. It consists of 12 thoracic vertebrae with one rib attached on both sides of each of them, to create a thoracic cage.

The lumbar spine has five lumbar vertebrae. The lumbar vertebral bodies are the weight-bearing portion of the spine and are the largest in diameter compared to the thoracic and cervical vertebral bodies. They sit atop the sacrum, which is formed by five vertebrae, which are fused together into a solid unit. There are usually no identifiable disc spaces between the sacral segments. Most people have 33 vertebrae in total, although there may be 32 or 34. Variations are usually found in the lumbar or sacral regions.

2.1 Vertebrae

Every vertebra is characterized by unique features, depending on the region where it is located. Each vertebra, regardless of location, consists of three basic functional parts: (1) the drum-shaped vertebral body, designed to bear weight and withstand compression or loading; (2) the posterior (backside) arch, made of the lamina, pedicles and facet joints; and (3) the transverse processes, to which the muscles attach. An anatomical image of the 5th lumbar vertebra is shown in Fig. 2.2. The vertebral body

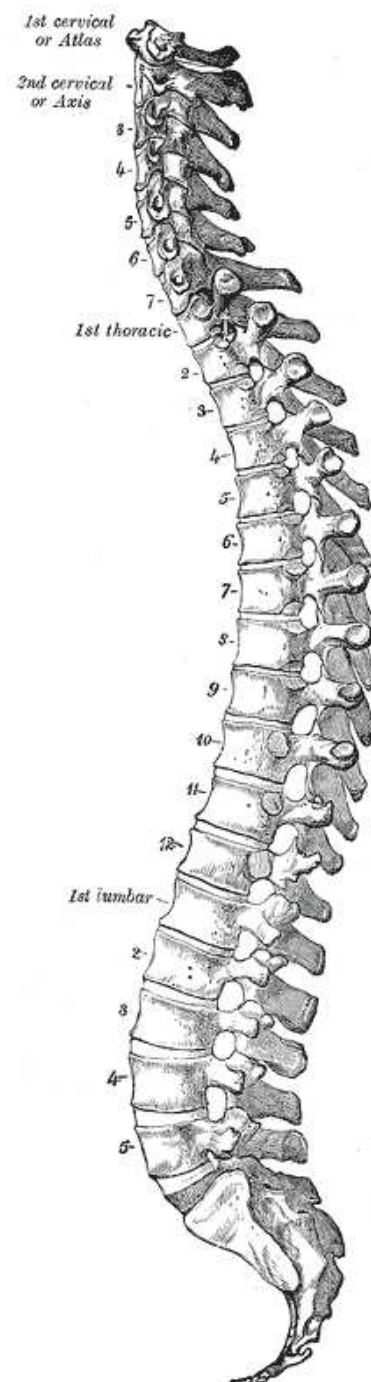
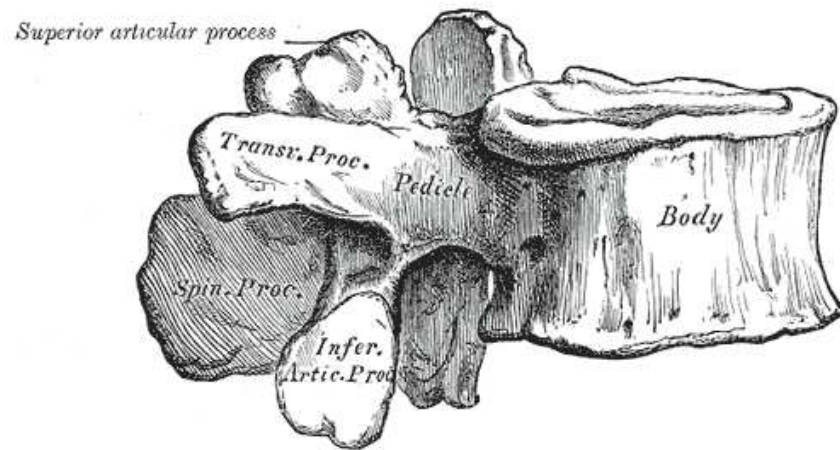
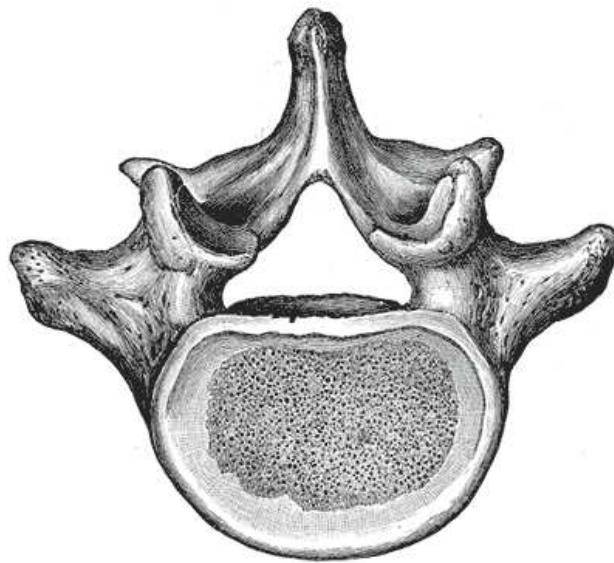


Figure 2.1: Sagittal view of the vertebral column (taken from Gray's Anatomy).



(a) Side view



(b) Top view

Figure 2.2: 5th lumbar vertebral body (taken from Gray's Anatomy).

is composed of hard cortical bone on the outside and less dense cancellous bone, the spongiosa, on the inside. The cancellous bone structurally resembles a honeycomb and accounts for about 20 % of bone matter in the human body, see Fig. 2.5. It can be classified as a porous cellular solid, consisting of an irregular three-dimensional array of bony rods, called trabeculae. Within the cancellous bone resides the bone marrow [20, 21]. Bone marrow occupies approximately 85 % of the bone cavity, while the rest is filled by the trabeculae, see Fig. 2.3. Trabecular bone is not as strong as compact bone. It is somewhat more flexible and useful in bones that are jointed. Primarily, however, trabecular bone protects the bone marrow, where the hematopoiesis occurs. The top and bottom of the vertebral body are called the end plates. The intervertebral disc lying between two vertebral bodies is attached to the end plates.

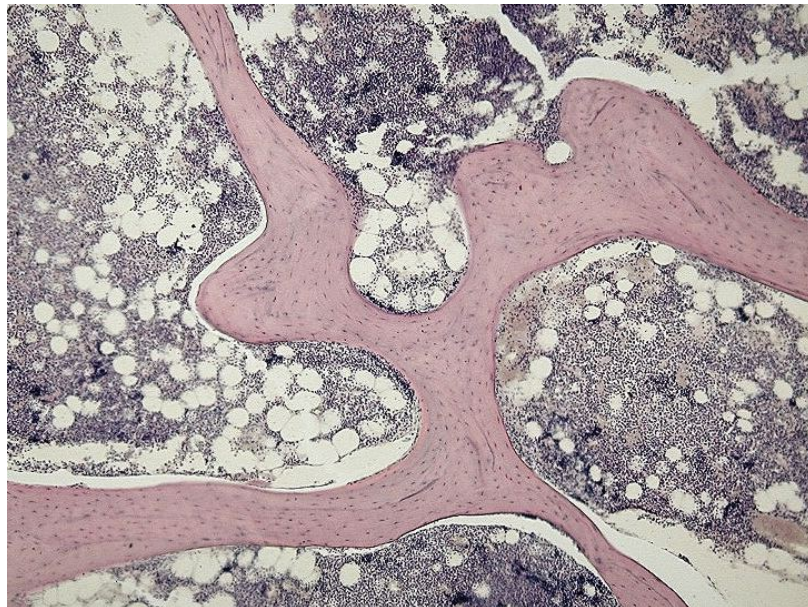


Figure 2.3: Microscopic view of a histological specimen of normal bone marrow.

2.2 Bone Marrow

Bone marrow is a richly cellular connective tissue. The blood cells, namely red cells, thrombocytes and white cells, form there and enter the circulation, to provide tissue oxygenation, coagulation and immunity. It is divided into two main constituents, yellow and red marrow. “Yellow marrow” is considered as hematopoietically inactive. It is mainly composed of fat cells (95 %) and its substantial composition consists of 80 % fat, 15 % water and 5 % proteins. The vascular network of yellow marrow is

sparse and consists of few capillaries, venules and thin-walled veins. “Red marrow”, in contrast, is characterized by a rich sinusoidal system. It contains approximately 60 % hematopoietic cells and 40 % fat cells. Its chemical composition consists of about 40 % water, 40 % fat and 20 % proteins [20]. During growth, conversion of red to yellow marrow occurs following a predictable and orderly pattern. While in the fetus virtually the entire marrow space is made up of red marrow, this changes until a balanced distribution pattern is reached by the age of 25. The exact pattern depends on various factors like sex, age and the health of the individual. At this time the red marrow is concentrated mainly in the axial skeleton and the proximal aspects of the limbs. It has been well demonstrated in vertebral bodies, that the volume of red marrow decreases substantially with age. The increase in fatty marrow is even greater, since with age trabecular bone is decomposed and replaced by fat cells. If a sudden rise in the demand for hematopoiesis of the organism occurs, like low oxygen tension, a reconversion of yellow to red marrow takes place.

2.3 Intervertebral Disc

The intervertebral disc (iVD) is located between the vertebral bodies. It is a complex structure that bears the weight of the body and, with the facet joints, permits a significant range of motion. The disc is mainly made up of fibrocartilage and has two parts: the nucleus pulposus and the annulus fibrosus. The nucleus pulposus is a gel-like material located in the center of the disc. It has a high water content, and thus acts as a cushion, distributing loads onto the vertebral body end plates and to the annulus. The water content of the nucleus decreases with age. In an adult the healthy disc has no blood supply of its own and is supplied with nutrients via diffusion from the vertebral body. The annulus fibrosus is the outer portion of the disc. The annulus comprises 15 to 20 collagenous (type I) laminae, which run obliquely from the edge of one vertebra down to the edge of the vertebra below. The direction of the fibres alternates from lamina to lamina. The inner portion of the annulus is made of fibrocartilage which gradually blends with the nucleus

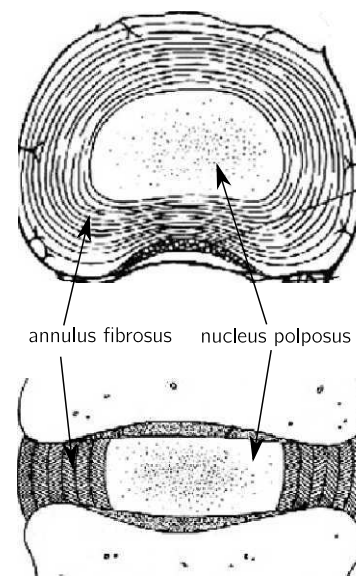


Figure 2.4: Intervertebral disc seen from a transversal and a coronal perspective.

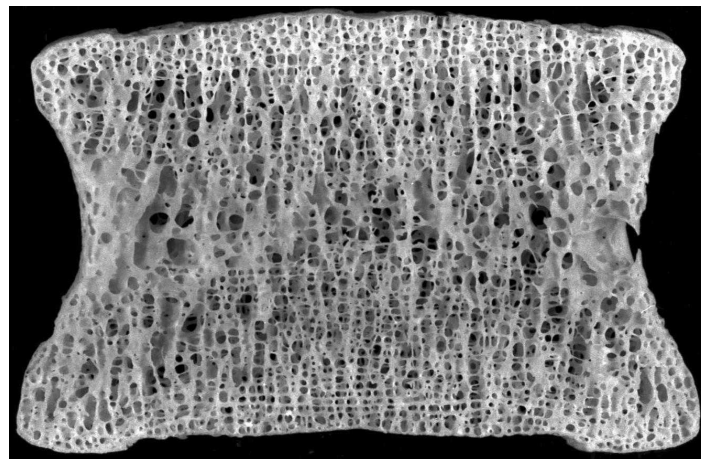
pulposus. Posterolaterally, the annulus is not only thinner, but also has more disorganised collagen bundles, and a greater proportion of vertical fibres. It is the weakest part of the IVD, thus often being the location of disc herniations.

2.4 Vertebral Compression Fractures

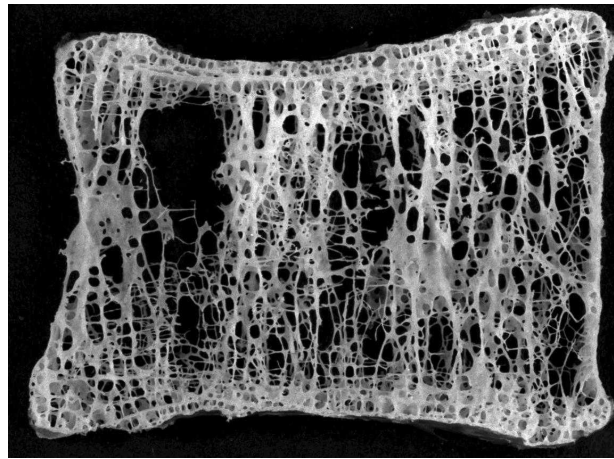
One of the most common clinical findings in the vertebral bodies, especially in elderly people, are vertebral compression fractures (vCF). A vCF usually occurs when the bones of the spine become broken due to trauma. Usually the trauma necessary to break the bones of the spine is quite large. Yet, Under certain circumstances, such as in elderly people and in people with cancer, these bones can break with little or no force. The vertebrae most commonly broken are those in the lower back. In about 75 % of the cases, vCFs are caused by osteoporosis [6]. Osteoporosis is a metabolic bone disease leading to a loss of bone mass, resulting in deterioration of the structure of bones, see Fig. 2.5. The demographic change in the industrialized civilizations leads to an increasing number of osteoporotic compression fractures, showing a considerable impact on the health care system. In 2005, according to the national osteoporosis foundation (NOF)¹, 10 million Americans were estimated to have osteoporosis. Approximately one in two women and one in four men over age 50 will have an osteoporosis related fracture in their remaining lifetime. According to estimated figures, osteoporosis was responsible for more than 2 million fractures in 2005, including 547.000 vCFs. The number of fractures due to osteoporosis is expected to rise to more than 3 million by 2025. In 2005, osteoporosis-related fractures were responsible for an estimated \$19 billion in costs. By 2025, experts predict that these costs will rise to approximately \$25.3 billion.

Another possible cause of vCFs is a malignant infiltration of the vertebral body. The tumor or metastasis destroys the trabecular bone and bone marrow, causing a destabilization of the vertebra that ultimately might lead to a vCF. The prevalence of malignant diseases is increasing with age, and consequently compression fractures caused by tumor or metastasis are a common finding. The most common type of spinal column tumors are metastases and up to 10 % of cancer patients will develop symptomatic secondary spinal lesions, with multiple levels of involvement in 40 to 70 % of symptomatic cancer patients. Typically, these lesions are distributed throughout the skeleton according to the pattern of red marrow prevalence. Thus, the vertebral column is the most common site of vertebral metastases. Cancer from breast, lung, prostate and of renal or hemopoietic origin (multiple myeloma, lymphoma) account

¹<http://www.nof.org/osteoporosis/diseasefacts>



(a) Healthy vertebral body



(b) Osteoporotic vertebral body

Figure 2.5: Microscopic view of the trabecular structure of a healthy and an osteoporotic vertebral body.

for the vast majority of spinal metastases.

The differentiation between a malignant or a benign origin of the vertebral fracture is essential, in order to initiate an appropriate therapy. Furthermore, in many patients a vertebral compression fracture is the initial finding of an unknown primary tumor, and thus, the characterization of a pathological fracture may lead to an early detection of a malignant disease, which is important for proper therapy planning and prognosis.

In addition, this subject becomes more complicated considering the fact, that 10 % of the vCFs detected in patients with osteoporosis are of malignant origin. On the other hand, 25 % of the vCFs in patients with a known malignancy are of osteoporotic origin. This is a frequent cause for the overstaging of a tumor. In

addition, many treatment protocols in oncology lead to manifest osteoporosis and this might also explain the rather high incidence of osteoporotic vCFs in tumor patients. Radiotherapy causes local atrophy of bone and bone marrow, while chemotherapy and hormone therapy induce systemic rarefaction of both trabecular and cortical bone [22]. Thus, tissue characterization of vertebral fractures is essential, which is to date in a lot of cases only possible by histologic means, requiring tissue specimen, which are usually obtained by needle biopsy [23]. It is, however, well known that the accuracy of this procedure is less than 85 %, which is mainly due to sample errors. In addition, the complications following the invasive procedure are a big concern [23, 24].

2.5 MRI of the Spine

In the spine, MRI is the preferred imaging modality for the detection of diseases because of its unique ability to provide an adequate contrast resolution to differentiate the intraspinal soft tissue structures, and reveal spinal cord or canal pathology. It was shown, that MRI is the most sensitive tool with regard to the detection of bone marrow infiltration in comparison to PET, PET/CT and MS-CT [25]. On conventional MR images, the contrast is defined by three properties of the tissue, proton density and the T_1 and T_2 relaxation times [26]. Depending on the chosen sequence, these parameters in combination, or separately, define the resulting image contrast. The standard sequences used in MRI of the spine include T_1 - and T_2 -weighted spin echo (SE) as well as STIR (short TI inversion recovery) fast SE sequences. Another very useful technique is the acquisition of contrast-enhanced T_1 -weighted images, which provide additional information for an improved assessment of intraspinal pathologies or the soft tissue extension of lesions. On T_1 -weighted spin echo images, well hydrated (nondegenerated) discs are hypointense compared to vBM. On T_2 -weighted images, fat saturation is usually recommended, and when used normally, hydrated (nondegenerated) discs will be markedly hyperintense compared to vBM, see Fig. 2.6. These contrasts are explained by the relaxation properties of fat and water protons. Fat protons are contained in hydrophobic CH_2 groups in relatively heavy molecular complexes, which are responsible for a very efficient spin-lattice relaxation, leading to a short T_1 relaxation time [27]. The spin-spin relaxation of fat protons is less efficient, resulting in a relatively long T_2 relaxation time, though not as long as that of water protons [28]. The longitudinal relaxation of water protons is less efficient and the T_1 relaxation time is relatively high. This explains the contrast between the water signal dominated iVD and the fat signal dominated vertebral body. The relaxation times of both components are summarized in the table on the right [29]. The min-

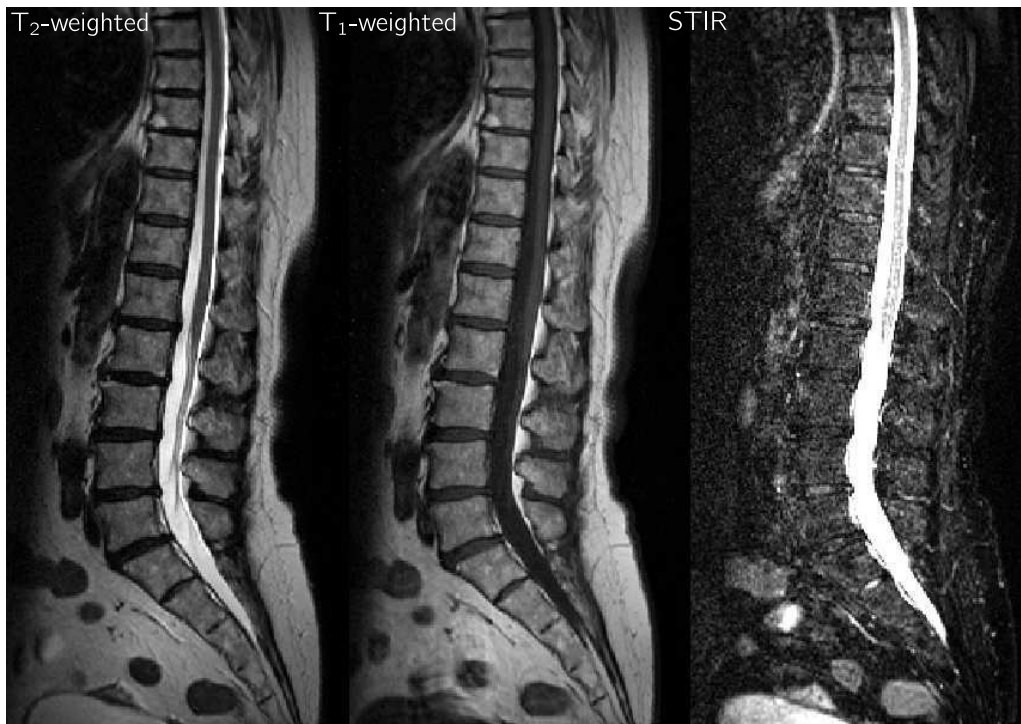


Figure 2.6: Standard sagittal MRI images of the lumbar and thoracic spine acquired with a T2-weighted TSE, a T1-weighted TSE and STIR sequence in a healthy volunteer.

eralized bone has a low density of hydrogen protons, which, moreover, lack mobility within the crystalline structure of bone. Thus the T_1 relaxation time is very long, while the T_2 relaxation time is very short yielding low signal on both T_1 - and T_2 -weighted (SE) images [30]. The composition of the vertebral body can also lead to image artifacts in MRI. Water and fat protons differ in their precession frequencies, at the surface between water- and fat-dominated tissues. These difference, known as the chemical-shift, can lead to a shift in the apparent position of fat protons in the direction of decreasing frequency along the frequency encoding axis [31]. If gradient-echo (GRE) images are acquired, (see section 4.1), the chemical shift is also responsible for the variable signal intensity of red marrow, known as the intravoxel chemical shift effect [32].

The difference in the relaxation times of fat and water protons is also responsible for the different MR appearances of yellow and red marrow. On T_1 -weighted SE images, yellow marrow shows a high signal intensity comparable to that of subcutaneous fat. On T_2 -weighted

Parameter	T_1 [ms]	T_2 [ms]
Water	850	80
Fat	300	120

SE images it has an intermediate, while a high signal intensity on fast SE T_2 -weighted images [33]. On GRE images its signal varies according to the amount of trabecular bone [34]. The signal intensity of yellow marrow on contrast-enhanced images is not expected to change markedly, since only negligible uptake of contrast agent occurs in fatty tissue [35]. Red marrow has a lower signal intensity than yellow marrow on T_1 -weighted SE images, but the signal intensity is generally higher than that of muscles and intervertebral discs [36]. On T_2 -weighted SE images red marrow, in general, has a lower signal intensity than yellow marrow, but the difference is smaller than on T_1 -weighted SE images. On STIR as well as on fat-saturated SE images red marrow has a higher signal intensity than yellow marrow. On gradient echo images the signal intensity depends strongly on the chosen value of the echo time T_E . Since red marrow contains almost equal fractions of fat and water protons, the net signal difference, which corresponds to the signal on opposed phase images where the magnetizations of fat and water are oppositely oriented, is close to zero. On contrast-enhanced images the T_1 relaxation time of red marrow equals more or less that of yellow marrow. Hence, only very careful measurements of signal intensities can depict the bone marrow blood supply [37].

With conventional imaging techniques including MRI, CT, radiographs, PET, and scintigraphy, it is often difficult or even impossible to distinguish malignant from osteoporotic or posttraumatic fractures [7, 5, 38, 39, 40, 41]. Vertebral metastases or tumors can be well depicted on T_1 -weighted images because of the natural contrast between the bright appearing fatty bone marrow (low T_1 relaxation time) and the darker tumor tissue on T_1 -weighted images [42]. Furthermore, they can be seen as enhancing regions on fat-saturated contrast-enhanced T_1 -weighted images, depending on the vascularity of the underlying pathological process [20, 43]. Unfortunately, this contrast can also be found in patients with increased blood neogenesis, where edema and red marrow replace the regular adult bone marrow [44]. In Fig. 2.7, conventional MR images acquired with a T_1 -weighted turbo spin-echo (TSE) and a STIR sequence in a patient with a benign osteoporotic and a patient with a malignant vCF are shown. The vCFs appears hypointense on the T_1 -weighted and hyperintense on the STIR images in both pathologies. The differentiation between benign osteoporotic and malignant vCFs can thus be very complicated on morphological images. The analysis of contrast mechanisms like diffusion, see section 3, enables the investigation of certain aspects of bone physiology. Their analysis might provide important new insight into the pathogenesis of certain bone-marrow diseases, like vCFs. Hence, they can potentially serve as a supplementary tool to differentiate benign and malignant lesions. The analysis of diffusion-weighted imaging in the spine, focussing on vCFs,



(a) Patient with an osteoporotic vCF in T7



(b) Patient with a malignant vCF in T7

Figure 2.7: Sagittal images of vCFs (indicated with arrows) acquired with a T_1 -weighted TSE sequence (left side) and a STIR sequence (right side).

will be the main topic of this thesis.

Chapter 3

Diffusion-Weighted Imaging – DWI

In this chapter, we first summarize the derivation of a general model of diffusion. Afterwards, we analyze the effect of the self-diffusion of the protons on the MR signal. We show how the self-diffusion can be measured using diffusion-sensitizing gradients during the MR imaging process. Finally, we review the most prominent sequences used for diffusion-weighted MRI and talk about their applications in clinical imaging, focusing on the brain and the musculoskeletal system.

3.1 Diffusion – Theoretical Background

Diffusion is a process describing the statistical distribution of a given entity in space, e.g. concentration or heat, caused by the random motion of small objects (atom, molecules, charges). Since the motion is random the movement at one moment in time cannot be correlated to the movement at any other moment in time. Hence, diffusion causes a statistical distribution of these entities in space. The diffusion coefficient is a macroscopic measure of the particle diffusion. It is usually measured in terms of the flux of a tracer caused by a concentration gradient. In the case of MRI, the diffusion-weighted contrast on the images is caused by the self-diffusion of the water molecules.

Diffusion can be understood either on a macroscopic or a molecular level. Both descriptions should be equal at large scales and long measurement times. On the macroscopic level diffusion is governed by the diffusion equation (Fick's 2nd law of

diffusion)

$$\frac{\partial c(\mathbf{r}, t)}{\partial t} = D \nabla^2 c(\mathbf{r}, t). \quad (3.1)$$

D is the diffusion coefficient, describing the relationship between the temporal and spatial evolution of the concentration. In Eq. (3.1) we assume that the diffusion coefficient is constant and a scalar, i.e. isotropic diffusion. The diffusion equation can also be used to analyze experiments involving self-diffusion. The diffusion equation can be solved if the $c(\mathbf{r}, t)$ is known for all \mathbf{r} at one t . Of particular interest is for example the case of an initial delta function variation of the concentration. In this case at $t = 0$ we have

$$c(\mathbf{r}, 0) = A \delta(\mathbf{r}) \quad (3.2)$$

and all concentration is located at the origin. The solution of Eq. (3.1) is given by

$$c(\mathbf{r}, t) = A \left(\frac{1}{4\pi Dt} \right)^{3/2} \exp(-\mathbf{r} \cdot \mathbf{r} / (4Dt)). \quad (3.3)$$

The concentration located at the origin spreads out with time. The maximum is always at the origin, but it extends farther as time goes on, as can be seen in Fig. 3.1. Using Eq. (3.3), the average vector distance traveled between time 0 and t can be calculated

$$\bar{\mathbf{r}} = \frac{\int d\mathbf{r} c(\mathbf{r}, t) \mathbf{r}}{\int d\mathbf{r} c(\mathbf{r}, t)} = 0. \quad (3.4)$$

The mean square displacement, or the average of the square of the distance traveled by a molecule in 3 dimensions

$$\overline{\mathbf{r} \cdot \mathbf{r}} = \overline{r^2(t)} = \frac{\int d\mathbf{r} c(\mathbf{r}, t) \mathbf{r} \cdot \mathbf{r}}{\int d\mathbf{r} c(\mathbf{r}, t)} = 6 \cdot D \cdot t. \quad (3.5)$$

It can be seen in Eq. (3.5), that for a molecule to travel over a distance of order L due to diffusion on average it takes an amount of time proportional to L^2 .

The observation in 1827 of the irregular motion of small particles immersed in a fluid, the so-called Brownian motion, played almost no role in physics when the kinetic theory of gases and the diffusion equation was developed. In 1905, Einstein [45] and independently in 1906 Smoluchowski [46] showed theoretically that an explanation

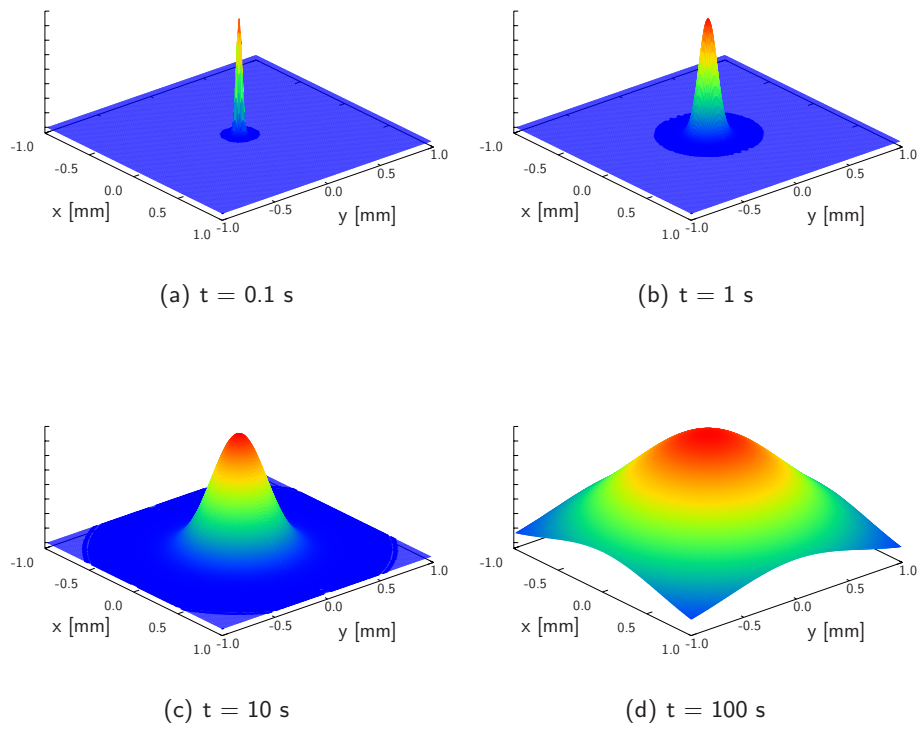


Figure 3.1: Distribution of $c(\mathbf{r}, t)$ in eq. (3.3) as a function of time in 2 dimensions. The scale of $c(\mathbf{r}, t)$ is decreased by a factor of $1/10$ for each increase of t by a factor of 10. The diffusion coefficient was set to $0.002 \text{ mm}^2/\text{s}$.

of the Brownian motion based on kinetic theory shows that diffusion is the result of Brownian motion. Einstein approached the problem of diffusion in two different manners. Firstly, he assumed that Brownian particles are in thermal equilibrium and the osmotic pressure is then given by the ideal gas equation

$$p = \frac{RT}{N} c, \quad (3.6)$$

where c is the concentration, T the temperature in Kelvin, N is Avogadro's number and R is the gas constant. The particles are diffusing in the liquid in such way, that the osmotic force originating from a concentration gradient is balanced by the viscous force, slowing the motion of the particles according to hydrodynamics. The viscous force F_c is proportional to the pressure gradient

$$F_c = \frac{\partial p}{\partial x}, \quad (3.7)$$

and using Eq. (3.6) we get

$$F_c = \frac{RT}{N} \frac{\partial c}{\partial x}. \quad (3.8)$$

Using Stokes formula for the velocity, v , of a particle moving through a viscous medium

$$F = 6\pi a \eta v, \quad (3.9)$$

where a is the radius of the particle and η the coefficient of dynamical viscosity, the force F can be eliminated

$$6\pi a \eta v c = \frac{RT}{N} \frac{\partial c}{\partial x}. \quad (3.10)$$

In Eq. (3.9) it can be seen, that $cF/6\pi a \eta$ corresponds to the number of particles crossing a unit area per unit time. This can be equated to $-D(\partial c/\partial x)$ according to Fick's law. This leads to Einstein's second equation

$$\frac{F_c}{6\pi a \eta} = D \frac{\partial c}{\partial x}, \quad (3.11)$$

and hence, using Eq. (3.8) the diffusion coefficient can be expressed as

$$D = \frac{RT}{N} \frac{1}{6\pi a \eta}. \quad (3.12)$$

Combining Eq. (3.5) and Eq. (3.12), we get for the mean square displacement of a Brownian particle

$$\sigma = \sqrt{t} \sqrt{\frac{kT}{\pi a \eta}}, \quad (3.13)$$

where we used $k = R/N$.

Einstein connected this theory with the “irregular movement which arises from thermal molecular movement”, making the following assumptions

1. the motion of each particle is independent of the others
2. the movements of one and the same particle after different intervals of time are considered to be independent processes, as long as the consecutive time interval is not chosen too small.

Under these conditions, the particles behave according to a continuous-time stochastic process, named Wiener process, which corresponds to a random walk in the limit of very small steps, see Fig. 3.2. If we assume to observe each particle at time points $\tau, 2\tau, \dots$ the number of particles whose displacement lies between Δ and $\Delta + d\Delta$ corresponds to

$$dn = n\phi(\Delta)d\Delta, \quad (3.14)$$

where

$$\int_{-\infty}^{\infty} \phi(\Delta)d\Delta = 1, \quad \phi(\Delta) = \phi(-\Delta), \quad (3.15)$$

n is the total number of particles, and the distribution function ϕ is only different from zero for small values of Δ . $\phi(\Delta)$ is defined effectively by Eq. (3.14) and describes the probability distribution of the displacements. In one dimension, the value of the concentration $c(x, t)$ after the time τ has elapsed is then given by

$$c(x, t + \tau) = \int_{-\infty}^{\infty} c(x + \Delta, t)\phi(\Delta)d\Delta. \quad (3.16)$$

For small τ and Δ , $c(x, t)$ can be expanded as a Taylor series

$$\begin{aligned} c(x, t) + \frac{\partial c(x, t)}{\partial t} \tau + \dots = c(x, t) \int_{-\infty}^{\infty} \phi(\Delta) d\Delta + \frac{\partial c(x, t)}{\partial x} \int_{-\infty}^{\infty} \Delta \phi(\Delta) d\Delta \\ + \frac{\partial^2 c(x, t)}{\partial x^2} \int_{-\infty}^{\infty} \frac{\Delta^2}{2} \phi(\Delta) d\Delta + \dots \end{aligned} \quad (3.17)$$

Using Eq. (3.15) and neglecting higher order terms, this can be simplified to

$$\frac{\partial c(x, t)}{\partial t} = D \frac{\partial^2 c(x, t)}{\partial x^2}, \quad (3.18)$$

where

$$D = \frac{1}{\tau} \int_{-\infty}^{\infty} \frac{\Delta^2}{2} \phi(\Delta) d\Delta. \quad (3.19)$$

Eq. (3.18) is equal to the diffusion equation in Eq. (3.1).

3.2 Diffusion-weighted Imaging

3.2.1 Derivation of the DWI Signal

In DWI, the process which is measured, is the self-diffusion of water, and the moving entities are water molecules. Before the emergence of nuclear magnetic resonance (NMR), the self diffusion of water was measured using heavy water as a tracer. Diffusion was measured in phantoms, containing deuterium [47] or tritium [48], based on density measurements. However, the presence of the tracer might alter the diffusion characteristics of the normal water. In contrast, in DWI the water molecules are in effect labeled by the phase angle of the nuclear magnetic moment, as pointed out by Carr et al. [49] “a more innocuous label would be difficult to imagine”. Hahn was the first to describe, that the presence of a magnetic field gradient during a magnetic resonance spin-echo experiment results in a signal attenuation due to the molecular diffusion of the spins [50]. In 1954, Carr and Purcell [49] showed that the self-diffusion coefficient could be determined using a SE sequence applying a field gradient during the whole imaging process. Based on a random walk model for the movement of the spins, they showed that the transversal magnetization in a spin-echo measurement

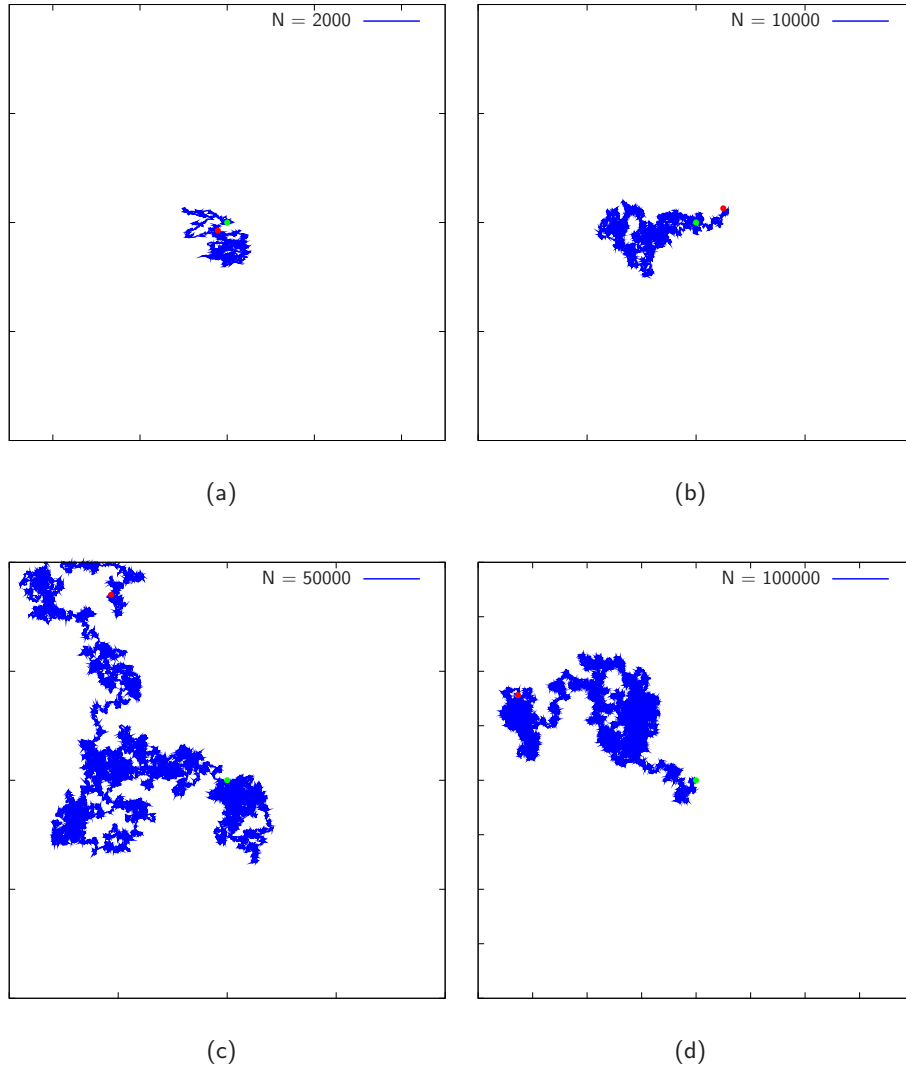


Figure 3.2: Simulation of the isotropic diffusion path of a water molecule as a random walk with (a) 2000, (b) 10000, (c) 50000 and (d) 100000 steps. The green point corresponds to the origin and the red point to the end of the simulation. In plot (d) the scale of the axes has been increased by a factor of 2.

evolves as follows

$$M_{\perp}(t) = M_0 \exp \left[(-t/T_2) + (-\gamma^2 G^2 D t^3 / 12) \right]. \quad (3.20)$$

They performed a first measurement of the diffusion coefficient of water at 25° and obtained a value of $D = 2.5 (\pm 0.3) \times 10^{-3} \text{ mm}^2/\text{s}$. This method had strong experimental limitations, since the magnetic field gradient, causing the diffusion weighting,

was present during the whole spin-echo measurement. Therefore an increase of the gradient strength, necessary to measure smaller and smaller values of the diffusion coefficient, also increases the linewidth of the nuclear magnetic resonance, causing a decrease of the amplitude of the echo after the 180° pulse. Furthermore, for measurements of anisotropic diffusion coefficients, e.g. if diffusion is restricted by barriers such as cell membranes, it is desirable to precisely fix the period during which diffusion is observed and to keep it as short as possible. In order to overcome these limitations, Stejskal and Tanner, in 1965 [51], developed the concept of using a pair of pulsed field gradients. Thus, the gradient is switched off during the application of the RF pulses and can be arbitrarily large at other times.

The theoretical description of the evolution of the magnetization in the presence of diffusion was given by Torrey [52] in terms of the so-called Bloch-Torrey equations. Following the notation of Abragam [53], the magnetization in the presence of diffusion is given by:

$$\frac{\partial \vec{M}(\vec{r}, t)}{\partial t} = \gamma \vec{M} \times \vec{H}(\vec{r}, t) - \frac{M_x \vec{i}' + M_y \vec{j}'}{T_2} - \frac{M_z - M_0}{T_1} \vec{k}' + D \nabla^2 \vec{M}, \quad (3.21)$$

where \vec{i}' , \vec{j}' and \vec{k}' are the unit vectors in x-, y- and z-direction. The extra term $D \nabla^2 \vec{M}$ represents the contribution of the diffusion to the rate of change of the magnetization considered as a macroscopic fluid, behaving according to Eq. (3.1). In the presence of a diffusion gradient, the static magnetic field vector is given by

$$B_z = B_0 + \vec{G} \cdot \vec{r}, \quad (3.22)$$

where the vector \vec{G} is assumed to be constant through the sample. The evolution of the transverse magnetization $M_\perp = M_x + iM_y$ in the absence of an RF pulse is then given by

$$\frac{\partial M_\perp}{\partial t} = -i\omega_0 M_\perp - \frac{M_\perp}{T_2} - i\gamma(\vec{G} \cdot \vec{r}) M_\perp + D \nabla^2 M_\perp. \quad (3.23)$$

Introducing $\Psi(\vec{r}, t)$ through $M_\perp = \Psi \exp(-(i\omega_0 t - t/T_2))$, we get

$$\frac{\partial \Psi}{\partial t} = -i\gamma(\vec{G} \cdot \vec{r}) \Psi + D \nabla^2 \Psi. \quad (3.24)$$

In the absence of the diffusion term, the solution of Eq. (3.24) is given by

$$\Psi = A \exp(-i\gamma \vec{r} \cdot \vec{F}), \quad (3.25)$$

with the boundary condition that $\Psi = A$ immediately following the 90° pulse and

$$\vec{F}(t) = \int_0^t \vec{G}(t') dt'. \quad (3.26)$$

After the 180° pulse, at time $t = \tau$, the phase is inverted and therefore it follows

$$\Psi = A \exp \left[-i\gamma \vec{r} \cdot (\vec{F} - 2\vec{f}) \right], \quad (3.27)$$

where $\vec{f} = \vec{F}(\tau)$. This can be written in a single expression

$$\Psi = A \exp \left\{ -i\gamma \vec{r} \cdot \left[\vec{F} + (\xi - 1)\vec{f} \right] \right\}, \quad (3.28)$$

where

$$\xi = +1 \quad \text{for} \quad 0 < t < \tau \quad (3.29)$$

$$\xi = -1 \quad \text{for} \quad t > \tau \quad (3.30)$$

and we assume that $\Psi(2\tau) = A$. Taking diffusion into account we set $A \rightarrow A(t)$. Substituting Eq. (3.25) into Eq. (3.24) yields

$$\frac{\partial A(t)}{\partial t} = -\gamma^2 D \left[\vec{F} + (\xi - 1)\vec{f} \right]^2 A(t). \quad (3.31)$$

Integration of both sides yields

$$\ln \left[\frac{A(t)}{A(0)} \right] = -D\gamma^2 \left[\int_0^t F^2 dt - 4\vec{f} \cdot \int_\tau^t \vec{F} dt + 4f^2(t - \tau) \right]. \quad (3.32)$$

Eq. (3.32) can now be solved depending on the specific function for $\vec{G}(t)$. In the case of a diffusion-weighted spin-echo sequence as shown in Fig. 3.3 the solution can be calculated assuming for $\vec{G}(t)$:

$$\begin{aligned} \vec{G}(t) &= 0 & \text{when} \quad 0 < t < t_1 \\ \vec{G}(t) &= -g_D & \text{when} \quad t_1 < t < t_1 + \delta < \tau \\ \vec{G}(t) &= 0 & \text{when} \quad t_1 + \delta < t < t_1 + \Delta > \tau \\ \vec{G}(t) &= -g_D & \text{when} \quad t_1 + \Delta < t < t_1 + \Delta + \delta < 2\tau \\ \vec{G}(t) &= 0 & \text{when} \quad t_1 + \delta + \delta < t. \end{aligned}$$

The first gradient pulse occurs at time t_1 and the second at time $t_1 + \Delta$. Furthermore, we have assumed that the effects of field inhomogeneities and the slice selection gradient are negligible. The echo occurs at $t = 2\tau$ and the amplitude can be derived by plugging $\vec{G}(t)$ into Eq. (3.32):

$$\ln A_0 = -D\gamma^2 G^2 \delta^2 \left(\Delta - \frac{1}{3}\delta \right). \quad (3.33)$$

Assuming that $\Delta = \delta = \tau$, it can be seen, that this corresponds to the result of Carr and Purcell in Eq. (3.20) for $t = 2\tau$. Another possibility would be to apply a

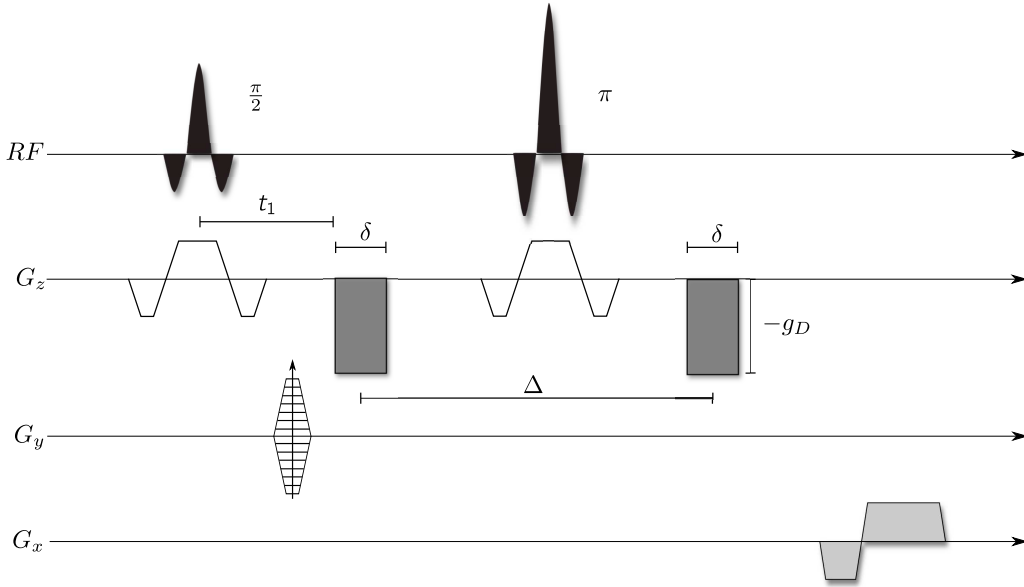


Figure 3.3: Conventional "Stejskal-Tanner" spin-echo pulse sequence with the slice selection and diffusion sensitive gradient applied along the same physical dimension.

bipolar gradient pulse between the RF excitation pulse and the read-out gradient in a gradient-echo sequence. Assuming a simple bipolar pulse of duration $2\tau_b$ (i.e., of amplitude G for $0 \leq t < \tau_b$ and amplitude $-G$ for $\tau_b \leq t < 2\tau_b$), it follows

$$\int_0^{t''} \mathbf{G}(t') dt' = \begin{cases} G t'' & \text{for } t'' < \tau_b \\ -G(t'' - 2\tau_b) & \text{for } \tau_b < t'' < 2\tau_b. \end{cases} \quad (3.34)$$

Plugging this into Eq. (3.32), we get for $t = 2\tau_b$

$$\ln A_0(2\tau_b) = -D\gamma^2 \int_0^{\tau_b} G^2 t'^2 dt' - D\gamma^2 \int_{\tau_b}^{2\tau_b} G^2 (t'' - 2\tau_b)^2 dt''. \quad (3.35)$$

Applying a change of variables in the second integral to $u = 2\tau_b - t''$, the second integration is equal to the first and the solution is given by

$$\ln A_0(2\tau_b) = -\frac{2}{3}D\gamma^2 G^2 \tau_b^3. \quad (3.36)$$

The reversed gradient causes the spins to reset their dephasing at the echo as the refocusing pulse in the spin echo case. The diffusion coefficient measured in DWI is usually referred to as the apparent diffusion coefficient (ADC).

3.3 Applications of DWI

3.3.1 Pulse Sequences

In general, almost every type of pulse sequence can be modified for DWI by insertion of additional diffusion-sensitizing gradients. The most important sequences used nowadays for DWI will be briefly reviewed. An extensive overview was given by Dietrich et al. [54].

SE and STE sequences: Historically, DWI was first performed with stimulated-echo and spin-echo pulse sequences [55, 56, 57]. These sequences have the disadvantage, that they require very long acquisition times, which causes a very high sensitivity to motional artifacts.

Echo-planar imaging (EPI) sequences: Today, the standard sequence used in DWI is the single-shot echo planar imaging sequence (EPI) [58]. Due to the very fast read-out – an entire slice is acquired within about 100 ms – this sequence is less sensitive to motional artifacts. However, EPI sequences are very sensitive to B_0 inhomogeneities and susceptibility variations. This limits the application of DW-EPI in the body, especially for structures or organs found in the direct neighborhood of air-filled spaces (e.g., the lungs) or bone-soft-tissue interfaces with substantially different susceptibilities. Furthermore, due to the rapid T_2^* decay that occurs during the acquisition of the gradient-echo train, the spatial resolution is limited to typically 128x128 pixels. Two ways exist to overcome these limitations. Firstly, to increase the

resolution a segmented (or multi-shot) echo-planar readout can be applied, where the acquisition of k-space is divided into several parts, reducing the length of the echo-train per repetition interval. Secondly, the echo-train length can be reduced by the application of parallel imaging techniques. Thus, geometric distortions can be reduced and at the same time the spatial resolution can be increased.

Fast-spin-echo or turbo-spin-echo sequences: The diffusion-weighted single-shot fast-spin-echo (or turbo-spin-echo) sequence acquires a train of spin echoes via the successive application of a series of refocusing pulses after one excitation pulse. Thus, as in the case of the EPI sequence, one image can be acquired in one shot, with acquisition times in the order of 200 - 400 ms per image. These sequences are also known as diffusion-weighted “rapid acquisition with relaxation enhancement” (RARE) or “half-Fourier-acquisition single-shot turbo-spin-echo” (HASTE) sequences [59, 60]. Being very fast, these sequences are relatively insensitive to motion, but provide only limited spatial resolution of typically 128x128 pixels due to the T_2 decay of the signal during the spin-echo train. In contrast to DW-EPI, these sequences are insensitive to susceptibility variations due to the application of the refocusing pulses, and are therefore well suited for DWI of the musculoskeletal system.

SSFP sequences: In section 4.4, we will derive the diffusion-weighted signal of a steady-state free precession (SSFP) sequence. It will be shown, that the signal is a complicated function not only of the ADC as for the other sequences, but also of the relaxation times and sequence parameters. Therefore, the main application of DW-SSFP has been the qualitative evaluation of diffusion-weighted images based on the signal contrast between normal and abnormal tissue. Due to the short repetition times of the DW-PSIF sequence in the order of 20-30 ms, it is rather insensitive to the influence of bulk motion and also allows for the acquisition of diffusion-weighted 3D-images [61]. In [62, 63] ADCs in phantoms were determined using the signal model derived in section 4.4.

3.3.2 DWI of the Brain

The primary applications of diffusion imaging in the clinical routine is the early assessment of injury in stroke [64]. A stroke of ischemic origin starts with a sudden interruption of blood flow to a region of the brain, starting a cascade of destructive events that ultimately lead to ischemic injury and infarction. The therapeutic window for delivering drugs to break up the embolus and restore flow before irreversible damage has occurred, is the first hours after onset. In the very early acute stages

of stroke, conventional MRI, such as T_1 -weighted, T_2 -weighted, or density-weighted images, and computed tomography appear normal. These conventional techniques show the area of the stroke only several hours after the event. However, DWI shows a fall in the ADC within minutes of the interruption of blood flow [65]. In human studies, the size of the lesion measured acutely with DWI correlated strongly with the neurological deficit assessed 24h after the stroke onset [66]. Other disorders such as status epilepticus [67] and spreading depression [68] also exhibit early changes in the ADC. For this reason, DWI is widely used clinically for the early assessment of stroke and other disorders and is also a standard technique for animal studies investigating the patho-physiological changes involved in stroke.

The reason for the abrupt decrease of the ADC in stroke is not fully understood. Early ideas were based on the hypothesis noted above, that the diffusion coefficient, D , for intracellular water is substantially lower than the diffusion coefficient for extracellular water, and that the measured ADC is a weighted average of these two different values. The change in the ADC with stroke then could be a result of cytotoxic edema, with a water shift from extracellular to the intracellular space, which would move the average ADC toward the intracellular value [69, 10]. Other investigators have argued on the basis of an observed bi-exponential behavior, that a simple averaging of D values is not adequate to understand the ADC changes fully [70]. An alternative theory is that the intracellular swelling increases the tortuosity of the diffusion paths in the extracellular space, decreasing the extracellular ADC [71]. However, other data indicate that D is reduced in both the intracellular and the extracellular compartment [72, 73]. An alternative idea is that a part of the ADC of the intracellular water results from active cytoplasmic motions driven by ATP-dependent mechanisms, and that early in stroke these driven motions stop, leading to a reduced intracellular ADC [74]. All of these mechanisms may play a role in reducing the measured brain ADC, but a quantitative understanding of the phenomenon is still lacking. Exemplary images obtained with a diffusion-weighted echo planar imaging sequence in a patient with a posterior infarct are shown in Fig. 3.4. On the diffusion-weighted images, the infarct appears brighter than the healthy tissue, while the ADC is significantly reduced.

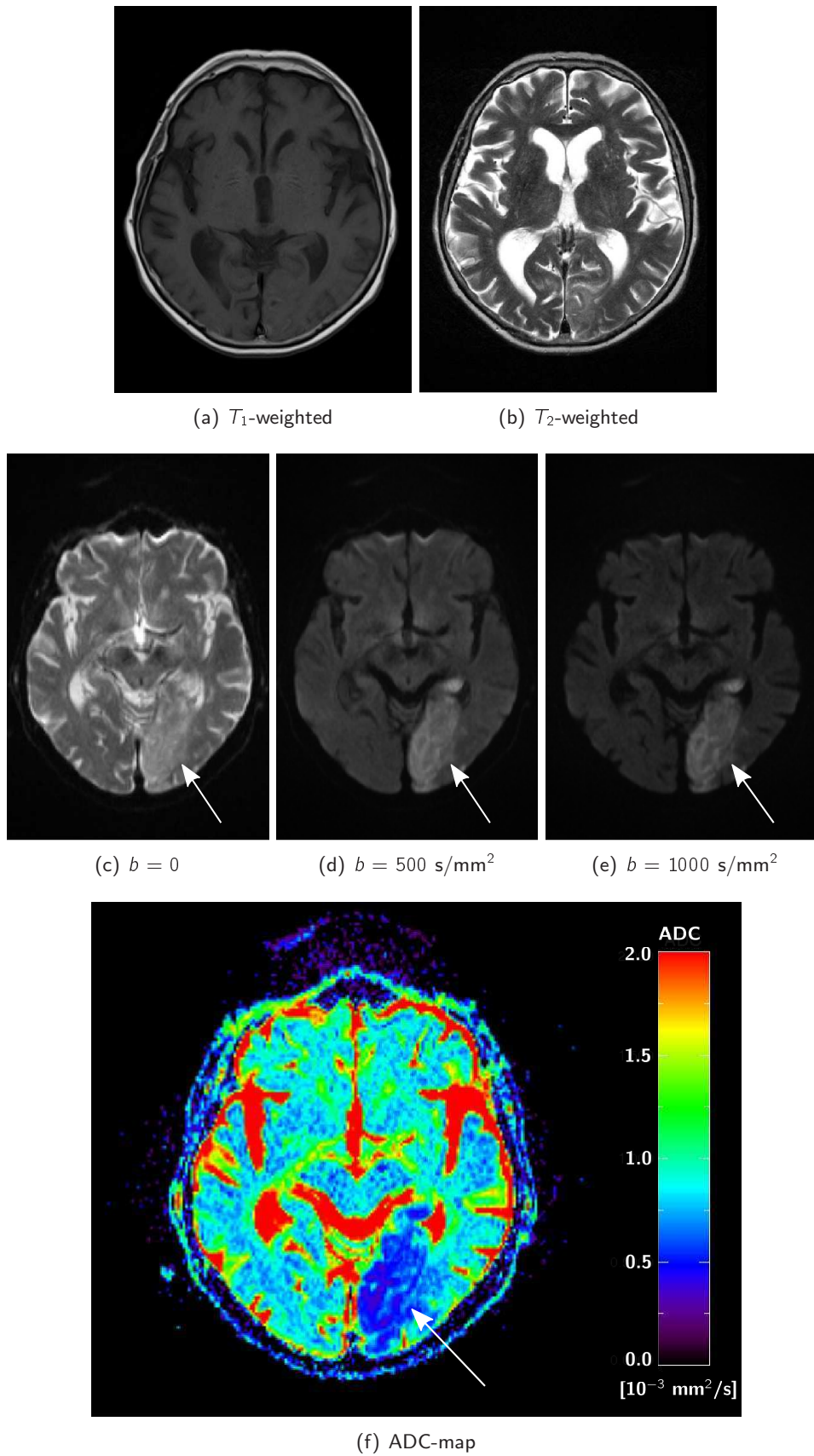
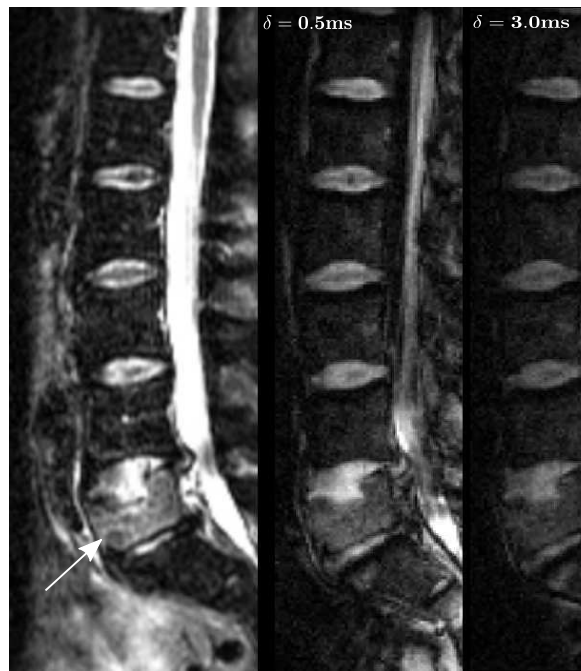


Figure 3.4: Axial diffusion-weighted images obtained with a DW-EPI sequence (c-e) and the corresponding ADC map of the brain of a patient with a posterior infarct on the left side (indicated by the arrows). For reference the T_1 -weighted and T_2 -weighted image of the same slice are shown.

3.3.3 DWI of the Body

For many years, the use of DWI was restricted to the central nervous system, because motion artifacts, primarily derived from bulk motion, and the challenging magnetic environment outside the brain made it difficult to produce diffusion-encoded images with sufficient image quality within a reasonable acquisition time. This situation, however, has significantly improved within the last decade and the technical limitations of this demanding imaging technique could be surpassed. Rapid developments in MR hardware and sequence technology, as described above, increased the robustness of DWI and this diagnostic tool has now the potential to produce diffusion-weighted images of diagnostic quality of tissues outside the brain within a reasonable time span. Examples of studies that applied DWI successfully outside the brain include the prostate [75], the breast [76], the liver [77] and the kidneys [78]. In the following, we want to concentrate on the applications of DWI in the musculoskeletal system (MSK) [79].

Non-quantitative DWI: Most applications of DWI to the MSK focused on the spine. During recent years non-quantitative DWI was also applied outside the spine, using a technique called diffusion-weighted whole-body imaging with background suppression (DWIBS), which was introduced by Takahara et al. [80]. The aim of DWIBS is to provide images that are comparable with PET. The primary focus is the sensitive depiction of lesions and it was demonstrated that it is sensitive to bone-marrow lesions as well [81, 82, 83]. It was also shown that whole-body DWI is superior to skeletal scintigraphy in the detection of bone metastases [84]. The first applications of DWI in the spine were based on the non-quantitative evaluation of the DW-PSIF sequence in vertebral bodies. Baur et al. [12] differentiated between benign osteoporotic and malignant vCFs based on the relative signal intensity of the affected vertebra. The problems of differentiation between these pathologies based on conventional MRI were discussed in section 2.5. It was demonstrated that benign osteoporotic fractures appear hypointense or isointense on DW-PSIF images, while malignant fractures, caused by bone-marrow tumors and metastases, appear hyperintense. Several similar studies of non-quantitative DWI of vCFs were performed during recent years, most of these being compatible with a general tendency to hypointensity in benign vertebral fractures and to hyperintensity in malignant fractures [19, 18, 14, 85]. Exemplary images acquired with a DW-PSIF sequence in patients with benign osteoporotic and malignant fractures are shown in Fig. 3.5. Non-quantitative diffusion-weighted images were also acquired with other sequences such as single-shot EPI [86], single-shot FSE [39] or conventional SE or STE [13]. But in general, the signal behavior showed up more clearly on images obtained with the DW-PSIF sequence.



(a) Malignant fracture L5



(b) Osteoporotic fracture L1

Figure 3.5: Exemplary images of two vertebral fractures (indicated with arrows) acquired with a DW-PSIF sequence with two different durations δ of the diffusion weighting gradient. For reference, the corresponding STIR image is shown on the left. Sequence parameters were set to $T_R = 25$ ms, $G = 23$ mT/m and $\alpha = 40^\circ$.

An important factor in diffusion-weighted SSFP imaging is the influence of in- and opposed-phase effects between the fat and water components, which will be explained in section 4.1. These effects are particularly relevant for vBM, since it contains fat and water fractions at the same order of magnitude, whereas most other tissues consist of a single predominant component, see section 2.2. Thus, a small change of the sequence timing, more precisely of T_E , leads to a significant change of the signal intensity of vBM relative to its surroundings; see Fig. 3.6, where this effect is shown for two images of the spine acquired in the in- and opposed-phase state. The original studies by Baur et al.[12, 87, 18] were based on a DW-PSIF sequence with approximately opposed-phase readout. Measurements were performed at 1.5 T and the time interval between the echo readout and the center of the following excitation pulse was set to 7.2 ms. The acquisition of images with a different setting of this parameter might result in completely different signal properties, potentially reducing the differentiability between vCFs and normal-appearing vBM. The exact signal behavior of the DW-PSIF is as yet not fully understood and will be the topic of this thesis in section 5.

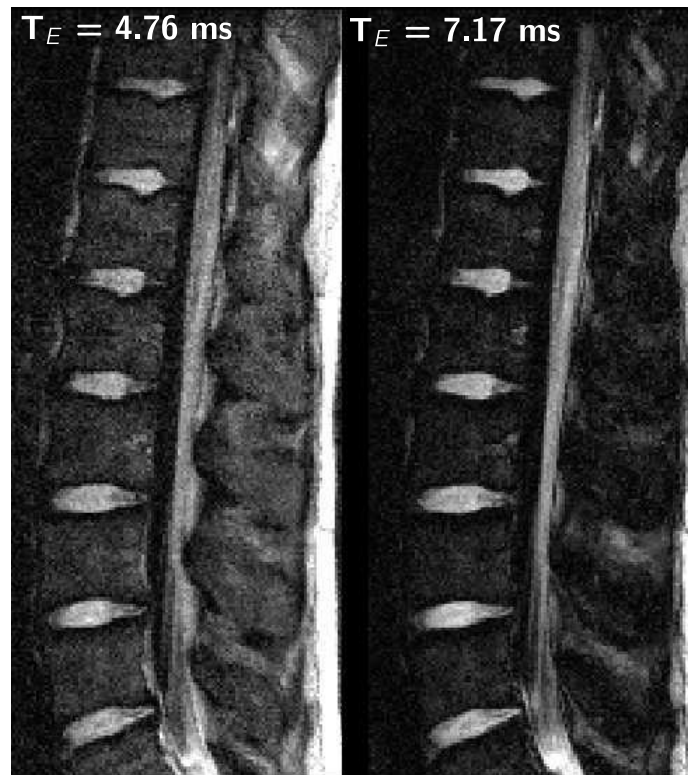


Figure 3.6: DW-PSIF images of the spine acquired for different values of the T_E corresponding to the in- and opposed-phase.

Quantitative DWI: Non-quantitative DWI has the disadvantage that the image contrast and differentiation depends on the exact measurement setup, i.e. sequence choice, strength of diffusion weighting, etc. Thus, the interpatient comparability as well as the comparability of different studies is limited. In contrast, quantitative DWI provides a measurement of a physical parameter that, theoretically, should be independent of the acquisition technique, allowing ideally for the determination of universally valid cutoffs to differentiate between normal and abnormal tissues or different pathologies. For quantification, two or more images with different diffusion weightings are acquired, where the diffusion-weighting is given in terms of the b -value [s/mm^2], depending on the duration and amplitude of the diffusion gradient as well as on the time period between the application of the diffusion gradients. The apparent diffusion coefficient can be calculated from the signal curve of the diffusion-weighted images using Eq. (3.32). Several studies applied quantitative DWI to normal and pathological bone marrow. Typical values of the ADC in normal bone marrow are in the range of 0.2 to $0.5 \times 10^{-3} \text{ mm}^2/\text{s}$ [88]. Partially, these variations are explained by the different pulse sequences and diffusion weightings used in these studies. In addition, the diffusion properties of bone marrow are also strongly dependent on the distribution pattern of yellow and red marrow, and in particular on the fractions of fat and water. The ADC of water was found to be about $3 \times 10^{-3} \text{ mm}^2/\text{s}$ at body temperature [89]. Only very few results exist with regard to the in vivo determination of the ADC of protons in fat. Lehnert et al. [90] reported ADC values of $0.012 - 0.021 \times 10^{-3} \text{ mm}^2/\text{s}$ in subcutaneous fat and similar values of $0.011 - 0.012 \times 10^{-3} \text{ mm}^2/\text{s}$ in yellow bone marrow. In the bone marrow of rat paws, Abadneh et al. [91] reported an ADC of $0.018 \times 10^{-3} \text{ mm}^2/\text{s}$. Ward et al [92] reported ADC values of $0.2 \times 10^{-3} \text{ mm}^2/\text{s}$ in red and $0.1 \times 10^{-3} \text{ mm}^2/\text{s}$ in yellow marrow. These results suggest that the ADC in fat is very close to zero and, hence, the most important difference with respect to the applied pulse sequences is the use of fat saturation, which is required for single-shot echo-planar imaging but is optional in combination with spin-echo or fast-spin-echo techniques. Due to the very low ADC of fat, the calculated diffusion coefficients of normal bone marrow are systematically decreased when fat saturation is not applied. Typical values of the ADC determined without fat saturation [93, 16, 14, 94, 95, 96, 97] are in the range of 0.2 to $0.3 \times 10^{-3} \text{ mm}^2/\text{s}$ in contrast to 0.3 to $0.5 \times 10^{-3} \text{ mm}^2/\text{s}$ with fat saturation [15, 17, 98, 99, 100, 101, 102].

Several studies applied quantitative DWI to normal and pathological vertebral bone marrow [15, 16, 17, 98, 103, 95, 96, 104]. Pathological bone marrow exhibits much higher ADCs, ranging from about 0.7 to $1.0 \times 10^{-3} \text{ mm}^2/\text{s}$ in metastases as well as malignant fractures, and from about 1.0 to $2.0 \times 10^{-3} \text{ mm}^2/\text{s}$ in osteoporotic

or traumatic fractures [88]. Typical image examples are shown in Fig. 3.7. Although the measured ADC may be indicative for benign or malignant lesions, a considerable overlap has been described in several studies. In addition, ADC values of different studies are not always comparable due to varying measurement setups, i.e. inclusion of fat saturation, choice of b -values etc. In contrast to normal marrow the differences induced by the use of fat saturation are smaller in lesions, since the relative fat content is much lower there than in normal vBM. Theoretically the choice of the b -values should not effect the calculation of the ADC-value, if the choice of the b -value range covers most of the decay dynamics. However, this is not true in practice. At very low b -values, the diffusion effect is known to be overestimated due to the contribution of perfusion to the signal attenuation [105, 99]. On the other hand, at high b -values, greater than 600 s/mm^2 , the ADC can be underestimated since the signal intensities become dominated by noise. In the future, a consensus on the optimum choice of the measurement parameters should be found.

The pathophysiological background of the described diffusion properties in vBM is not yet fully understood. Currently, the most probable hypothesis is that the molecular diffusion of water is substantially increased in osteoporotic fractures because of bone-marrow edema and the disruption of the trabecular structure. In malignant vCFs, the diffusion is partially restricted due to the high cellularity of tumor tissue [12].

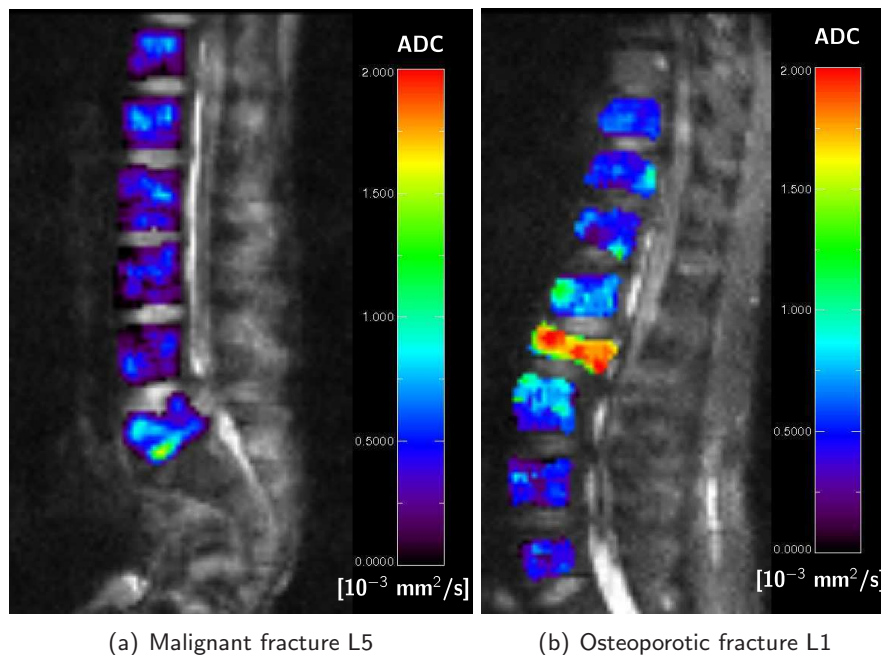


Figure 3.7: ADC-maps obtained with a fat-saturated DW-ssTSE sequence with b -values of 100, 250, 400 and 600 s/mm^2 .

Quantitative DWI has also been applied for the evaluation of degenerative disc disease [106]. It may provide information about early changes of the pathophysiology of the intervertebral disc and might be helpful to predict if or when disc bulging occurs and if a non-surgical treatment could be successful. In contrast to the vertebral bodies, the water content of the intravertebral discs is rather high, thus the SNR on diffusion-weighted images is high and allows reliable diffusion measurements [107]. It was shown that the ADC of the annulus fibrosus is substantially lower than the ADC of the nucleus pulposus and that the ADC shows a cranio-caudal gradient with the ADC decreasing from the cervical spine downwards. In degenerated discs, the ADCs were reported to be significantly decreased compared to the discs of healthy volunteers. It was also shown, that mechanical load leads to a reduction of diffusion in the disc and since diffusion is responsible for the nutrient supply, this might accelerate disc degeneration [108].

Another important application of quantitative DWI is the differentiation of soft tissue tumors. Since DWI reveals the microstructure of such masses it may be helpful to distinguish benign masses from malignancy. In general, published results showed that ADCs of soft-tissue malignancies are ranging from 0.6 to $1.4 \times 10^{-3} \text{ mm}^2/\text{s}$, whereas ADCs in non-neoplastic soft-tissues such as muscle tissue are ranging from 1.5 to $1.8 \times 10^{-3} \text{ mm}^2/\text{s}$ [109, 110]. As in the case of cCF some overlap exists between benign soft-tissue tumors and soft-tissue malignancies such as lipomas, where restricted diffusion is present due to the high amount of fatty tissue.

Further applications of quantitative DWI include therapy monitoring and treatment planning, which are not discussed here.

Chapter 4

MR Signal Theory

In this chapter the basic features and applications of the *Steady-State Free Precession* (SSFP) sequence are reviewed. SSFP is a special form of gradient echo imaging based on the repetitive application of a radiofrequency (RF) pulse with a fixed flip angle separated by a fixed time interval defined as the repetition time T_R . First, a brief introduction to the formation of the gradient echo signal (GRE) after the application of a single RF pulse and its characteristics is given. Afterwards the signal of the SSFP will be derived theoretically and the signal equations for the different sequences based on the SSFP will be presented, and some exemplary applications will be shown. Finally, the signal of the diffusion-weighted SSFP sequence will be derived and its general dependence on the relaxation times and the ADC will be discussed.

4.1 Gradient-Echo Signal

In general, the simplest form of a gradient echo pulse sequence consists of a RF pulse with an arbitrary flip angle followed by a signal measurement at the so-called echo time T_E after the RF pulse. In MRI this pattern is applied repeatedly at T_R varying the gradient in the phase-encoding direction. In contrast to a spin-echo (SE) sequence, where an echo is produced by the application of a pair of a 90° and an 180° RF pulse, a gradient echo is formed typically by the application of a pair of bipolar gradient pulses. It is therefore described as a gradient recalled-echo (GRE) or gradient echo. Usually a negative gradient lobe is applied prior to the frequency encoding gradient so that a gradient echo forms at the center of data collection. At the occurrence of the gradient echo the dephasing of the spins caused by the negative gradient pulse is compensated by the positive gradient pulse and the net effect of the gradients applied up to that time is zero. The prototype of such a pulse sequence is

the FLASH (fast low-angle shot) sequence [111].

The term gradient echo imaging might be a bit misleading because it suggests that these method uses gradient echos instead of RF echoes. But as will be shown in the following not only a spin echo formed by a $90^\circ - 180^\circ$ pulse pair, but also a series of RF pulses with an arbitrary flip angle can produce a generalized echo [50]. In addition, gradient echoes are used for image acquisition in SE as well as GRE imaging. The only difference between a SE and GRE is the inclusion of the 180° refocusing pulse in the SE sequence.

The absence of the refocusing pulse causes two important differences between the GRE and SE signal. Firstly, the dephasing effects of field inhomogeneities are not reversed and, accordingly, the GRE signal decays exponentially with increasing T_E with the decay constant T_2^* in contrast to the SE signal decaying with T_2 . Usually, T_2^* is considerably smaller than T_2 and hence the T_E of a GRE sequence should be kept small, up to 30 ms in T_2^* weighted MRI. The second effect is caused by the difference of the resonant frequencies of the hydrogen nuclei in fat and water, referred to as the chemical shift [112]. Due to the absence of the refocusing pulse, fat and water signals develop different phases and the net signal of a voxel containing fat and water shows oscillations of the signal intensity with increasing T_E . The extreme cases with parallel and antiparallel alignment of the water and fat magnetization are referred to as in-phase and out-of-phase condition. As we will show in section 5.7 this effect can be used to estimate the fat/water content of tissues or to partly suppress the signal from tissues containing fat.

The absence of the refocusing pulse allows for the use of significantly shorter T_R 's in GRE pulse sequences. Firstly, the absence of the 180° pulse shortens T_R and secondly the RF exposure per T_R is considerably smaller for a GRE sequence. Since the deposited energy in the body is proportional to the square of the flip angle one repetition of a SE pulse sequence deposits 45 times as much energy as one repetition of the GRE sequence with a single 30° RF pulse.

First, we want to derive the signal for a flip angle of 90° . In this case the longitudinal magnetization after application of the RF pulse is zero. For a long T_R , much greater than T_2 , the whole transverse magnetization generated by the previous RF pulse has decayed away and the contrast characteristics of the GRE are similar to the SE case. For a T_R much longer than T_1 , the whole longitudinal magnetization recovers and the image will therefore be proton-density-weighted for a short T_E . Decreasing the TR results in an increasing T_1 weighting of the image similar to the SE sequence. Therefore except for the decay of the signal with T_2^* in contrast to T_2 the contrast characteristics of the GRE and SE sequence are equivalent. For a short T_E ,

the signal is given by

$$S(T_E) = M_0 e^{-T_E/T_2^*}, \quad (4.1)$$

where M_0 is the longitudinal equilibrium magnetization. In general, in addition to T_R it is also possible to vary the flip angle α in a GRE sequence. Assuming the special case of a spoiled GRE pulse sequence – the signal will be derived in section 4.2 – the evolution of the contrast with varying α is shown in Fig. 4.1. First of all it can be seen that for a long T_R of 3000 ms the T_1 -weighting is rather small compared to the a the shorter T_R of 500ms. Furthermore, the contrast between the two components with T_1 -values of 1000 and 500 ms is almost independent of α . As expected at flip angles close to 90° the signal is strongly T_1 -weighted for a short T_R . However a reduction of the α yields a decrease of the T_1 -weighting. In the case of a small α , the longitudinal magnetization needs less time to recover and accordingly the T_1 -weighting decreases. Therefore, a GRE sequence offers the possibility to decrease the T_1 -weighting by either increasing T_R or decreasing α for a short T_R in the order of a few milliseconds.

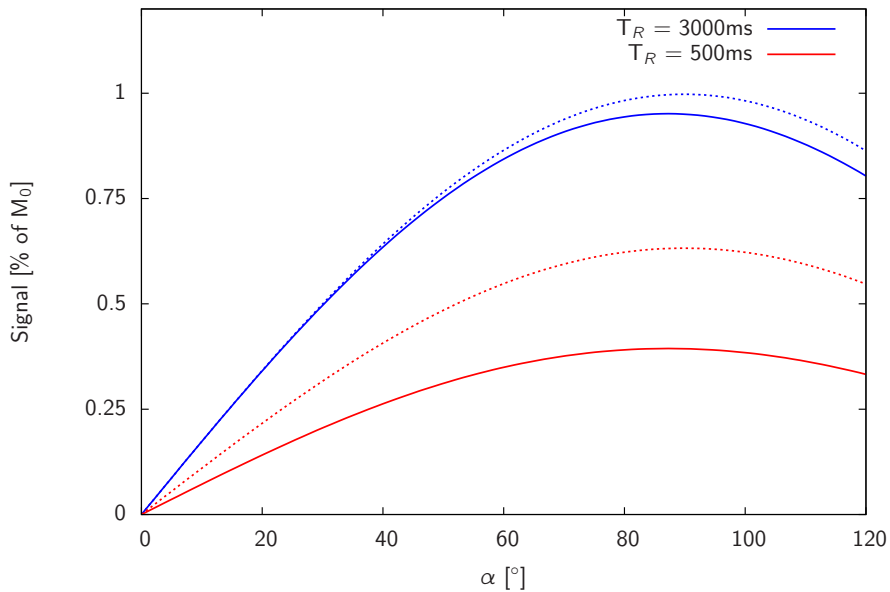


Figure 4.1: Signal behavior of a spoiled GRE sequence as a function of the flip angle. Shown are the signals for to different values of T_R . The blue lines correspond to $T_R = 3000$ ms and the red lines to 500 ms. The solid line corresponds to a T_1 of 1000 ms and the dashed line to 500 ms, respectively.

4.2 Spoiled Gradient Echo

Depending on the vendor of the manufacturer of the MR imager, different names exist, the most common being SPGR or FLASH [111] and T_1 fast field echo (T1-FFE). If T_R between the repetitive application of the RF pulses is decreased further to values comparable or less than T_2 the transverse magnetization will not decay away before the next RF pulse and the longitudinal magnetization will not be completely restored. In the special case of a spoiled GRE sequence, the idea is to achieve a complete dephasing of the transverse magnetization before the application of the following RF pulse in each T_R -cycle. This signal is referred to as the spoiled signal, which consists only of the free induction decay (FID) without any echoes. The spoiling of the transverse magnetization can be accomplished in a variety of ways. As in the case of the SE sequence, a long T_R could be chosen, so that the transverse magnetization decays away before the next RF-pulse. But in order to enable short image acquisition times, a different spoiling strategy exists. Firstly, a gradient spoiler at the end of each cycle can be used, but are only effective if the gradient area varies from T_R to T_R interval. In this case the spoiling is spatially nonuniform, since the gradients produce spatially varying fields. A second solution is the use of RF spoiling [113, 114], where the phase of the RF excitation pulse is changed according to a predetermined phase-cycling scheme. In general RF- and gradient-spoiling are combined to achieve almost perfect spoiling.

Assuming perfect RF-spoiling, each RF pulse causes a transverse magnetization, producing an FID that can be rephased into a GRE. Since the longitudinal magnetization does not completely relax to its equilibrium state during a T_R -interval, the transverse magnetization produced by the subsequent RF pulse is decreased compared to the previous interval. After a few acquisitions, $n \approx T_1/T_R$, the longitudinal and with it the transversal magnetization reaches a steady state. In this state the effect of the RF pulse is exactly compensated by the longitudinal relaxation. The spoiled signal produced by the rephasing of the FID is given by

$$S_{\text{spoil}} = M_0 \frac{\sin(\alpha) (1 - e^{-T_R/T_1})}{(1 - \cos(\alpha) e^{-T_R/T_1})} e^{-T_E/T_2^*}. \quad (4.2)$$

The flip angle that maximizes the signal of the spoiled GRE is called the *Ernst angle*. It can be derived by setting the first derivative of Eq.(4.2) to zero:

$$\alpha_E = \arccos \left(e^{-T_R/T_1} \right) = \arccos(E_1). \quad (4.3)$$

4.3 Steady-state Free Precession

In the case of a SSFP sequence no spoiling is applied. Therefore, the RF pulses do not solely act on the longitudinal but also on the transverse magnetization. Much of the magnetization in the imaging slice experiences a series of identical excitation pulses with flip angle α , evenly distributed in time by T_R , see Fig. 4.2. The signal after the next RF pulse will not solely consist of the FID as in the case of the SPGR. The remaining transverse magnetization will have acquired different phases through local field offsets and may hence be incoherent. But, since these offsets are the same during each T_R period, the RF pulse will produce echoes that will add up and together produce a strong coherent signal before and after the RF pulse. After a few repetitions the signal will approach a steady state. This condition producing a constant signal just before or after the RF pulse is called *steady-state free precession*. In the following, the characteristics of two types of sequences, acquiring either the signal before or after the RF pulse, will be briefly discussed.

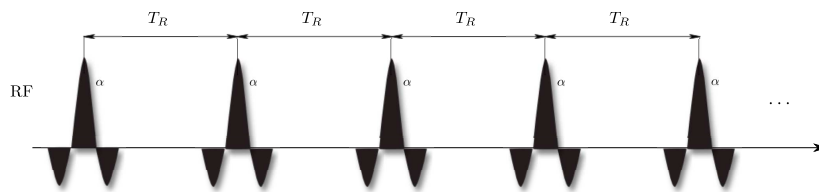


Figure 4.2: A train of RF excitation pulses used in the analysis of the GRE.

4.3.1 SSFP-FID and SSFP-Echo

The sequence diagram of an unspoiled SSFP-sequence is shown in Fig. 4.3. The SSFP-FID, acquired by sequences known under acronyms such as FISP, FFE or GRASS, corresponds to the FID-like signal forming just after each RF pulse. In general, the SSFP-FID sequence provides greater signal than the spoiled GRE, but at the cost of reduced contrast. The SSFP-Echo, acquired by sequences known as PSIF, CE-FAST or T2-FFE, corresponds to the time-reversed echo-like signal that forms just before each RF pulse. In contrast to the spoiled GRE, the RF pulses are phase coherent to avoid spoiling of the transverse magnetization and it is assumed that the phase accumulated by the transverse magnetization is the same in each T_R -interval. If these conditions are met, steady states for the longitudinal and transverse magnetization form [115, 116]. In the following, we will derive the signals of the SSFP-FID and SSFP-Echo, shown as S^\pm in Fig. 4.4 [117].

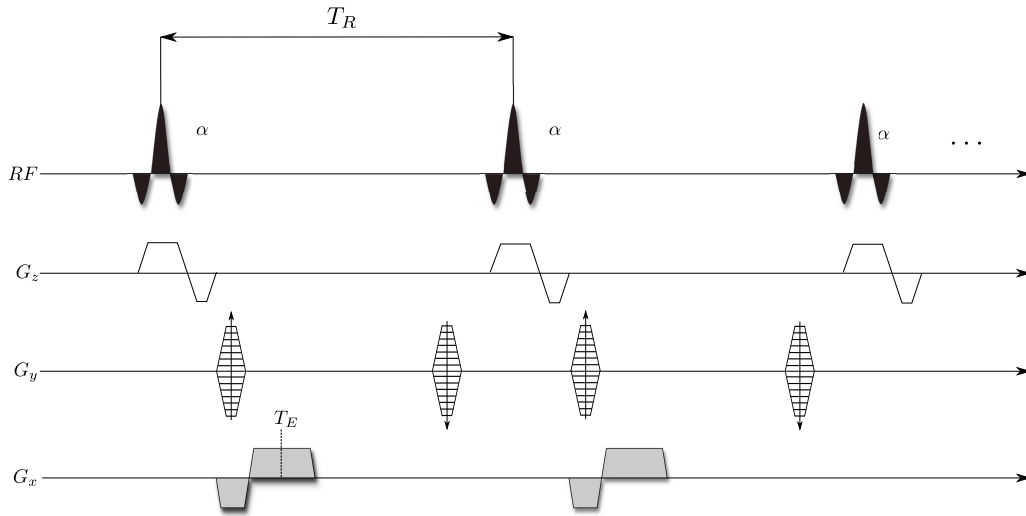


Figure 4.3: Sequence diagram of an SSFP-sequence recording the SSFP-FID.

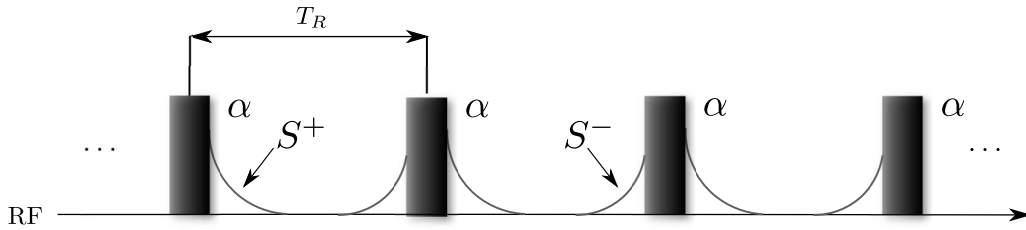


Figure 4.4: Representation of the transverse steady state for SSFP sequence.

For the signal analysis of the SSFP-FID and -Echo we write the magnetization as a vector

$$\vec{M}(t) = \begin{pmatrix} M_x(t) \\ M_y(t) \\ M_z(t) \end{pmatrix}, \quad (4.4)$$

The evolution of the magnetization is described by the Bloch equations given by

$$\vec{M}(t) = D(t)\vec{M}(0) + M_0 (1 - E_1(t)) \hat{z}, \quad (4.5)$$

where \hat{z} is the unit vector in z-direction and $E_1(t) = e^{-t/T_1}$. Furthermore we intro-

duce

$$D(t) \equiv \begin{pmatrix} e^{-t/T_2} & 0 & 0 \\ 0 & e^{-t/T_2} & 0 \\ 0 & 0 & e^{-t/T_1} \end{pmatrix} \quad (4.6)$$

describing the T_2 -relaxation of the magnetization. The following analysis is valid for an isochromat of spins, where macroscopic spin phase effects can be ignored. After having derived the equilibrium equations, we will consider a voxel instead of the isochromat, leading to the replacement of T_2 by T_2^* . In the interval between two RF-pulses the transverse magnetization precesses freely and it will obtain an additional phase due to static field inhomogeneities and the applied gradient fields. A necessary condition to establish a steady-state is that the gradient area in each T_R -interval is constant. Thus, the phase encoding gradient has to be rewinded. The precession angle is defined as

$$\beta(t) = \gamma \Delta B \cdot t + \gamma \vec{r} \int_0^t \vec{G}(t) dt \quad (4.7)$$

where the two terms are the static and gradient field inhomogeneity-induced resonance offset angles, respectively. Considering the free precession in Eq. (4.5), defining $t' = t - nT_R$ and n as the time nT_R , the evolution of the magnetization in a T_R -interval for $nT_R \leq t \leq (n+1)T_R$ is given by

$$\vec{M}(n, t') = D(t')P(t')\vec{M}(n, 0) + M_0 (1 - E_1(t')) \hat{z}. \quad (4.8)$$

$P(t')$ represents the free precession of the transverse magnetization and is defined as

$$P(t') \equiv \begin{pmatrix} \cos(\beta(t')) & \sin(\beta(t')) & 0 \\ -\sin(\beta(t')) & \cos(\beta(t')) & 0 \\ 0 & 0 & 1 \end{pmatrix}. \quad (4.9)$$

Combining Eq. (4.6) and (4.9) the evolution during each T_R -interval is given by

$$F_P(t') = D(t') \cdot P(t') \quad (4.10)$$

$$= \begin{pmatrix} \cos(\beta(t')) E_2(t') & \sin(\beta(t')) E_2(t') & 0 \\ -\sin(\beta(t')) E_2(t') & \cos(\beta(t')) E_2(t') & 0 \\ 0 & 0 & E_1(t') \end{pmatrix}, \quad (4.11)$$

where we defined $E_2(t') = \exp(-t'/T_2)$. We assume that the RF pulse is applied along the x-axis of the rotating frame of reference. It corresponds to a clockwise rotation with flip angle α about \hat{x} and is defined as

$$R_x(\alpha) \equiv \begin{pmatrix} 1 & 0 & 0 \\ 0 & \cos(\alpha) & \sin(\alpha) \\ 0 & -\sin(\alpha) & \cos(\alpha) \end{pmatrix}. \quad (4.12)$$

Hence, the magnetization \vec{M}^+ after the application of the RF pulse is given by

$$\vec{M}^+(n+1) = R_x(\alpha)\vec{M}^-(n), \quad (4.13)$$

and \vec{M}^- just before the application follows as

$$\vec{M}^-(n) = F_P(T_R)\vec{M}^+(n-1) + M_0(1 - E_1(T_R))\hat{z}. \quad (4.14)$$

In order to find the steady-state value of the magnetization M^\pm we set $\vec{M}^-(n) = \vec{M}^-(n-1)$ and $n \rightarrow \infty$ yields

$$\begin{aligned} \vec{M}^-(\infty) &= F_P(T_R)\vec{M}^+(\infty) + M_0(1 - E_1(T_R))\hat{z} \\ \vec{M}^-(\infty) &= F_P(T_R)R_x(\alpha)\vec{M}^-(\infty) + M_0(1 - E_1(T_R))\hat{z} \\ \vec{M}^-(\infty) &= [I - F_P(T_R)R_x(\alpha)]^{-1} M_0(1 - E_1(T_R))\hat{z}, \end{aligned} \quad (4.15)$$

where I corresponds to the identity matrix. Accordingly setting $\vec{M}^+(n) = \vec{M}^+(n-1)$ for $n \rightarrow \infty$ we get

$$\begin{aligned} \vec{M}^+(\infty) &= R_x(\alpha)\vec{M}^-(\infty) \\ \vec{M}^+(\infty) &= R_x(\alpha)F_P(T_R)\vec{M}^+(\infty) + R_x(\alpha)M_0(1 - E_1(T_R))\hat{z} \\ R_x(\alpha)^{-1}\vec{M}^+(\infty) &= F_P(T_R)\vec{M}^+(\infty) + M_0(1 - E_1(T_R))\hat{z} \\ \vec{M}^+(\infty) &= [R_x^{-1}(\alpha) - F_P(T_R)]^{-1} M_0(1 - E_1(T_R))\hat{z}. \end{aligned} \quad (4.16)$$

Rotation matrices satisfy the following equation, $R^{-1} = R^T$, and therefore

$$R_x^{-1}(\alpha) = \begin{pmatrix} 1 & 0 & 0 \\ 0 & \cos(\alpha) & -\sin(\alpha) \\ 0 & \sin(\alpha) & \cos(\alpha) \end{pmatrix}. \quad (4.17)$$

Now we can evaluate

$$\left[R_x^{-1}(\alpha) - FP(T_R) \right]^{-1} \hat{z} = \begin{pmatrix} 1 - E_2(T_R) \cos(\beta) & -E_2(T_R) \sin(\beta) & 0 \\ E_2(T_R) \sin(\beta) & \cos(\alpha) - E_2(T_R) \cos(\beta) & -\sin(\alpha) \\ 0 & \sin(\alpha) & \cos(\alpha) - E_1(T_R) \end{pmatrix}^{-1} \hat{z}. \quad (4.18)$$

The evaluation of Eq. (4.18)¹ in Eq. (4.16) and (4.15) yields

$$\vec{M}^+(\infty) = \frac{M_0 (1 - E_1(T_R))}{D} \begin{pmatrix} E_2(T_R) \sin(\alpha) \sin(\beta) \\ \sin(\alpha) (1 - E_2(T_R) \cos(\beta)) \\ E_2(T_R) (E_2(T_R) - \cos(\beta)) + (1 - E_2(T_R) \cos(\beta)) \cos(\alpha) \end{pmatrix}, \quad (4.19)$$

and

$$\vec{M}^-(\infty) = \frac{M_0 (1 - E_1(T_R))}{D} \begin{pmatrix} M_x^+(\infty) \\ E_2(T_R) \sin(\alpha) (\cos(\beta) - E_2(T_R)) \\ \cos(\alpha) (1 - E_2(T_R) \cos(\beta)) + E_2(T_R) (E_2(T_R) - \cos(\beta)) \end{pmatrix}, \quad (4.20)$$

where

$$D = (1 - E_1(T_R) \cos(\alpha)) (1 - E_2(T_R) \cos(\beta)) - E_2(T_R) (E_1(T_R) - \cos(\alpha)) (E_2(T_R) - \cos(\beta)). \quad (4.21)$$

The signal is a function of α , T_1 , T_2 and β . The dependence of the signal on α and β is shown in Fig. 4.5. It can be seen that in the case of a small flip angle a large signal response is only achieved for β close to 0° or 360° . For larger flip angles a high signal is achieved for a wide range of β values centered around $\beta = 180^\circ$. Since the static field varies as a function of position, β is function of position in the image. Usually, it is assumed that the field variations over a single voxel can be neglected.

1

$$A^{-1} = \begin{pmatrix} a & b & c \\ d & e & f \\ g & h & i \end{pmatrix}^{-1} = \frac{1}{\det(A)} \begin{pmatrix} ei - fh & ch - bi & bf - ce \\ fg - di & ai - cg & cd - af \\ dh - eg & bg - ah & ae - bd \end{pmatrix}$$

Due to the variation of $\beta(\vec{r})$ across the object the uniformity of the reconstructed image will be degraded.

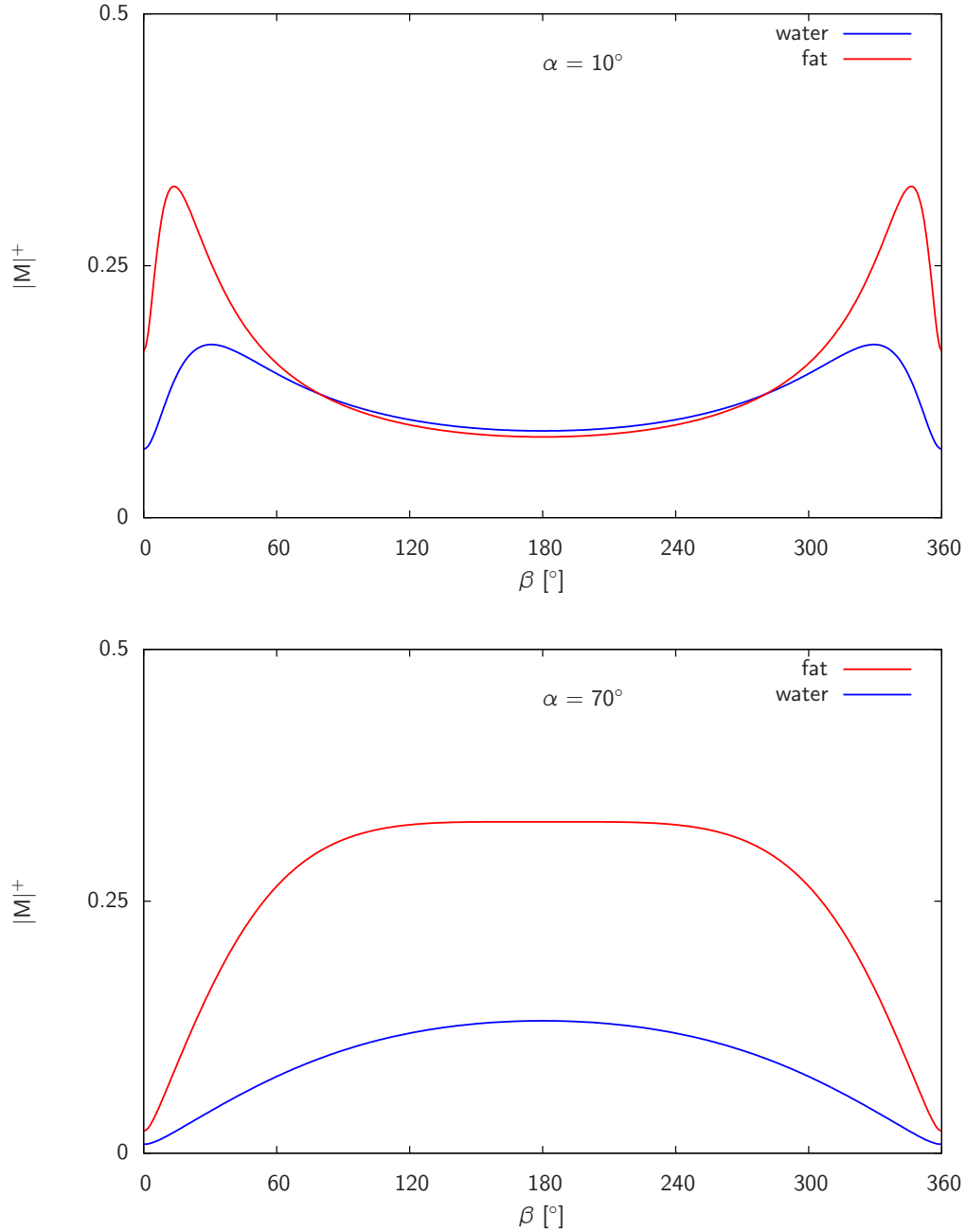


Figure 4.5: Plot of the magnitude signal $|M|^+$ as a function of the precession angle β for values of α of 10° and 70° . T_R was set to 10 ms and T_E was assumed to be 0.

The above equations are valid for isochromats with an effective resonance offset β . In typical imaging sequences the gradients are turned off and on and hence the resonance frequency is itself a function of time. To account for these effects a convolution analysis will be performed [118]. The phase angle acquired by an isochromat of spins is given by

$$\Delta\omega t = \int_0^t \omega(t') dt'. \quad (4.22)$$

The total off-resonance dephasing between two pulses is then defined as

$$\phi \equiv \Delta\omega T_R = \int_0^{T_R} \omega(t') dt'. \quad (4.23)$$

The transverse magnetization can also be expressed in complex notation

$$M_{\perp} = M_y + iM_x \quad (4.24)$$

Using this notation the transverse magnetization in Eq. (4.19) can be written as

$$M_{\perp}^+ = \frac{M_0(1 - E_1(T_R))}{D} \sin(\alpha) [1 - E_2(T_R)e^{-i\phi}] \quad (4.25)$$

In the subsequent repetition interval the evolution of $M_{xy}(t)$ is given by

$$M_{\perp}(t) = M_{\perp}^+ E_2(t) \exp(i\Delta\omega t) \quad (4.26)$$

$$= \frac{M_0(1 - E_1)}{D} \sin(\alpha) \left[E_2(t) \exp(i\Delta\omega t) - E_2(t + T_R) \exp(i\Delta\omega(t + T_R)) \right], \quad (4.27)$$

and the signal at the end of the interval is given by

$$M_{\perp}^- = \frac{M_0(1 - E_1(T_R))}{D} \sin(\alpha) E_2(T_R) (e^{i\phi} - E_2(T_R)). \quad (4.28)$$

It can be seen that the transverse magnetization is the sum of two components. The first is the FID component which is "in-phase" at $t = 0$ and is dephasing afterwards. The second is called the echo rephasing at $t - T_R = 0$, i.e. at the end of each interval [119]. The steady-state signal can now be calculated via the integration of Eq. (4.27)

over all inhomogeneities in the sample. We get

$$S(t) = \int_{-\infty}^{\infty} M_{\perp}(t, \Delta\omega) g(\Delta\omega) d(\Delta\omega), \quad (4.29)$$

where $g(\Delta\omega)$ is the spin distribution function. Plugging (4.27) into (4.29) yields

$$S(t) = \frac{M_0(1 - E_1(T_R))}{p} \sin(\alpha) \left[E_2(t) \int_{-\infty}^{\infty} \frac{g(\Delta\omega) e^{i\Delta\omega t}}{1 - (q/p) \cos(\Delta\omega T_R)} d(\Delta\omega) \right. \\ \left. - E_2(t + T_R) \int_{-\infty}^{\infty} \frac{g(\Delta\omega) e^{i\Delta\omega(t - T_R)}}{1 - (q/p) \cos(\Delta\omega T_R)} d(\Delta\omega) \right], \quad (4.30)$$

where we have used

$$p = 1 - E_1(T_R) \cos(\alpha) - E_2(T_R)^2 (E_1(T_R) - \cos(\alpha)) \quad (4.31)$$

$$q = E_2(T_R) (1 - E_1(T_R)) (1 + \cos(\alpha)). \quad (4.32)$$

Assuming that $|p| > |q|$ for all α and $T_2 < T_1$, the denominator in Eq. (4.30) can be written as geometrical series

$$\left(1 - \left(\frac{q}{p} \cos(\beta T_R) \right) \right)^{-1} = 1 + \sum_{n=1}^{\infty} \left(\frac{q}{p} \right)^n \cos^n(\beta T_R) \quad (4.33)$$

and as shown in [119] the integral can be solved and the amplitudes of the signals are given by

$$S_{\text{FID}} = \frac{M_0(1 - E_1(T_R))}{p} \sin(\alpha) (u - E_2(T_R) v) \quad (4.34)$$

$$S_{\text{Echo}} = \frac{M_0(1 - E_1(T_R))}{p} \sin(\alpha) (E_2(2T_R) u - E_2(T_R) v). \quad (4.35)$$

The terms u and v are given by

$$u = 1 + \sum_{m=1}^{\infty} \left(\frac{q}{2p} \right)^{2m} \binom{2m}{m} \quad (4.36)$$

$$v = \frac{1}{2} \sum_{m=1}^{\infty} \left(\frac{q}{2p} \right)^{2m-1} \binom{2m}{m}. \quad (4.37)$$

Both summations converge since $|p| > |q|$. The FID and echo signal are both a combination of coincident responses, primary, secondary and stimulated echoes. Closed

expressions of (4.34) and (4.35) where defined in [120]

$$S_{\text{FID}} = M_0 \tan\left(\frac{\alpha}{2}\right) (1 - (E_1(T_R) - \cos(\alpha)) \cdot r) \quad (4.38)$$

$$S_{\text{Echo}} = M_0 \tan\left(\frac{\alpha}{2}\right) (1 - (1 - E_1(T_R) \cos(\alpha)) \cdot r) \quad (4.39)$$

with:

$$r = \frac{1 - E_2(T_R)^2}{\sqrt{p^2 - q^2}} = \sqrt{\frac{1 - E_2^2}{(1 - E_1 \cos(\alpha))^2 - E_2^2 (E_1 - \cos(\alpha))^2}}. \quad (4.40)$$

It is assumed that the SSFP-FID and the SSFP-Echo do not overlap substantially in the readout window. The evolution of the signal of the S_{FID} and the S_{Echo} is shown in Fig. 4.6. The flip angle corresponding to the maximum signal depends on the relaxation times. In addition the signal amplitude increases with decreasing T_1 and with increasing T_2 . In general the signal evolution is more complicated than in the spoiled case, but there are some simple limiting cases. If $T_R \gg T_2$, then E_2 is negligible and $p \rightarrow (1 - E_1 \cos(\alpha))$ and $q \rightarrow 0$. Therefore the SSFP-Echo $\rightarrow 0$ and using $\tan(x/2) = \sin(x)/(1 + \cos(x))$

$$S_{\text{FID}} \rightarrow M_0 \sin(\alpha) \frac{(1 - E_1)}{1 - E_1 \cos(\alpha)}, \quad T_R \gg T_2 \quad (4.41)$$

corresponding to the spoiled case Eq. (4.2) up to factor of e^{-T_E/T_2^*} . If the SSFP-FID is rephased as a GRE at time T_E , the two expressions become identical.

In general the spoiled GRE, SSFP-FID and SSFP-Echo all provide substantially different contrast behavior. At intermediate and high flip angles, spoiled GRE provides considerable T_1 -weighting and dark fluid signal, whereas SSFP-FID provides less contrast but bright fluid signal. For fixed imaging parameters, the signal of the SSFP-FID is greater than the spoiled GRE signal. The SSFP-Echo signal provides greater T_2 -weighting compared to the SSFP-FID, especially at intermediate and high flip angles. In the special case of $\alpha = 90^\circ$, the ratio of both signals is given by

$$\frac{S_{\text{Echo}}}{S_{\text{FID}}} = \frac{1 - \sqrt{(1 - E_2^2) / (1 - E_1^2 E_2^2)}}{1 - E_1 \sqrt{(1 - E_2^2) / (1 - E_1^2 E_2^2)}}. \quad (4.42)$$

In the case of $T_R \ll T_1$ this yields the following relationship

$$\frac{S_{\text{Echo}}}{S_{\text{FID}}} \approx E_2^2 = e^{-2T_R/T_2}, \quad T_R \ll T_1, \quad (4.43)$$

showing that the SSFP-Echo is mainly the refocused SSFP-FID from the previous T_R -interval with a $T_E = 2 \cdot T_R$. As has been shown in [121] the combined acquisition of the SSFP-FID and SSFP-Echo might be applied for T_2 -quantification.

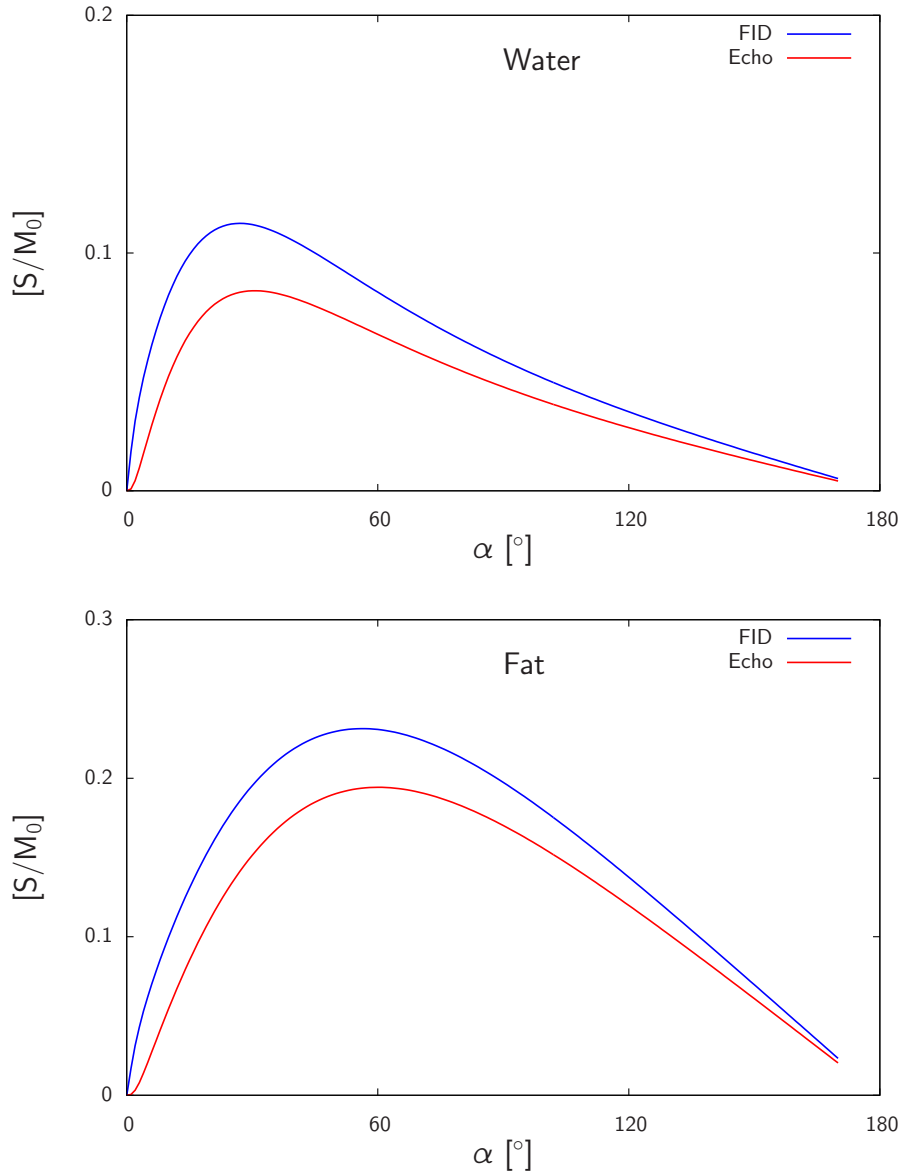


Figure 4.6: Evolution of the SSFP-FID and SSFP-Echo signal for different values of the relaxation times T_1 and T_2 for water protons (upper plot, $T_1 = 850$ ms, $T_2 = 90$ ms) and fat protons (lower plot, $T_1 = 300$ ms, $T_2 = 150$ ms) as function of the flip angle α . T_R was set to 10ms.

4.3.2 Balanced SSFP Sequence

The balanced SSFP sequence [122] (TrueFISP, FIESTA) is a special case of the SSFP sequence where the gradient area on any axis is not only equal during each T_R -interval but is also balanced, i.e. the area along each gradient axis is zero. If this condition is satisfied the SSFP-Echo and the SSFP-FID rephase at the same time TE and the so called balanced SSFP (bSSFP) signal is the coherent sum of the two signals. Since all gradients are rephased, $\Delta\omega \cdot t = 0$ and if we assume that our excitation pulse is around the y-axis we get for the steady-state magnetization if rephased at the center of the T_R -interval [123]

$$M_{bSSFP} = M_0 \frac{\sqrt{E_2(T_R)}(1 - E_1)\sin(\alpha)}{1 - (E_1 - E_2)\cos(\alpha) - E_1E_2}, \quad (4.44)$$

where we have assumed an alternating phase of the RF excitation pulses. In contrast to the spoiled GRE the signal is multiplied with a factor e^{-T_E/T_2} . The optimal flip angle depends on T_1 and T_2 and is given by

$$\cos(\alpha) = \frac{T_1/T_2 - 1}{T_1/T_2 + 1}, \quad (4.45)$$

which results in a signal amplitude of [124]

$$M_{bSSFP} = \frac{1}{2} M_0 \sqrt{T_2/T_1}. \quad (4.46)$$

The maximum achievable signal approaches 50% of M_0 , therefore offering the highest possible SNR per unit time of all sequences. For an optimized flip angle the images are T_2/T_1 -weighted. This type of mixed contrast has only limited application for diagnostic imaging, but is especially useful in applications, where fast image acquisitions are necessary such as functional and morphological cardiac imaging.

4.4 Formation of the SSFP Signal in the Presence of Diffusion

The signal of the SSFP sequence was derived in section 4.3. It was shown that the signal of the SSFP-Echo is a complicated sum of a spin echo and of many stimulated echoes. The diffusion-weighted signal of a spin-echo sequence was derived above. In this case, the diffusion attenuation is mainly limited by the echo time, which is especially important for short- T_2 tissues. It was shown in [55] that the diffusion sensitivity can be increased by extending the diffusion time Δ with a stimulated-echo

(STE) pulse sequence. The lowest-order STE forms after the third pulse. Therefore the diffusion time is longer than with the SE pulse sequence. Between the second and third pulse, relaxation is governed by T_1 relaxation only, hence, no significant signal loss due to relaxation occurs.

The method that is most sensitive to diffusion is therefore the SSFP sequence since it combines both SE and a sum of STEs. Therefore the signal formation is more complicated than in the simple SE and STE case. A first analysis of the effects of a constant field gradient on the SSFP signal in the context of NMR was performed by Kaiser et al. [125]. In the special case of a 90° pulse, only the spin echo and the primary stimulated echo contribute to the signal, leading to a bi-exponential signal attenuation [126]. Le Bihan et al. [127] derived the signal by incorporating diffusion effects in the steady state equations of the SSFP. In this analysis, however, the diffusion effect on higher order echos is not considered correctly. The first complete analysis of the diffusion-weighted SSFP signal was provided by Wu and Buxton [128]. In the following, the derivation of the DW-SSFP signal by Wu and Buxton will be summarized briefly. An alternative approach was described by Carney et al. [129] allowing for the implementation of arbitrary diffusion gradient profiles.

The DW-SSFP sequence corresponds to a series of RF pulses with a flip angle α around the x-axis separated by T_R . During each repetition, a single diffusion-gradient pulse of magnitude G and duration δ is applied at a time ϵ after the RF pulse. For simplicity, we assume that this is the only source of acquired precession, ignoring the effects of the gradients used for slice selection and k-space encoding. Accordingly, the position dependent precession angle is given by

$$\theta(\vec{r}) = -\gamma \vec{G} \cdot \vec{r} \delta. \quad (4.47)$$

Therefore, the position vector after application of the gradient can be substituted by the precession angle θ and the magnetization can be expressed as a Fourier series. We will derive expressions for the evolution of the magnetization before, during and after the application of the diffusion gradient and determine the coefficients of the Fourier series using boundary conditions. The evolution of the transverse magnetization in the presence of diffusion was derived in Eq. (3.23). We rewrite $M_\perp(\vec{r}, t)$ as $M_\perp(\theta, t)$ and for the different time intervals we set

$$M_\perp(\theta, t) = \begin{cases} \mu(\theta, t) \exp(-t/T_2) & 0 \leq t \leq \epsilon \\ \mu(\theta, t) \exp(-i\gamma \vec{G} \cdot \vec{r} \cdot (t - \epsilon) - t/T_2) & \epsilon \leq t \leq \epsilon + \delta \\ \mu(\theta, t) \exp(-i\gamma \vec{G} \cdot \vec{r} \cdot \delta - t/T_2) & \epsilon + \delta \leq t \leq T_R \end{cases} \quad (4.48)$$

Using the substitution of Eq. (4.47) in Eq. (3.23) we get for the first interval $0 \leq t \leq \epsilon$

$$\frac{\partial \mu}{\partial t} = D(\gamma G \delta)^2 \frac{\partial^2 \mu}{\partial \theta^2}. \quad (4.49)$$

This equation can be easily solved in Fourier space and the solution is the following Fourier integral

$$\mu(\theta, t) = \int_{-\infty}^{+\infty} a(k) \exp[-D(\gamma G \delta)^2 k^2 t] \exp(ik\theta) dk, \quad (4.50)$$

for $0 \leq t \leq \xi$. Similarly, we get

$$\mu(\theta, t) = \begin{cases} \int_{-\infty}^{+\infty} a'(k) \exp\left[-\frac{1}{3}D\delta(\gamma G \delta)^2 \left(k - \frac{t - \epsilon}{\delta}\right)^3\right] \\ \times \exp(ik\theta) dk & \text{for } \epsilon \leq t \leq \epsilon + \delta \\ \int_{-\infty}^{+\infty} a''(k) \exp[-D\delta(\gamma G \delta)^2 (k + 1)^2 t] \\ \times \exp(ik\theta) dk & \text{for } \epsilon + \delta \leq t \leq T_R. \end{cases} \quad (4.51)$$

The Bloch equation for the longitudinal equation is given by

$$\frac{\partial M_z}{\partial t} = \frac{M_0 - M_z}{T_1} + D\nabla^2 M_z. \quad (4.52)$$

If we define

$$M_z(\theta, t) = M_0 + \nu(\theta, t) \exp(-t/T_1), \quad (4.53)$$

in Eq.(4.52) the solution for $0 \leq t \leq T_R$ is given by

$$\nu(\theta, t) = \int_{-\infty}^{+\infty} c(k) \exp(-D(\gamma G \delta)^2 k^2 t) \exp(ik\theta) dk, \quad (4.54)$$

assuming that M_0 is spatially uniform. Since M_\perp is a periodic function of θ and M_z is an even periodic function when the gradient is off, the Fourier integrals can be

reduced to a Fourier series

$$M_{\perp}(\theta, t) = \begin{cases} e^{-t/T_2} \sum_{k=-\infty}^{+\infty} a(k) \exp[-D(\gamma G \delta)^2 k^2 t] e^{ik\theta} & 0 \leq t \leq \epsilon \\ e^{-\epsilon/T_2} \sum_{k=-\infty}^{+\infty} a'(k) \exp[-\frac{1}{3}D\delta(\gamma G \delta)^2 k^3] e^{ik\theta} & t = \epsilon \\ e^{-(\epsilon+\delta)/T_2} \sum_{k=-\infty}^{+\infty} a'(k) \exp[-\frac{1}{3}D\delta(\gamma G \delta)^2 (k+1)^3] e^{i(k+1)\theta} & t = \epsilon + \delta \\ e^{-t/T_2} \sum_{k=-\infty}^{+\infty} a''(k) \exp[-D(\gamma G \delta)^2 (k+1)^2 t] e^{i(k+1)\theta} & \epsilon + \delta \leq t \leq T_R \end{cases} \quad (4.55)$$

and

$$M_z(\theta, t) = M_0 + e^{-t/T_1} \sum_{k=0}^{\infty} c(k) \exp[-D(\gamma G \delta)^2 k^2 t] \cos(k\theta) \quad 0 \leq t \leq T_R. \quad (4.56)$$

The magnetization is a continuous function leading to the following boundary conditions

$$M_{\perp}(\theta, \epsilon^-) = M_{\perp}(\theta, \epsilon^+) \quad (4.57)$$

$$M_{\perp}(\theta, \epsilon + \delta^-) = M_{\perp}(\theta, \epsilon + \delta^+). \quad (4.58)$$

The orthogonality of $e^{ik\theta}$ implies the following relationships between the Fourier coefficients

$$a(k) \exp[-D(\gamma G \delta)^2 k^2 \epsilon] = a'(k) \exp\left[-\frac{1}{3}D\delta(\gamma G \delta)^2 k^3\right] \quad (4.59)$$

$$a'(k) \exp\left[-\frac{1}{3}D\delta(\gamma G \delta)^2 (k+1)^3\right] = a''(k) \exp[-D(\gamma G \delta)^2 (k+1)^2 \epsilon], \quad (4.60)$$

yielding

$$a'(k) = a(k)G_{2,k} \quad \text{with} \quad G_{2,k} = \exp\left[-D(\gamma G \delta)^2 k^2 \left(\epsilon - \frac{k\delta}{3}\right)\right] \quad (4.61)$$

$$a''(k) = a(k)H_{2,k} \quad \text{with} \quad H_{2,k} = \exp\left[D(\gamma G \delta)^2 \left(\delta \left(k + \frac{2}{3}\right) + \epsilon(2k+1)\right)\right]. \quad (4.62)$$

Since the RF pulse is applied along the x-axis at $t = 0$ the x-component of the

transverse magnetization is an odd function while the y-component is even. Thus all coefficients $a(k)$, and consequently all $a'(k)$ and $a''(k)$ are imaginary. Defining $b_k = -ia(k)$, $b_k \in \mathbb{R}$ the x- and y-component can be written as

$$M_x(\theta, t) = \begin{cases} -\sum_{k=-\infty}^{\infty} b_k E_{2,k}(t) \sin(k\theta) & 0 \leq t \leq \epsilon \\ -\sum_{k=-\infty}^{\infty} b_k E'_{2,k}(t) \sin\left[\left(k + \frac{t-\epsilon}{\delta}\right)\theta\right] & \epsilon \leq t \leq \epsilon + \delta \\ -\sum_{k=-\infty}^{\infty} b_k E''_{2,k}(t) \sin[(k+1)\theta] & \epsilon + \delta \leq t \leq T_R \end{cases} \quad (4.63)$$

$$M_y(\theta, t) = \begin{cases} \sum_{k=-\infty}^{\infty} b_k E_{2,k}(t) \cos(k\theta) & 0 \leq t \leq \epsilon \\ \sum_{k=-\infty}^{\infty} b_k E'_{2,k}(t) \cos\left[\left(k + \frac{t-\epsilon}{\delta}\right)\theta\right] & \epsilon \leq t \leq \epsilon + \delta \\ \sum_{k=-\infty}^{\infty} b_k E''_{2,k}(t) \cos[(k+1)\theta] & \epsilon + \delta \leq t \leq T_R \end{cases} \quad (4.64)$$

and the z-component as

$$M_z(\theta, t) = M_0 + \sum_{k=0}^{\infty} c_k E_{1,k}(t) \cos(k\theta) \quad \text{for } 0 \leq t \leq T_R, \quad (4.65)$$

where

$$E_{1,k}(t) = \exp\left(-\left[\frac{1}{T_1} + D(\gamma G \delta)^2 k^2\right] t\right), \quad (4.66)$$

$$E_{2,k}(t) = \exp\left(-\left[\frac{1}{T_2} + D(\gamma G \delta)^2 k^2\right] t\right), \quad (4.67)$$

$$E'_{2,k}(t) = G_{2,k} \exp\left[-\frac{t}{T_2} - \frac{1}{3} D \delta (\gamma G \delta)^2 \left(k + \frac{t-\epsilon}{\delta}\right)^3\right], \quad (4.68)$$

$$E''_{2,k}(t) = H_{2,k} \exp\left(-\left[\frac{1}{T_2} + D(\gamma G \delta)^2 (k+1)^2\right] t\right). \quad (4.69)$$

Finally we can apply the steady-state condition yielding

$$\begin{pmatrix} M_x(\theta, T_R^-) \\ M_y(\theta, T_R^-) \\ M_z(\theta, T_R^-) \end{pmatrix} = \begin{pmatrix} 1 & 0 & 0 \\ 0 & \cos(\alpha) & -\sin(\alpha) \\ 0 & \sin(\alpha) & \cos(\alpha) \end{pmatrix} \begin{pmatrix} M_x(\theta, 0^+) \\ M_y(\theta, 0^+) \\ M_z(\theta, 0^+) \end{pmatrix} \quad (4.70)$$

Based on these equations, the coefficients b_k and c_k can be determined. For the

x-component we get

$$\sum_{k=-\infty}^{\infty} b_k E_{2,k}(0) \sin(k\theta) = \sum_{k=-\infty}^{\infty} b_{k-1} E_{2,k-1}''(T_R) \sin(k\theta). \quad (4.71)$$

This condition must hold for all values of θ and therefore taking into account the orthogonality of $\sin(k\theta)$ and $\cos(k\theta)$ and $E_{2,k} = 0$ and setting $E_{i,k}(T_R) = E_{i,k}$ we get for each $p = |k|$

$$b_p - b_{-p} = b_{p-1} E_{2,p-1}'' - b_{p-1} E_{2,p-1}'' \quad \text{for } p > 0. \quad (4.72)$$

For the y- and z-component similar conditions follow. In summary the coefficients must satisfy the following equations:

For $p = 0$:

$$-b_{-1} E_{2,-1} + b_0 \cos(\alpha) - c_0 \sin(\alpha) = M_0 \sin(\alpha) \quad (4.73)$$

$$b_0 \sin(\alpha) + c_0 [\cos(\alpha) - E_{1,0}] = M_0 [1 - \cos(\alpha)] \quad (4.74)$$

For $p > 0$:

$$c_p = \frac{(b_p + b_{-p}) \sin(\alpha)}{E_{1,p} - \cos(\alpha)} \quad (4.75)$$

and using Eq. (4.72) and (4.75)

$$\begin{aligned} b_p (\cos(\alpha) + 1) (E_{1,p} - 1) + b_{-p} (\cos(\alpha) - 1) (E_{1,p} + 1) \\ = 2b_{p-1} E_{2,p-1}'' (E_{1,p} - \cos(\alpha)) \end{aligned} \quad (4.76)$$

$$\begin{aligned} b_p (\cos(\alpha) - 1) (E_{1,p} + 1) + b_{-p} (\cos(\alpha) + 1) (E_{1,p} - 1) \\ = 2b_{-p-1} E_{2,-p-1}'' (E_{1,p} - \cos(\alpha)). \end{aligned} \quad (4.77)$$

The structure of these equations suggests a solution in the form of two series

$$b_p = F_p b_{p-1} \quad \text{and} \quad b_{-p-1} = F_p b_{-p}, \quad p > 0. \quad (4.78)$$

The first series begins with b_0 and contains the b_p , while the second series begins with b_{-1} and contains the b_{-p} . Eq. (4.73) provides the link between both starting values. Plugging Eq. (4.78) into (4.76) and (4.77) two equations for b_p and b_{-p} arise.

Solving the linear system of equations yields the following quadratic equation for F_p

$$F_p^2 - 2F_p \frac{1 - E_{1,p} \cos(\alpha) - E''_{2,p-1} E''_{2,-p-1} (E_{1,p} - \cos(\alpha))}{E''_{2,-p-1} (\cos(\alpha) + 1) (1 - E_{1,p})} + \frac{E''_{2,p-1}}{E''_{2,-p-1}} = 0. \quad (4.79)$$

The product of both roots equals $E''_{2,p-1}/E''_{2,-p-1} > 0$ and thus both roots are positive. The solutions of Eq. (4.73) to (4.77) can be determined. Starting with Eq. (4.76) for $p = 1$ we get

$$b_{-1} = b_0 \frac{2E_{2,0} (E_{1,1} - \cos(\alpha)) + (\cos(\alpha) + 1) (1 - E_{1,1})}{(\cos(\alpha) - 1) (E_{1,1} + 1)}. \quad (4.80)$$

This can be simplified using Eq. (4.79)

$$b_{-1} = b_0 \frac{F_1 - E_{2,0}}{1 - F_1 E_{2,-2}}. \quad (4.81)$$

Since $F_1 < E_{2,0} < 1$, this shows that the starting values and consequently all members of the two series b_p and b_{-p} are of opposite sign. Eq. (4.73) and (4.74) and (4.81) can now be solved and we get

$$b_0 = M_0 (1 - E_{1,0}) \sin(\alpha) \frac{(1 - F_1 E''_{2,-2})}{r - F_1 s}, \quad (4.82)$$

$$b_{-1} = M_0 (1 - E_{1,0}) \sin(\alpha) \frac{F_1 - E''_{2,0}}{r - F_1 s}, \quad (4.83)$$

$$c_0 = \frac{M_0 (1 - \cos(\alpha)) - b_0 \sin(\alpha)}{\cos(\alpha) - E_{1,0}}, \quad (4.84)$$

where

$$r = 1 - E_{1,0} \cos(\alpha) + E''_{2,0} E''_{2,-1} (\cos(\alpha) - E_{1,0}) \quad (4.85)$$

$$s = E''_{2,-2} (1 - E_{1,0} \cos(\alpha)) + E''_{2,-1} (\cos(\alpha) - E_{1,0}). \quad (4.86)$$

All b_p and b_{-p} can now be determined by repeated application of Eq. (4.78). The c_p then follow from Eq. (4.75). If we assume that the precession angle in each voxel is distributed uniformly from 0 to 2π the average magnetization within each voxel

immediately after the RF pulse (corresponding to the SSFP-FID (4.38)) is given by

$$\langle M_y(0^+) \rangle = \frac{1}{2\pi} \int_0^{2\pi} M_y(\theta, 0^+) d\theta = b_0 \quad (4.87)$$

$$\langle M_x(0^+) \rangle = 0, \quad (4.88)$$

and the signal immediately before the RF pulse (corresponding to the SSFP-Echo (4.39)) by

$$\langle M_y(0^-) \rangle = \frac{1}{2\pi} \int_0^{2\pi} M_y(\theta, T_R^-) d\theta = b_{-1} E_{2,-1}''(T_R) \quad (4.89)$$

$$\langle M_x(0^-) \rangle = 0. \quad (4.90)$$

The signal immediately after the RF pulse consists of the FID and multiple-path echoes, and only the echoes are affected by diffusion. The signal before the RF pulse is made purely of echoes and thus the entire signal is affected by diffusion. In Fig. 4.7 the behavior of both signals as a function of the flip angle is shown. The signal is maximized for $\alpha \approx 40^\circ$. The DW-SSFP-FID signal amplitude is roughly twice the amplitude of the DW-SSFP-Echo signal. However the diffusion sensitivity is more pronounced in the case of the DW-SSFP-Echo. In the case of the DW-SSFP-FID the signal decreases by 38% when increasing the duration of the diffusion gradient from $\tau = 0.5$ to 9.0 ms. In the case of the DW-SSFP-Echo a signal drop of 76% can be observed. Therefore the DW-SSFP-Echo, known also as DW-PSIF, is better suited to measure diffusion-weighted images with a SSFP sequence and in the following we will concentrate on the DW-PSIF signal. Buxton [62] provided a compact notation of the DW-PSIF signal assuming $\epsilon = 0$, which we corrected for errors²

$$M_{\perp}^- = - \frac{M_0 (1 - E_1) E_2 A_2^{1/3} (F_1 - E_2 A_1 A_2^{-2/3}) \sin(\alpha)}{r - F_1 s} \quad (4.91)$$

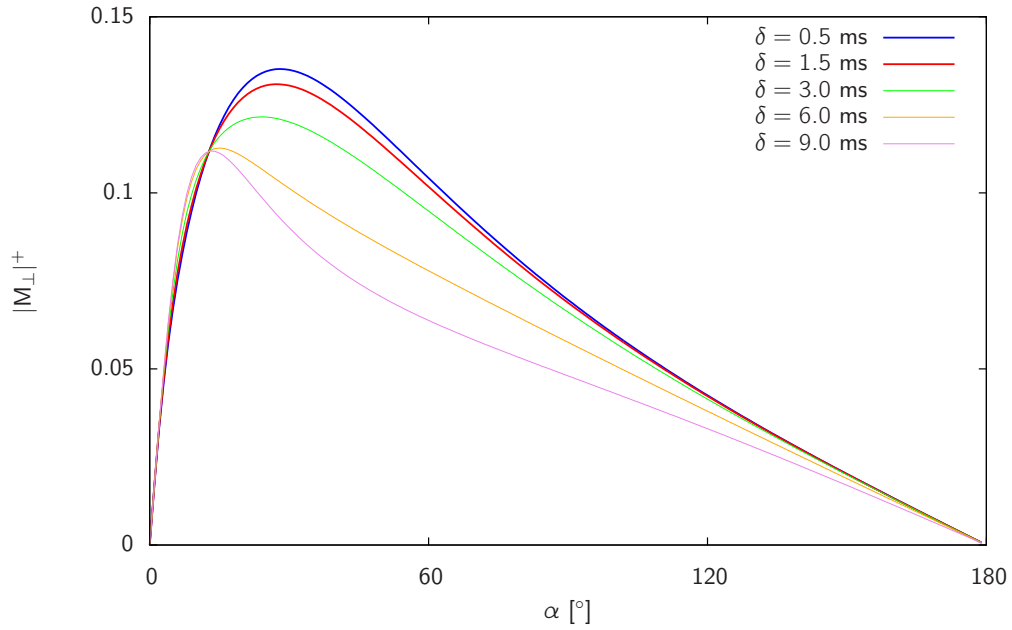
²The signs in the exponents of A_2 and A_1 were inverted, in the numerator the first $A_2^{-2/3}$ was substituted by $A_2^{1/3}$, and in the formula of s , the last 1 was substituted by E_1 .

with

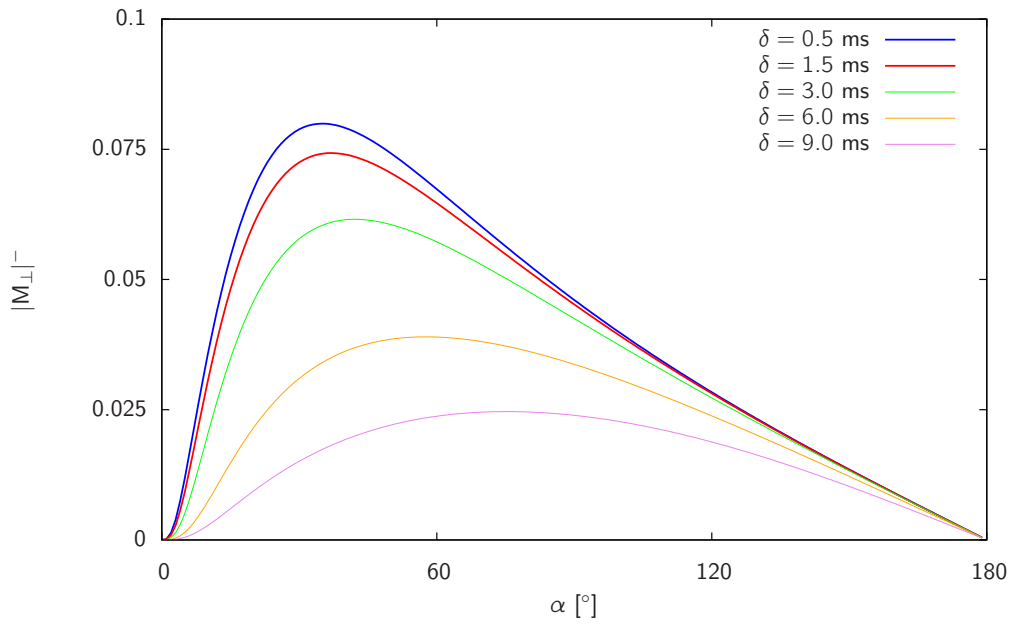
$$\begin{aligned}
 F_1 &= K - \sqrt{K^2 - A_2^{-2}}, \\
 K &= \frac{1 - E_1 A_1 \cos(\alpha) - E_2^2 A_1^2 A_2^{2/3} (E_1 A_1 - \cos(\alpha))}{E_2 A_1 A_2^{4/3} (\cos(\alpha) + 1) (1 - E_1 A_1)}, \\
 r &= 1 - E_1 \cos(\alpha) + E_2^2 A_1 A_2^{-1/3} (\cos(\alpha) - E_1), \\
 s &= E_2 A_1 A_2^{4/3} (1 - E_1 \cos(\alpha)) + E_2 A_2^{1/3} (\cos(\alpha) - E_1), \\
 A_1 &= \exp(-(\gamma G \delta)^2 T_R \cdot D), \quad A_2 = \exp(-(\gamma G \delta)^2 \delta \cdot D), \\
 E_1 &= \exp(-T_R/T_1), \quad E_2 = \exp(-T_R/T_2).
 \end{aligned}$$

A better understanding of the strong diffusion sensitivity of the DW-PSIF signal can be obtained via a simplified partition analysis of the magnetization [130, 125, 62]. It is assumed that spins dephased by the diffusion-gradient are rephased by a second diffusion gradient later in the sequence scheme; however, not necessarily during the subsequent repetition interval. This is illustrated in the pictorial phase diagram in Fig. 4.8 [131]. The first diffusion gradient (gray box) adds an extra phase to the spins (indicated by the first ramp in the diagram). The next RF pulse partially reverts the phase, leaves other spins in their current state and rotates a fraction of the spins into the longitudinal direction (indicated by the gray line; these spins cannot be dephased by the following gradient and are only effected by longitudinal relaxation). Only the reverted spins form the first spin echo, SE_1 , after the second diffusion gradient and the diffusion-sensitizing duration $\Delta = T_R$; the other spins remain dephased in evolve further until the next RF pulse acts on them. Again, some spins are flipped by 180° , some are left unchanged, and some are moved from the longitudinal direction back into the traversal plane. The last group forms the first stimulated echo (STE_1) in the following cycle and has experienced a diffusion-sensitizing duration of $\Delta = 2T_R$. Other spins are rephased even later. The steady-state that establishes after a number of RF pulses is therefore a combination of echoes which have experienced very different diffusion-sensitizing durations. Hence, the calculation of the signal of the DW-PSIF is very complicated as shown above and is a complicated function of not only the diffusion coefficient D but also the relaxation times T_1 and T_2 as well as of the sequence parameters T_E , T_R and α . Typical T_R are in the range of 20 – 30 ms and, consequently, a relatively fast image acquisition is possible. Therefore, the SSFP sequence is relatively insensitive to the influence of bulk motion. Based on the signal function in Eq. (4.91), the variation as a function of the relaxation times and the

input parameters was simulated and the results are shown in Fig. 4.9. It can be seen in (a) that the degree of diffusion weighting is decreasing with an increasing longitudinal relaxation time. In contrast, for an increasing value of the transverse relaxation time the signal attenuation due to the diffusion gradient is increasing (b). As expected for increasing values of D the signal attenuation as a function of the diffusion gradient duration is strongly increased.



(a) DW-SSFP-FID



(b) DW-SSFP-Echo

Figure 4.7: Simulation of the transverse magnetization of a diffusion-weighted SSFP sequence as a function of the flip angle for different durations of the diffusion gradient. In (a) the magnetization immediately after and in (b) immediately before the RF pulse are shown. Assumed parameters are $T_1 = 1000$ ms, $T_2 = 125$ ms, $T_R = 25$ ms, $D = 3.0 \times 10^{-3}$ mm²/s, $\epsilon = 1$ ms and $G = 23$ mT/m.

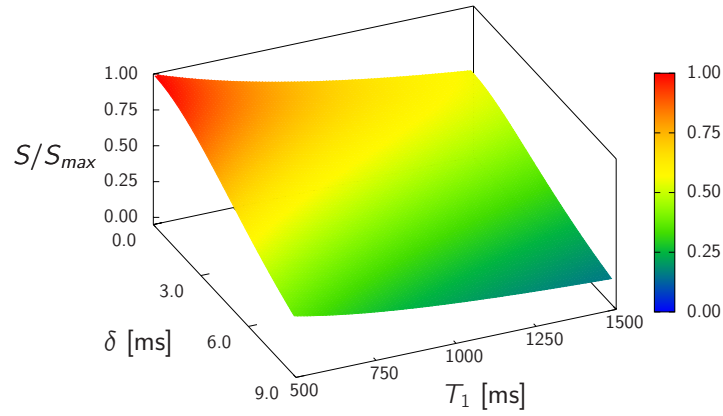
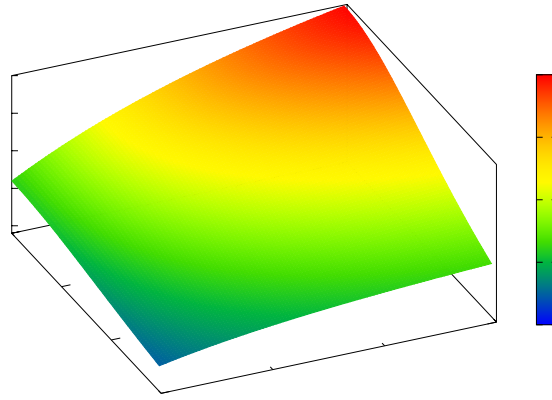
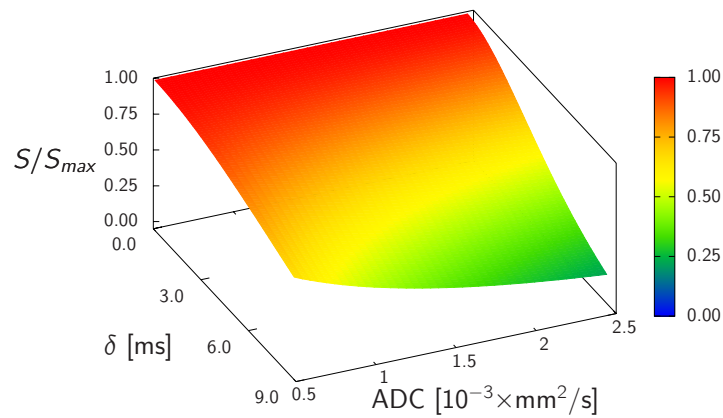
(a) δ vs T_1 (b) δ vs T_2 (c) δ vs ADC

Figure 4.9: Signal simulation of the DW-PSIF signal as a function of the duration of the diffusion gradient δ vs (a) T_1 , (b) T_2 and (c) the ADC-value. The fixed parameters were set to: $T_1 = 850$ ms, $T_2 = 125$ ms, $ADC = 1.5 \cdot 10^{-3}$ mm²/s, $T_R = 25$ ms, $\alpha = 40^\circ$ and $G = 23$ mT/m.

Chapter 5

DW-SSFP in Vertebral Fractures

In section 3.3, the results of previous studies, that successfully applied the DW-SSFP sequence for the differentiation of vertebral compression fractures caused by osteoporosis or malignant infiltration, were discussed. In all these studies, the differentiation was based on a qualitative evaluation of the DW-SSFP images, i.e. the contrast between vCFs and non-fractured vertebrae. All studies used the PSIF type of the DW-SSFP sequence, acquiring the images shortly before the application of the RF pulse, since this sequence provides the largest diffusion weighting. Hence, in the following we will focus on the DW-PSIF sequence. In general, osteoporotic vCFs appeared hypo- or isointense compared to normal-appearing vBM, whereas vCFs caused by malignant infiltration appeared hyperintense. The results of quantitative measurements of the ADCs in the lesions might be able to explain why osteoporotic vCFs appear hypointense. Since the ADC was found to be significantly increased in the fractures compared to normal-appearing vBM, the signal is expected to be attenuated in vCF on diffusion-weighted images. However, the measured ADCs in malignant vCFs are also significantly increased compared to normal-appearing vBM in contradiction to the findings on DW-PSIF images that malignant lesions appear hyperintense. Hence, the signal contrast of the DW-PSIF cannot be explained solely by the different diffusion characteristics, but also depends on additional parameters.

In section 4.4, we derived the signal function of the DW-SSFP and showed that the signal is a complicated function of the ADC as well as of the relaxation times T_1 and T_2 . In vBM, the situation is even more complicated, since the measured signal is a combination of the signal of the fat component and the water component. Therefore, the signal depends on the relative ratios of fat (f_{fat}) and water (f_{wat}) and the ADCs as well as the relaxation times of both components. As mentioned in section 4.1, if the ratios of fat and water are at the same order of magnitude the signal is also

strongly dependent on the chosen T_E , i.e. whether an opposed-phase, an in-phase or a mixed signal is acquired. In summary, for a quantitative analysis providing an explanation for the signal contrast described above, it is necessary to determine at least 9 parameters:

- T_{1wat} and T_{1fat}
- T_{2wat} and T_{2fat}
- T_{2wat}^* and T_{2fat}^*
- ADC_{wat} and ADC_{fat}
- f_{wat} or f_{fat} .

So far, the origin of the signal contrast between vCFs and normal-appearing vBM on DW-PSIF images has not been studied based on a detailed analysis of the signal function. Hence, it remains unclear how strongly each of the parameters listed above contributes to the different signal characteristics between normal and abnormal vBM. The theoretical treatment of the DW-PSIF requires the separate measurement of these parameters in vCF as well as in normal-appearing vBM. In this section, we will investigate the signal characteristics in a collective of patients with benign and malignant vCFs. First, we will present the methodologies used for the determination of the physical parameters listed above and briefly discuss the results. A detailed analysis with regard to the analysis of these parameters in normal-appearing vBM and vCFs can be found in Biffar et al. [29]. Using these parameters, we will perform simulations of the DW-PSIF signal in vBM, intervertebral discs and vCFs. Based on the results, we identify the origin of the signal contrast. Afterwards, we will present the results of the DW-PSIF measurements and compare them to the signal simulations.

5.1 Patient Collective

After internal review board approval and informed consent had been received, the protocol was applied to 40 patients, who were examined at our hospital within a time period of 20 months for suspected acute vertebral fracture caused by osteoporosis or malignant infiltration. The patient collective was divided into two groups. Group 1 consisted of 20 benign fractures in 20 patients with osteoporosis (14 women and 6 men, median age: 72 years, range: 52-86 years). The presence of a tumor in these patients was ruled out by follow-up MR examinations or multidetector computed tomography (CT) examinations. In case of a finding of fracture of unclear etiology

or an unclear bone-marrow lesion, histological clarification was obtained ($n = 2$) and no malignancy was found. Group 2 consisted of 20 malignant infiltrations in 20 patients (10 women and 10 men, median age: 60 years, range: 25-87 years) accompanied by pathological fractures in 13 of these 20 cases. Primary neoplasms included breast cancer ($n=6$), plasmacytoma ($n=4$), adenocarcinoma ($n=3$), ovarian cancer ($n=1$), hypopharyngeal cancer ($n=1$), thyroid carcinoma ($n=1$), bladder cancer ($n=1$), pancreatic cancer ($n=1$), lung cancer ($n=1$) and non-seminoma ($n=1$). The diagnoses were confirmed by histopathological examination of specimens obtained during surgery, CT-guided biopsy, or follow-up MR examinations. Exclusion criteria for the participation in the study were (1) the absence of acute bone-marrow edema in fracture sites; (2) a contraindication to MR examination; or (3) an incomplete MR examination.

All patients underwent MRI of the spine to assess the level and degree of the suspected fracture and acute bone-marrow edema. The fracture site and bone marrow edema were defined by two radiologists with 10 and 7 years of experience in musculoskeletal imaging in consensus. Acute osteoporotic fracture was diagnosed according to MR-specific criteria and correlation with additionally available studies, including conventional imaging and computed tomography. MR-specific criteria indicating acute fracture were a hyperintense fluid-like signal within a visible fracture cleft on T2-weighted TSE and STIR-imaging as well as a hyperintense bone-marrow edema within the affected vertebra, which corresponded to a hypointense signal of the affected bone marrow compared to the physiological hyperintense bone-marrow fat signal in T1-weighted TSE-sequences. In order to differentiate the fracture types on the morphological images, established criteria describing the osteoporotic nature of a fracture were used, such as the fluid sign or ground- and endplate impression fracture pattern. Signs indicating a malignant fracture or infiltration included solid, enhancing soft-tissue components or clear signs of infiltration into the vertebral arch, prominent posterior vertebral bulging or paravertebral or intraspinal infiltration.

5.2 Morphological Imaging

Measurements were performed on a 32-channel 1.5-T whole-body scanner (MAGNETOM Avanto, Siemens Healthcare, Erlangen, Germany). For signal reception, a quadrature spine surface coil was used. Prior to the quantitative and DW-PSIF measurements, T1-weighted (TR/TE, 531/12 ms), STIR (TR/TE/TI, 3790/61/180 ms) and T2-weighted (TR/TE, 4420/118 ms) turbo spin-echo images of 21 sagittal slices with a slice thickness of 3.0 mm were acquired using a $44 \times 44 \text{ cm}^2$ FOV and a

matrix size of 384×384 . The total acquisition time for these morphological images was 6:30 min. These pre-contrast images were used for lesion localization and proper slice positioning of the following quantitative measurements.

The classification of the vertebrae into the categories normal or abnormal appearing vBM was accomplished according to their appearance on the T_1 -weighted, T_2 -weighted and STIR-images by the consensus decision of two experienced radiologists. Old fractures (without any signs of bone-marrow edema on the STIR-image) or diffusely infiltrated vertebrae (manifested as a homogeneous signal reduction on unenhanced T_1 -weighted images) were excluded from the analysis. For the analysis of the signal in the intervertebral discs, those showing signs of degeneration either in form of a dehydration of the nucleus pulposus, indicated by a signal loss on T_2 -weighted images, or by clefts in the annulus fibrosus, showing an increased signal on contrast-enhanced T_1 -weighted images, were excluded.

5.3 T_1 Quantification

The longitudinal relaxation time, T_1 , describes the effect of the regrowth of the longitudinal magnetization after the application of an RF pulse. Due to the spin-lattice interaction, i.e. interactions between the spins and their surroundings, the magnetization realigns with the external B_0 field. In general, T_1 relaxation times in the body at 1.5 T are in the order of 1 s, i.e., 8 orders of magnitude longer than the precession period. The mechanism by which the spins relax is magnetic. As a water molecule tumbles due to thermal motions, it experiences a fluctuating magnetic field. The primary source of the fluctuating fields is the dipolar coupling between the nuclei. An oscillating magnetic dipolar field at the resonance frequency, $\omega_0 = \gamma B_0$, couples to the nucleus which can exchange energy with the field as it flips. Therefore, longitudinal relaxation is only effective if the frequency of the rotational motion of the molecules is equal to the resonance frequency. The spectrum of the rotational frequencies of the molecules depends on various parameters, like temperature, viscosity or the size of the molecules. Hence, the longitudinal relaxation times strongly vary between different tissues [132] as is demonstrated by e.g. fat (≈ 250 ms) and free water ($\approx 2000 - 3000$ ms). T_1 -weighted images of the spine provide a strong contrast between the hyperintense vertebrae dominated by the fat signal (short T_1) and the hypointense intervertebral discs dominated by the water signal (long T_1). Just recently, it has been shown by Hu et al. [133] that the T_1 relaxation times of fat and water depend on the mixture composition of fat and water. For both T_1 values, a decrease along with an increase of the fat fraction was

observed. In order to understand the influence of T_1 on the DW-PSIF signal, it is necessary to determine the exact values of the water as well as of the fat component.

For the measurement of the T_1 relaxation time, a saturation-recovery (SR) half-Fourier-acquisition single-shot turbo-spin-echo (HASTE) sequence was used (saturation times $T_I=5, 50, 100, 200, 400, 800, 1600, 3200$ ms). To determine the T_1 of the water component, the image acquisition was preceded by a fat-saturation pulse and for the fat component by a water-saturation pulse, respectively. The matrix size was 128×92 pixels and the receiver bandwidth was 735 Hz/pixel. T_E was fixed to 14 ms for the SR T_1 measurements (T_R is irrelevant in SR experiments). 2 averages were acquired for each T_I in order to increase the SNR.

For quantification of the T_1 relaxation times, ROIs were drawn manually in the lesions according to their appearance on the fat-saturated image with the longest saturation time. One ROI in a normal-appearing vertebrae and one in an intervertebral disc were selected on the water-saturated image with the longest saturation time, which provided the best contrast between vertebral bodies and intervertebral discs. The location of all ROIs was verified on the anatomical images. To determine T_1 , the mean signal intensity values of the ROIs for varying saturation times were fitted to a monoexponential saturation-recovery model of the longitudinal magnetization [113]. In vCFs, T_1 relaxation times of the fat component could not be determined, as the water-saturated signal was too low because of the negligible fat fraction, see section 5.7. An exemplary fit of the model to the signal data in normal-appearing vBM, an iVD and a vCF and the corresponding fat-saturated image with the longest saturation time are shown in Fig. 5.1.

In Fig. 5.2, maps of T_1 acquired pixel-wise are shown for two patients with a benign and a malignant fracture. On these maps, only the values in normal-appearing vBM and in vCF are shown. It can be seen in the case of the patient with the malignant lesion that the values of T_{1water} in the vCF are similar to those of T_{1fat} . This is caused by an incomplete fat suppression. Since there is almost no fat in the lesion the measured signal corresponds to the not-suppressed water signal. In the case of the osteoporotic vCF the determination of T_{1fat} , is also not reliable. The calculated values correspond to a mixture of the very small fat and non-suppressed water signal. The mean values and standard deviations of the T_1 -values in normal-appearing vBM, iVDs and in vCFs are summarized in Table 5.1. Box-plots of the values in measured in fat and water are shown in Fig. 5.3. The T_1 -values of the water component were found to be significantly longer in vCFs compared to normal-appearing vBM (malignant: 1264 vs. 927 ms, osteoporotic: 1331 vs. 925 ms). The values in the iVD were significantly increased compared to normal-appearing vBM in

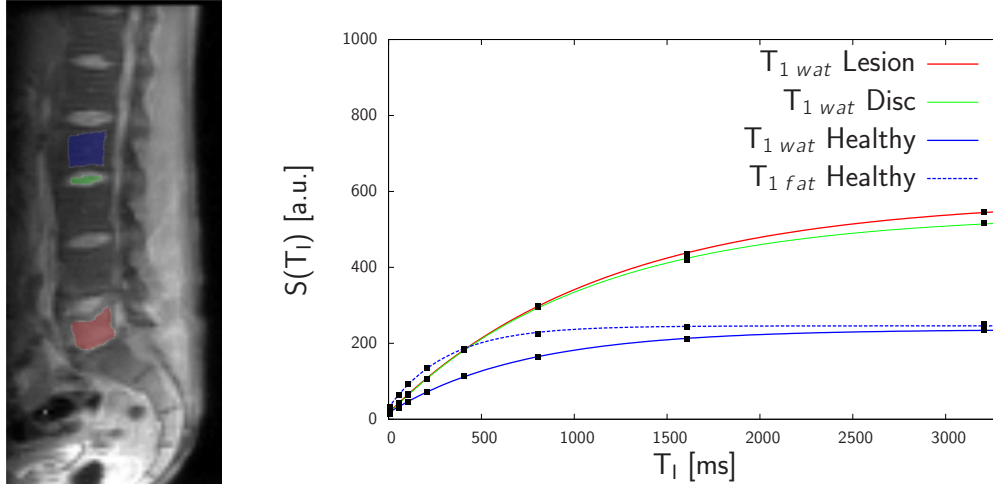


Figure 5.1: Reference image and the corresponding fit to a saturation- recovery model for a patient with a malignant lesion in L5. Shown are the fit for the water component in the lesion and the intervertebral disc between L3 and L2 and for the water and fat component in normal-appearing vBM in L2. The reference image corresponds to the fat-saturated image with $T_I = 3200$ ms

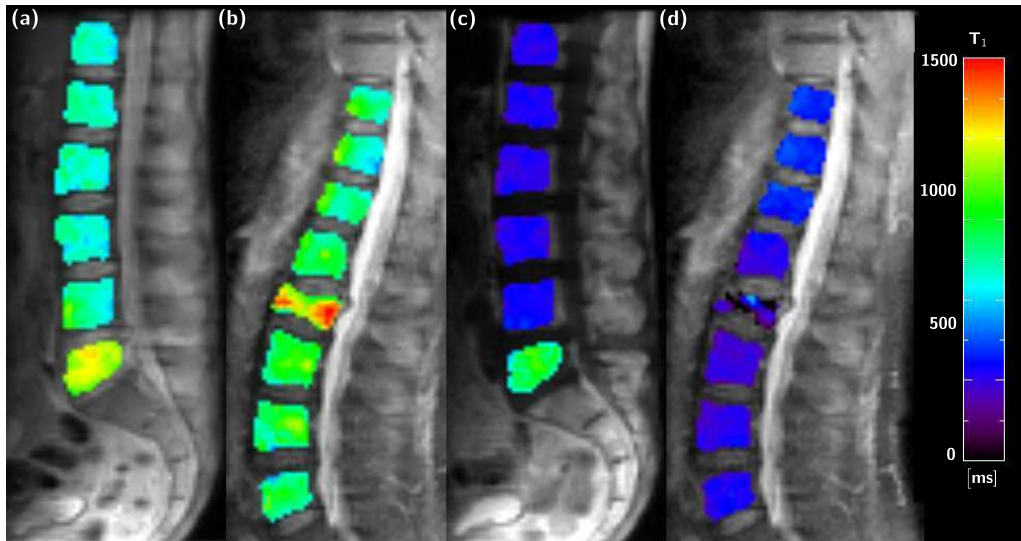


Figure 5.2: T_1 -map of the water component in a patient with (a) a vCF in L5 caused by malignant infiltration and (b) a vCF in L1 caused by osteoporosis. In (c) and (d), the maps of T_{1fat} in the corresponding patients are shown.

patients with a malignant lesion. A significant difference between the T_1 of the iVD in patients with a malignant or an osteoporotic vCF was found. The values in normal-appearing vBM agree with the measurements of Träber et al. [134]. The T_1 values of the fat component (386 and 324 ms) are somewhat higher than those of 260 –

290 ms obtained in [134, 135]. Träber et al. performed a spectroscopic measurement, which does not suffer from any imperfect suppression effects. Gold et al. [135] used a spectral-spatial excitation pulse.

It was shown by Sugimura et al. [136] at 0.15T that bulk T_1 of malignant metastatic lesions was longer than that of non-neoplastic. Träber et al. at 1.5T reported an increase in T_1 of water of 16 % in malignant lesions compared with normal vBM. We found an increase of 43 % in malignant lesions compared with normal-appearing vBM in the same patient, possibly explained by the higher ratio of free to fixed water in tumors. Ito et al. [137] found a positive correlation between the bone mineral density and T_1 of water at 1.5T. Conversely, Träber et al. found no significant differences between normal-appearing vBM of patients with and without osteoporosis. This agrees with our results, showing no significant differences between T_1 in normal-appearing vBM of patients with osteoporosis and those with malignant lesions.

Pathology	Osteoporosis ($n = 20$)		
Region	vBM	iVD	vCF
T_{1wat} [ms]	925 (101)	955 (140)	1331 (170)
T_{1fat} [ms]	279 (30)	–	–

Pathology	Malignant ($n = 20$)		
Region	vBM	iVD	vCF
T_{1wat} [ms]	927 (108)	1112 (215)	1264 (150)
T_{1fat} [ms]	375 (118)	–	–

Table 5.1: Summary of the mean values and standard deviations (shown in parentheses) of T_{1wat} and T_{1fat} .

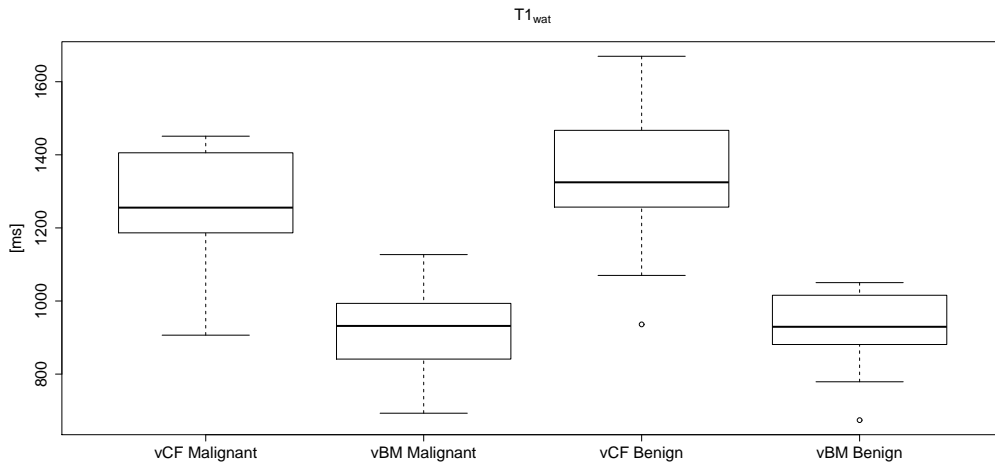
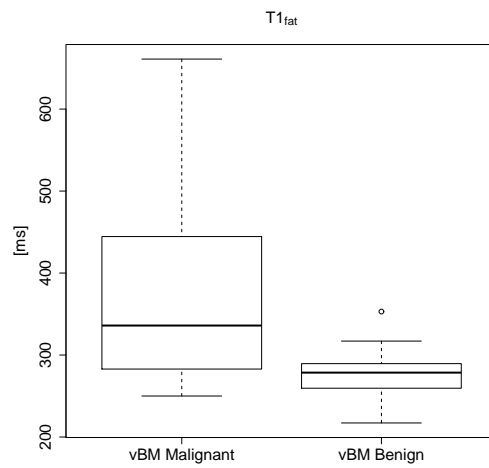
(a) T_{1wat} (b) T_{1fat}

Figure 5.3: Box-plots of (a) T_{1wat} values in normal-appearing vBM and vCFs and of (b) T_{1fat} values in normal-appearing vBM.

5.4 T_2 Quantification

The transversal relaxation time, T_2 , describes the decay of the transversal magnetization after the application of an RF pulse. Immediately after the excitation, the transverse magnetization consists of a coherent set of spins precessing together in phase. However, as mentioned in section 5.3, in addition to the primary magnetic field B_0 , each dipole also feels a fluctuating field from the magnetic moments of other nuclei. The z-component of this field adds to (or subtracts from) B_0 and so locally alters the precession rate and the rate of the precessional motion of the spins is randomly distributed. This distribution leads to a phase dispersion, which causes an attenuation of the transverse magnetization. In contrast to the longitudinal relaxation, the transverse relaxation is mainly caused by the average of the fluctuations over time, i.e. field fluctuations at zero frequency. This explains why the transverse relaxation is more or less independent of the magnetic field strength and is in general about 10 times shorter than T_1 in the body. As in the case of T_1 , the T_2 -values of fat (≈ 60 ms) and water ($\approx 500 - 1400$ ms) differ significantly, and in order to understand their influence on the DW-PSIF signal, it is necessary to determine the exact values of the water as well as of the fat component.

For T_2 determination of the water and fat component, a HASTE sequence with varying echo times ($T_E = 14, 28, 69, 99, 130, 170$ ms) was used, preceded by either a fat- or water-saturation pulse, respectively. The matrix size was 128×92 pixels and the receiver bandwidth was 735 Hz/pixel. T_R was fixed to 2500 ms and 2 averages were acquired for each TE to increase the SNR.

For quantification of the T_2 relaxation times, the ROIs from the T_1 quantification were used and corrected manually on the image with the lowest T_E if necessary. T_2 was quantified by fitting the mean signal values for varying T_E s to a monoexponential decay model [53]. In vCFs, T_2 relaxation times of the fat component could not be determined as the water-saturated signal was too low because of a negligible fat fraction. An exemplary fit of the model to the signal data in normal-appearing vBM, an iVD and a vCF and the corresponding image with the shortest T_E are shown in Fig. 5.4. In Fig. 5.5 maps of the T_2 acquired pixel-wise are shown for two patients with a benign and a malignant fracture. On these maps only the values in normal-appearing vBM and in vCF are shown. It can be seen as in the case of T_1 that for the malignant vCF the values of $T_{1\text{water}}$ in the vCF are similar to those of $T_{1\text{fat}}$. This is due to the fact that the fat suppression is not perfect and since there is almost no fat in the lesion the signal corresponds to the not-suppressed water signal. In the case of the osteoporotic vCF the determination of $T_{1\text{fat}}$ is also not reliable. The calculated

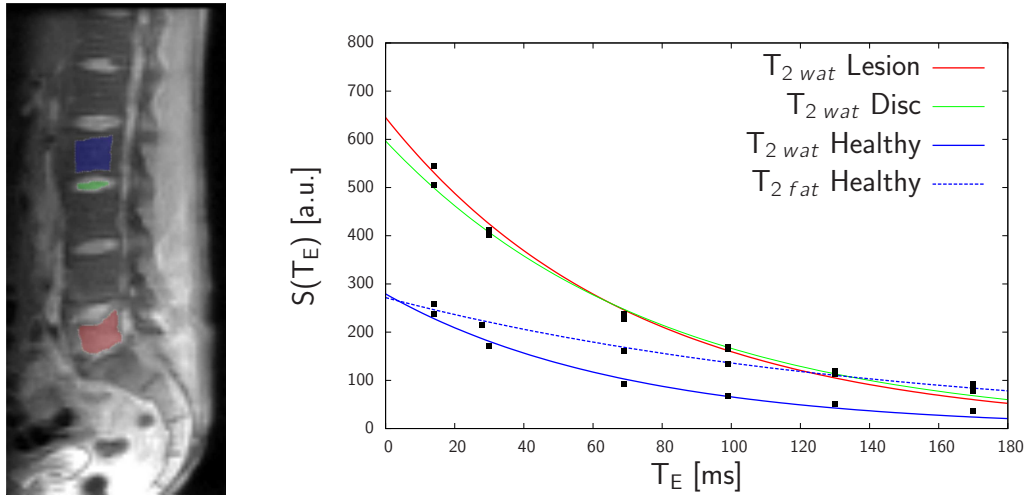


Figure 5.4: Fit of the signal data to a monoexponential decay model for a patient with a malignant lesion in L5. Shown are the fit for the water component in the lesion and the intervertebral disc between L3 and L4 and for the water and fat component in normal-appearing vBM in L2. The reference image corresponds to the fat-saturated image with $T_E = 14$ ms.

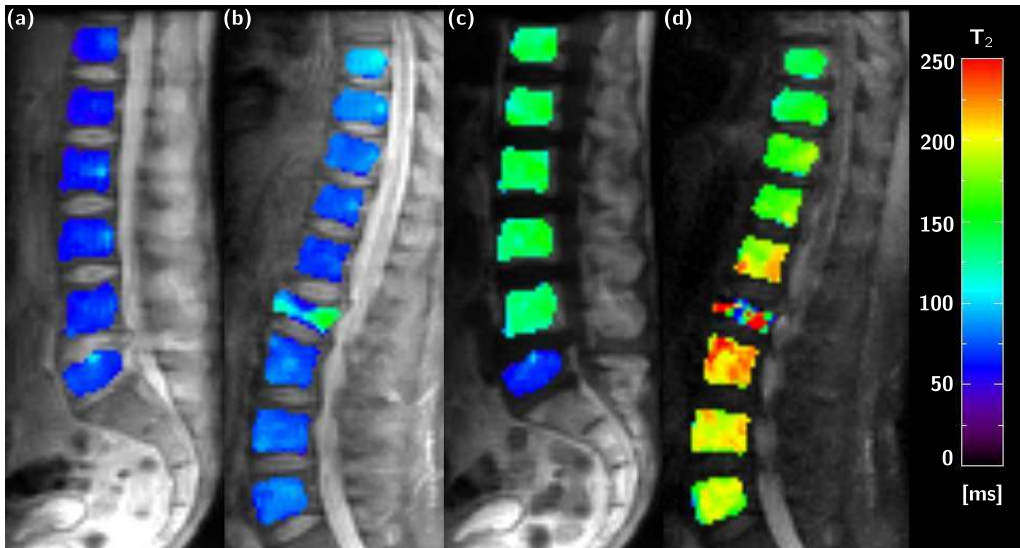


Figure 5.5: T_2 -map of the water component in a patient with (a) a vCF in L5 caused by malignant infiltration and (b) a vCF in L1 caused by osteoporosis. In (c) and (d), the maps of T_{fat} in the corresponding patients are shown.

values correspond to a mixture of the very small fat and non-suppressed water signal.

The mean values and standard deviations of the T_2 -values in normal-appearing vBM, iVDs and in vCFs are summarized in Table 5.2. Furthermore, box-plots of the measured T_2 -values in fat and water are shown in Fig. 5.6. The T_2 -values of the

water component were found to be significantly longer in vCFs compared to normal-appearing vBM (malignant: 120 vs. 82 ms, osteoporotic: 108 vs. 86 ms). The T_2 of the iVDs was significantly smaller than in the vCFs. The T_2 in the iVDs of patients with osteoporosis was decreased compared to patients with a malignant infiltration but not significantly. T_2 of water in vBM has previously been measured only by Träber et al. [134]. Our values of 82 ms in normal-appearing vBM of patients with osteoporosis and 86 ms in patients with malignant lesions are about 30 % higher. T_2 of fat in vBM was determined by Gold et al. [135] as 166 ms agreeing well with our values in normal-appearing vBM of 172 ms in patients with osteoporosis and 149 ms in patients with malignant lesions. The values reported by Träber et al. of about 70 ms are 50 % smaller than our results. Interestingly, the T_2 values of fat measured by Gold et al. agree, while the T_1 values of fat disagree with our results, although the same technique of fat suppression was applied in both cases. In malignant lesions, an increase of 16 % of T_2 was found compared with normal-appearing vBM. These differences were not significant, contrary to the findings of Träber et al. reporting a significant difference ($p < 0.002$). T_2 in osteoporotic fractures has not been determined before. A significant increase of 39 % was found, possibly due to a reduction of local magnetic field gradients caused by the destruction of the trabecular structure.

Pathology	Osteoporosis ($n = 20$)		
Region	vBM	iVD	vCF
T_{2wat} [ms]	82 (15)	65 (14)	120 (27)
T_{2fat} [ms]	172 (14)	–	–

Pathology	Malignant ($n = 20$)		
Region	vBM	iVD	vCF
T_{2wat} [ms]	86 (16)	78 (26)	108 (25)
T_{2fat} [ms]	148 (20)	–	–

Table 5.2: Summary of the mean values and standard deviations (shown in parentheses) of T_{2wat} and T_{2fat} .

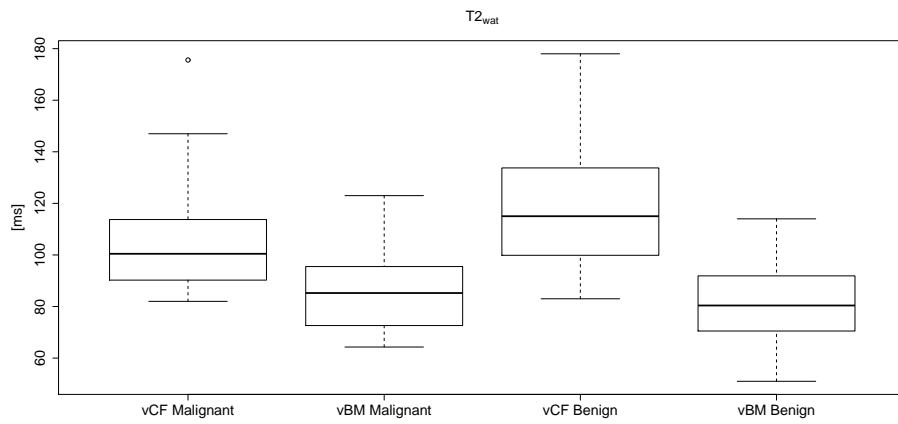
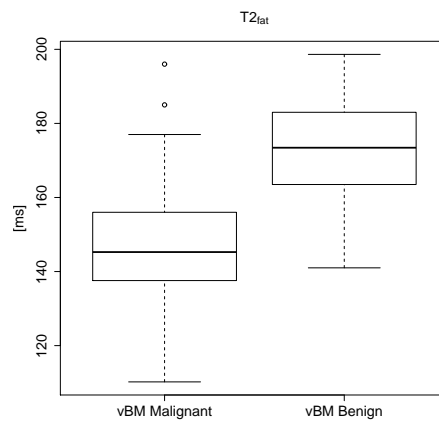
(a) T_{2wat} (b) T_{2fat}

Figure 5.6: Box-plots of (a) T_{2wat} values in normal-appearing vBM and vCFs and of (b) T_{2fat} values in normal-appearing vBM.

5.5 T_2^* Quantification

The signal of the DW-PSIF sequence that we have analyzed so far refers to a (hypothetical) signal acquisition exactly at the application of the RF pulse. However, for the measurements the T_E of the DW-PSIF, corresponding to the time span between the acquisition of the k-space center and the center of the subsequent RF pulse, was set to 7.17 ms. Therefore, an additional attenuation of the signal caused by the T_2^* -decay occurs. The signal function of the PSIF signal supplemented by the T_2^* effects is given by

$$S_{PSIF}^* = S_{PSIF} \cdot \exp(-T_E/T_2^*). \quad (5.1)$$

T_2^* is also called the apparent or effective transverse relaxation time. It takes into account that the signal-formation in gradient-echo imaging depends not only on the natural microscopic transverse relaxation T_2 , but is also effected by an additional dephasing arising from an inhomogeneous static magnetic field. These inhomogeneities arise from magnet imperfections and local magnetic susceptibility variations within an imaged object. Usually the parameter T_2' is used to account for the signal relaxation due to the imperfections. The effective transverse relaxation time is then given by

$$\frac{1}{T_2^*} = \frac{1}{T_2} + \frac{1}{T_2'}, \quad (5.2)$$

where T_2' is inversely proportional to the magnetic field inhomogeneity ΔB in each imaging voxel, that is, $T_2' \sim 1/(\gamma\Delta B)$. Whereas T_2 is an intrinsic property of the tissue, T_2' and T_2^* depend not only on external factors (e.g., susceptibility variations within the patient and how well the magnet is shimmed), but also on the prescribed imaging voxel size.

In vertebral bodies, the difference in magnetic susceptibility between trabecular bone and vBM has been shown to affect the appearance of vBM. The magnetic field inhomogeneities found in vBM depend on the density of the trabecular network, as was first shown by Davis et al. [138]. In general, they cause a strong reduction of the T_2^* of vBM. This measurements were confirmed by studies of Majumdar et al. [139] and Wehrli et al. [30], who found a correlation between the decrease of bone mineral density and the increase of T_2^* in patients with osteoporosis. In vCF, the trabeculae are either replaced by cancerous tissue in the case of a malignant infiltration or by yellow marrow in the case of osteoporosis. It is therefore suspected that the T_2^* in a vCF is increased compared to normal vBM. Hence, the signal contrast of the DW-PSIF sequence between vCFs and vBM depends on their T_2^* -values, which have to

be determined separately.

For the determination of the T_2^* a multi-echo GRE sequence was used. Echoes were acquired at $T_E = 3.6, 10, 15, 20, 25$ and 30 ms. The sequence parameters were set to $T_R = 197$ ms, FOV 300×225 mm², slice thickness 5 mm, receiver bandwidth 260 Hz/pixel, flip angle 25° and a matrix size of 128×96 .

The T_2^* values were calculated on a ROI-basis. The ROIs used for the quantification of the other parameters were used and corrected manually if necessary. The signal intensities were fitted to a monoexponential decay model as a function of the varying T_E , as in the case of T_2 in section 5.4. The mean values and standard deviations are summarized in Table 5.3. The values in the vCFs were significantly increased compared to normal-appearing vBM (malignant: 22 vs. 8 ms, osteoporotic: 14 vs. 8 ms). The values in osteoporotic and malignant lesions deviated significantly ($p = 0.006$). In the case of normal-appearing vBM, in many patients the applied measurement technique did not provide images of a sufficient image quality for a robust determination of the T_2^* values. Since our 2 shortest T_E s for the T_2^* quantification were 3.6 and 10 ms, for typical values of T_2^* in vBM, already for the second measurement noise became a severe problem. It has been shown in the literature [30], that the values of T_2^* of water and fat in vBM should be more or less equal if they are homogeneously distributed.

Pathology	Osteoporosis ($n = 20$)		
Region	vBM	iVD	vCF
$T_{2_{wat}}^*$ [ms]	8 (3)	42 (20)	14 (6)
$T_{2_{fat}}^*$ [ms]	11 (3)	–	–

Pathology	Malignant ($n = 20$)		
Region	vBM	iVD	vCF
$T_{2_{wat}}^*$ [ms]	8 (4)	36 (16)	22 (10)
$T_{2_{fat}}^*$ [ms]	9 (3)	–	–

Table 5.3: Summary of the mean values and standard deviations (shown in parentheses) of $T_{2_{wat}}^*$ and $T_{2_{fat}}^*$.

5.6 ADC Quantification

In the case of the ADC we only determined the value of the water component. As discussed in section 3.3.3, results of previous studies suggest that the ADC of protons in fat is close to 0. These findings were also confirmed by diffusion-weighted measurements performed in vertebrae of healthy volunteers. Using the diffusion-weighted sequence that will be described below in combination with a water saturation pulse no significant decrease of the signal intensity at increasing diffusion weighting was found, see Fig. 5.7.a. Hence, for the following analysis, the ADC_{fat} will always be set to 0.

For the determination of the ADC_{wat} , a fat-saturated diffusion-weighted single-shot turbo-spin-echo (DW-ssTSE) sequence with 4 b-values ($b=100, 250, 400, 600$ s/mm²) was applied. The imaging parameters were a 128×92 matrix, $TE = 72$ ms, $TR = 3000$ ms, a flip angle of 180° for the refocusing pulses and a receiver bandwidth of 735 Hz/pixel. In order to obtain the maximum diffusion weighting per T_E , it was applied in diagonal direction (diffusion gradients were applied simultaneously in all 3 physical directions). Due to the low signal of the bone-marrow in DWI, ten averages were taken in order to improve the signal-to-noise ratio (SNR). The process of averaging was performed on magnitude data to avoid image artifacts due to motion-induced phase variations. The total acquisition time was 2:13 min.

ADCs were quantified on a ROI basis. The ROIs used for the quantification of the relaxation times were adopted and if necessary adjusted on the image with the lowest diffusion weighting, which provided the best image quality. The location of all ROIs was verified on the anatomical images. To determine the ADC, the mean signal intensity curves (as a function of the varying b -value) within the ROIs were fitted to an exponential decay model with a least-squares method [51]. An exemplary fit of the model to data in normal-appearing vBM, an iVD and in a vCF, and the corresponding image with the lowest diffusion-weighting are shown in Fig. 5.8. In Fig. 5.9, maps of the ADC acquired pixel-wise are shown for two patients with a benign and a malignant fracture. The mean values and standard deviations of the ADCs in normal-appearing vBM and in vCFs are summarized in Table 5.4. Box-plots of the measured ADCs are shown in Fig. 5.10. Typical values in normal appearing vBM were found to be 0.58×10^{-3} mm²/s in both patient groups. The ADCs in the lesions deviated significantly from normal-appearing vBM and between both patient groups (malignant: 1.36×10^{-3} mm²/s, osteoporotic 1.77×10^{-3} mm²/s). The ADCs measured in the iVDs were significantly higher than in normal-appearing vBM and almost equal in both patient groups (malignant: 1.84×10^{-3} mm²/s, osteoporotic: 1.76×10^{-3} mm²/s).

The values agree with the results reported in the literature [93, 140].

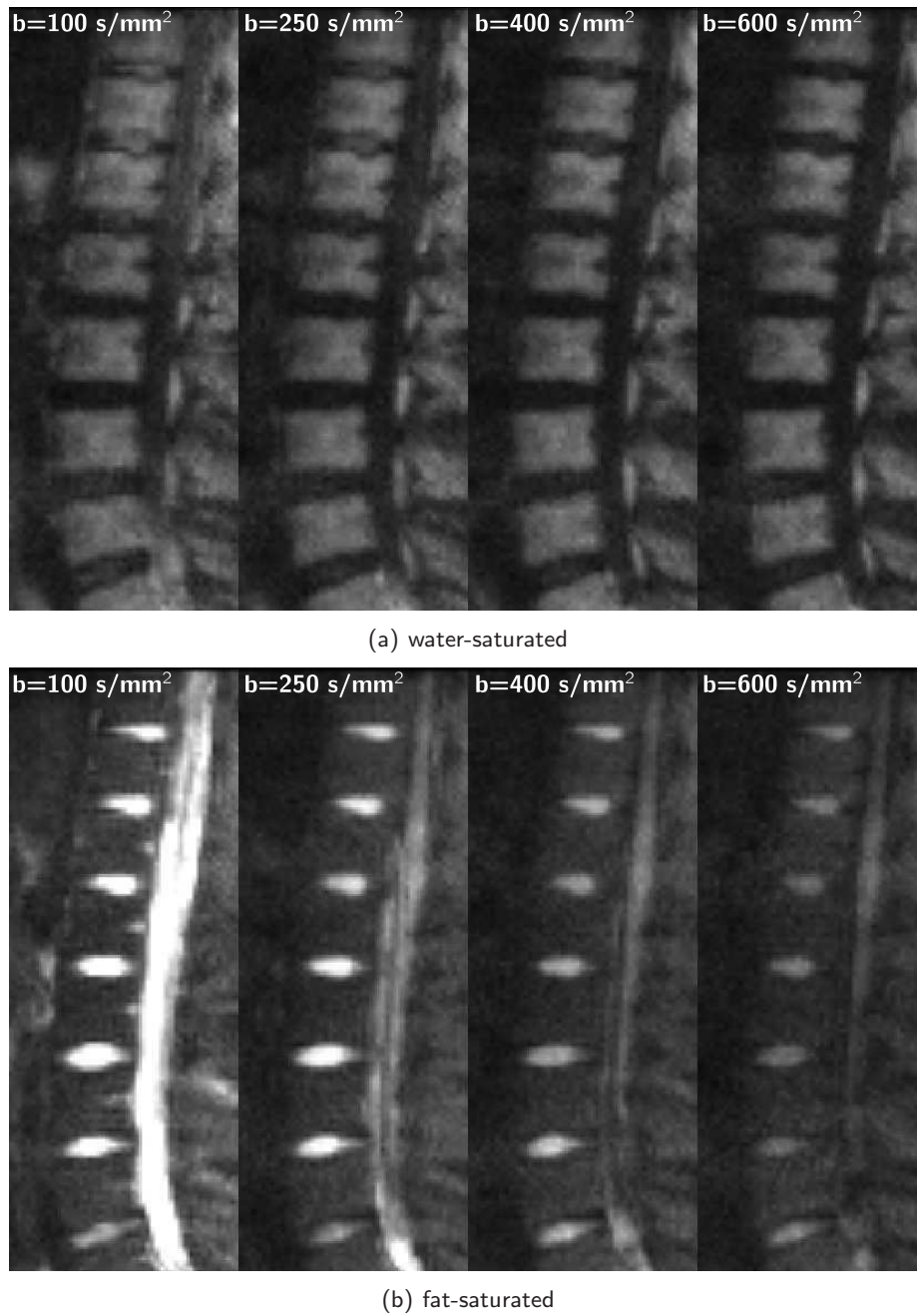


Figure 5.7: Diffusion-weighted images of a sagittal slice of the vertebral column of a healthy volunteer acquired with (a) a water-saturated and (b) a fat-saturated DW-ssTSE sequence. The diffusion weighting was increased from $b = 100$ to 600 s/mm^2 from left to the right.

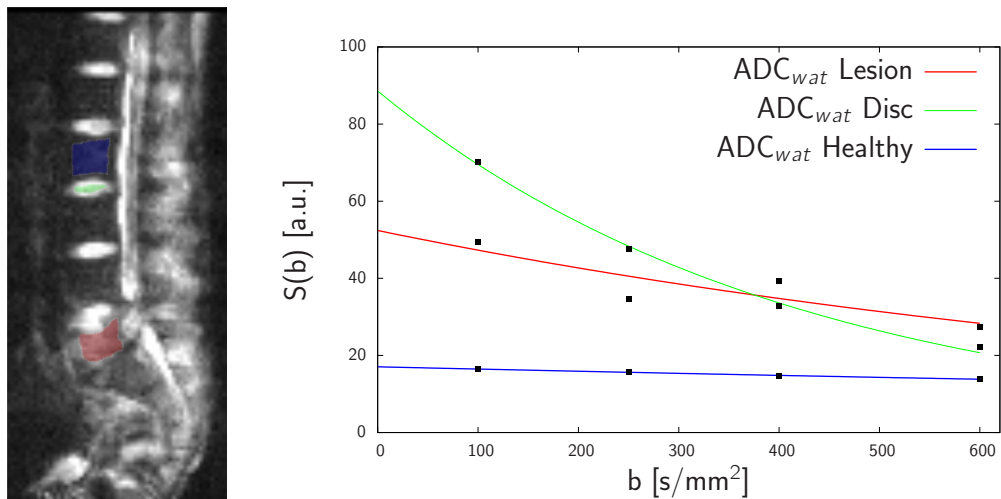


Figure 5.8: Fit of the signal data to the monoexponential decay model as a function of the b -value for a DW-ssTSE sequence acquired in a patient with a malignant lesion in L5. Shown are the fit for the lesion and normal-appearing vBM in L2. The reference image corresponds to $b = 100 \text{ s/mm}^2$.

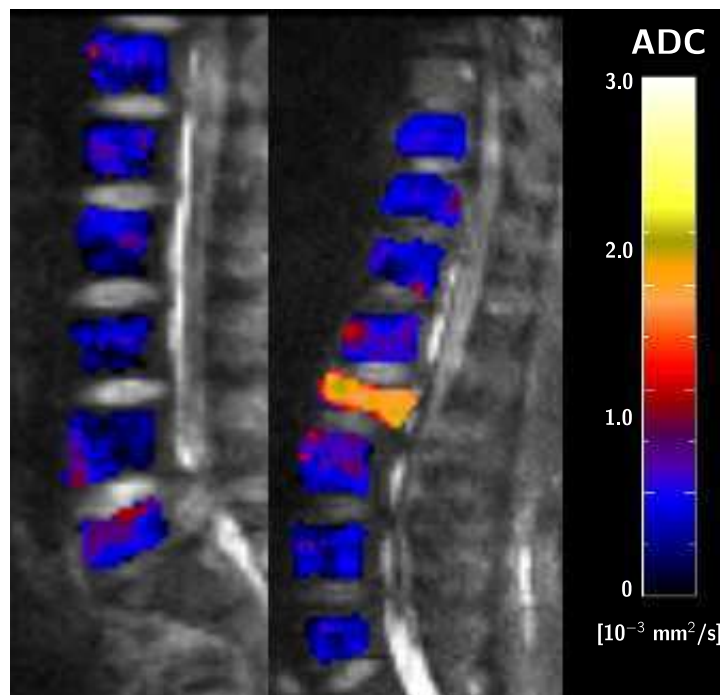


Figure 5.9: ADC-map of a patient with a vCF in L5 caused by malignant infiltration (left side) and a vCF in L1 caused by osteoporosis (right side).

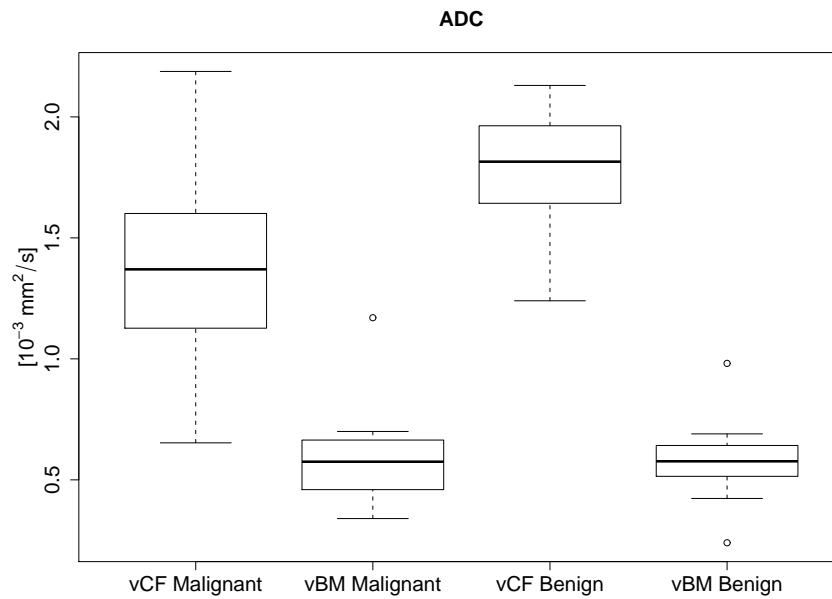


Figure 5.10: Box-plots of ADC_{wat} in normal-appearing vBM and vCFs.

Pathology	Osteoporosis ($n = 20$)			Malignant ($n = 20$)		
	vBM	iVD	vCF	vBM	iVD	vCF
Mean value [$10^{-3} \text{ mm}^2/\text{s}$]	0.58	1.76	1.77	0.58	1.84	1.36
Std Dev [$10^{-3} \text{ mm}^2/\text{s}$]	0.14	0.36	0.26	0.18	0.27	0.39

Table 5.4: Summary of the mean values and standard deviations of ADC_{wat} .

5.7 Fat and Water Quantification

As mentioned in section 2.2, vBM, in contrast to most other tissues, contains large fractions of fat. The distribution pattern depends on various parameters like age and sex. Furthermore, pathologies like osteoporosis or malignant infiltration are known to either change the composition of vBM or to replace vBM, thereby modifying the distribution pattern of fat and water. Since the physical properties of protons in fat and water are different, it is essential to know the exact ratios of fat, f_{fat} , and water, f_{wat} , to understand the MR signal of vBM.

Most techniques applied to separate the fat and water component rely on the chemical-shift between the fat and water component. Even in a perfectly homogeneous external field, local fields vary at the molecular level. The protons in water see a different field from those in a lipid-based or fatty compound. The precession frequency of the fat protons is shifted to a lower frequency compared to the water protons. The difference between the frequencies is given by

$$\Delta f_{fw} \equiv f_f - f_w = \sigma_{fw} \gamma B_0 / (2\pi), \quad (5.3)$$

where σ_{fw} is the chemical shift between fat and water. Most fat in the human body has $\sigma_{fw} = 3.35$ ppm, corresponding to a frequency shift of 214 Hz at 1.5 T. If the frequency spread per voxel is less or not much greater than Δf_{fw} , the chemical shift can lead to a misregistration of the fat component in the frequency-encoding direction. The frequency shift is also used in most fat-saturation techniques. Either the fat component is saturated prior to the image acquisition using a sufficiently narrow-band RF saturation pulse that only effects the fat component, or an excitation pulse that only acts on the water component is used. A third way to suppress the fat component is the so-called Dixon method [141] that additionally allows for the quantification of the fat and water ratios. In contrast to the other fat suppression techniques, the separation is achieved through postprocessing. If we assume that fat and water are the only two signal-contributing chemical species in the object to be imaged, the complex image acquired with a GRE sequence is a function of T_E

$$\hat{S}(T_E) = \hat{S}_{wat}(T_E) + \hat{S}_{fat}(T_E), \quad (5.4)$$

where \hat{S} refers to the complex signal, $\hat{S} = S_0 \exp(i\phi)$. S_0 is the signal amplitude of the GRE sequence. After the application of the RF pulse, the fat component acquires an additional phase relative to the water component due to the chemical shift. At

the time of the image acquisition T_E the phase difference is given by

$$\phi_w(T_E) - \phi_f(T_E) = \Delta\omega_{fw}T_E, \quad (5.5)$$

where ϕ_w and ϕ_f are the phases of both components and $\Delta\omega_{fw} = 2\pi\Delta f_{fw}$. The complex signal can then be written as

$$\hat{S}(T_E) = |\hat{S}_w| + |\hat{S}_f| \cdot e^{-i\Delta\omega_{fw}T_E}. \quad (5.6)$$

The acquisition of images at different values of T_E permits the separation of water and fat based on the phase information. Two limiting cases can be distinguished with respect to the phase difference: the situation when water and fat spins are in opposed phase

$$\Delta\omega_{fw}T_E = (2n+1)\pi \quad \rightarrow \quad |\hat{S}_{opp}| = |S_{w0} - S_{f0}| \quad (5.7)$$

or in phase

$$\Delta\omega_{fw}T_E = (2n)\pi \quad \rightarrow \quad |\hat{S}_{in}| = |S_{w0} + S_{f0}|, \quad (5.8)$$

where n is an integer and S_{w0} and S_{f0} are the amplitudes of the water and fat signal, respectively. In the in-phase case, the amplitudes of both components add up, while they cancel in the opposed-phase case. At a field strength of 1.5T, the opposed-phase image can be acquired setting $T_E = (2n+1) \cdot 2.38$ ms and an in-phase image setting $T_E = n \cdot 4.76$ ms, for $n \in \mathbb{N}_0$. In Fig. 5.11, images of the spine acquired at the opposed- and in-phase situation are shown for a FLASH sequence. While the signal of the water-dominated intervertebral discs remains unchanged, the opposed-phase signal in the vertebrae is strongly decreased compared to the in-phase images. Therefore, for an understanding of the signal of the DW-PSIF, it is essential to take in to account at which T_E the signal was acquired.



Figure 5.11: Images of the spine acquired with a FLASH sequence at $T_E = 2.38$ (opposed-phase) and 4.76 ms (in-phase) of a patient with an osteoporotic vCF in L5.

Previous studies have applied chemical-shift imaging to differentiate benign from malignant lesions based on the signal ratio of in- and opposed-phase images (Oppln-ratio) [142, 143, 144]. In general, it was found that the Oppln-ratio was significantly increased in malignant compared to benign vCFs. In the case of a vCF caused by malignant infiltration, vBM is replaced by cancerous tissue and the lesion is expected to contain almost no fat. In the case of osteoporosis, the trabeculae in the vertebra are replaced by fatty tissue, and therefore also in a fractured vertebra some fat is expected to remain in the lesion. This difference could potentially be visualized and quantified based on the Oppln-ratio. In Fig. 5.12, maps of the Oppln-Ratio of patients with a benign and a malignant vCF are shown.

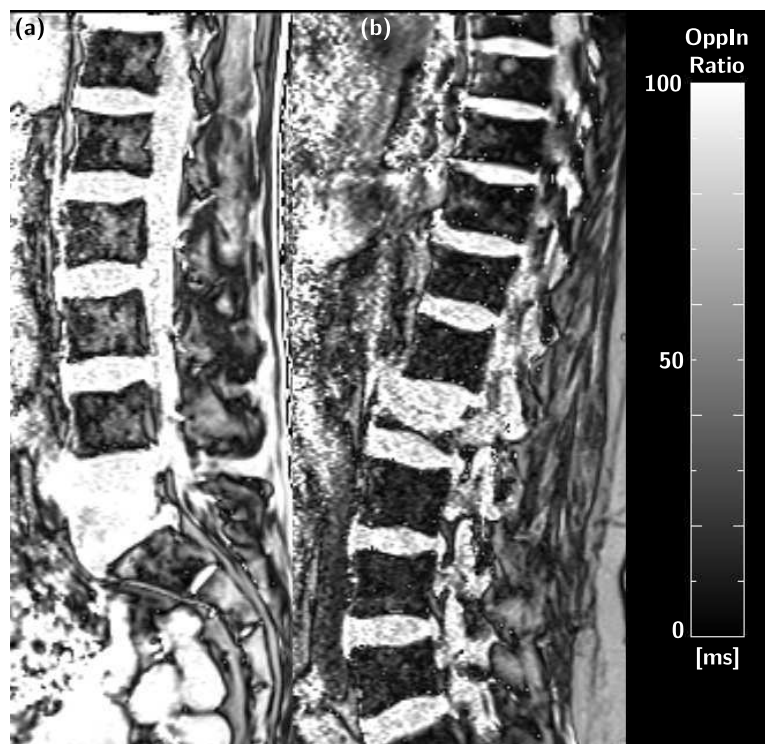


Figure 5.12: Maps of the Oppln-ratio of the spine determined with a FLASH sequence at $T_E = 2.38$ (opposed-phase) and 4.76 ms (in-phase) of (a) a patient with a malignant vCF in L5 and (b) a patient with a benign vCF in L1. The ROI values in the malignant vCF were 99% and 91% in the osteoporotic vCF.

However, these methods are suffering from a potential ambiguity, because only the dominant component can be determined. It remains unclear whether water or fat is dominating. Calculating the sum and the difference of the in- and opposed-phase

signal we get:

$$S_{sum} \equiv |S_{in}| + |S_{opp}| \quad (5.9)$$

$$S_{diff} \equiv |S_{in}| - |S_{opp}|. \quad (5.10)$$

While $S_{in} = S_{w0} + S_{f0}$, the second term depends on whether water or fat is the dominant component

$$|S_{opp}| = \begin{cases} S_{w0} - S_{f0} & \text{if } S_{w0} > S_{f0} \\ S_{f0} - S_{w0} & \text{if } S_{f0} > S_{w0} \end{cases}. \quad (5.11)$$

Hence, $S_{sum}/2$ can either correspond to the magnitude of the water or the fat signal. However, this analysis only uses one half of the information of the signal data, the magnitude of the signals. In order to obtain an unambiguous separation, the phase information has to be taken into account. The phase map of the opposed-phase image encodes the information whether the fat or water component is dominating. In order to determine the fat and water ratios for the evaluation of the DW-PSIF, an extended two-point Dixon method, using the phase information of the opposed-phase image, was applied in the present study [145, 146].

Opposed- and in-phase images were acquired with a FLASH sequence ($T_{Eopp} = 2.38\text{ms}$, $T_{Ein} = 4.76\text{ms}$, FOV $300 \times 225 \text{ mm}^2$, slice thickness 5 mm, matrix size 320×240). The ROIs used for the quantification of the relaxation times were used and if necessary adjusted on the opposed-phase image, providing the best separation between the intervertebral discs and vBM. In Fig. 5.13, exemplary images of the phase and magnitude images are shown.

In general, the signal in Eq. (5.4) has to be corrected for phase errors caused by field inhomogeneities or a global phase shift. Otherwise, these errors may lead to a reversal of the water/fat roles. Assuming that both water and fat are reconstructed within a voxel and experience the same global phase shift ϕ_0 and static field inhomogeneity ΔB , the signal is given by

$$\hat{S}(T_E) = [S_{w0} + S_{f0} \cdot e^{-i\Delta\omega_{fw}T_E}] \exp(-i\gamma\Delta BT_E - i\phi_0). \quad (5.12)$$

Hence, the signals of the opposed- and in in-phase images are then defined as

$$\hat{S}_{opp} = (S_{w0} - S_{f0}) \exp[-i(\phi_0 + \phi)] \quad (5.13)$$

$$\hat{S}_{in} = (S_{w0} + S_{f0}) \exp[-i(\phi_0 + 2\phi)], \quad (5.14)$$

where we have defined $\phi = i\gamma\Delta BT_{E_{opp}}$ and $T_{E_{in}} = 2T_{E_{opp}}$. In total, the in- and opposed-phase signals depend on four scalars. Hence, the acquisition of the magnitude- and phase-images should be sufficient to determine the unknown quantities. A unique solution for the unknown quantities is not immediate because some of the unknown terms occur in complex exponential factors and therefore are periodic. It is possible to determine an expression relating the data and the inhomogeneity phase shift ϕ as follows

$$\text{Arg} \left[\left(\bar{\hat{S}}_{opp} \cdot \hat{S}_{in} \right)^2 \right] = -2\phi \bmod 2\pi. \quad (5.15)$$

In general, ϕ is not restricted to an interval of length 2π . Therefore, a phase unwrapping has to be performed to correct for phase jumps before ϕ can be calculated from 2ϕ . In this study, the phase unwrapping was performed using a region-growing algorithm following Szumowski et al. [147], which is described briefly in Fig. 5.14. An exemplary image of 2ϕ before and after the phase wrapping is shown in Fig. 5.15.



(a) Opposed-phase



(b) In-Phase

Figure 5.13: (a) Opposed-phase and (b) in-phase images of the spine of a patient with a malignant vCF in L3. Shown are (i) the magnitude and (ii) the phase images.

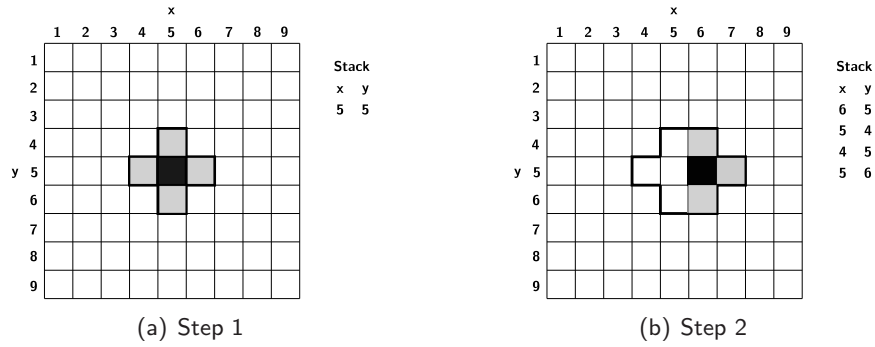


Figure 5.14: The black box refers to the current seed pixel, the shaded boxes to the neighbors checked in this iteration, and the white boxes surrounded by the thick black borders to the pixels included in the unwrapped region. At (a) the region growing starts with a single seed pixel. At each step of the iteration process, the four neighboring pixels, not included in the region, are checked. A preselected value of the phase difference $\Delta\psi$ between pixels is used as the criterion for adding a pixel to the region. If a pixel fulfills the criterion it is added to the region and to the stack, and will be used as a new seed later on as in (b). Otherwise 2π is added or subtracted from the pixel phase and the phase difference is checked again. If its value is still above $\Delta\Psi$ it will retain its original phase and will not be added to the stack; if it is less than $\Delta\Psi$ it keeps the new phase and is added to the stack. This process continues until no new seed pixels remain on the stack [147].

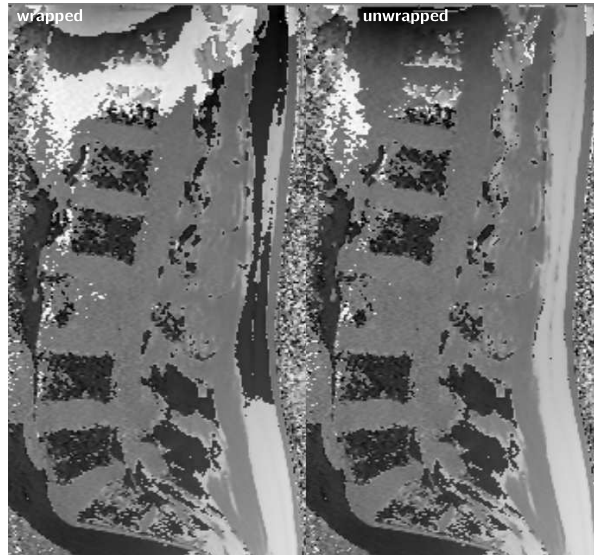


Figure 5.15: Images of 2ϕ , Eq. (5.15), before and after the phase unwrapping.

After the phase unwrapping has been performed, ϕ can be calculated, dividing the preceding result, Eq. (5.15), by 2. The in-phase images can now be corrected for the inhomogeneity induced phase errors

$$\hat{S}'_{in} = \hat{S}_{in} \cdot \exp(i\phi) \quad (5.16)$$

and the fat and water images can then be calculated as the magnitudes of

$$\hat{S}_W = \frac{1}{2} [\hat{S}'_{in} + \hat{S}_{opp}] \quad (5.17)$$

$$\hat{S}_F = \frac{1}{2} [\hat{S}'_{in} - \hat{S}_{opp}] \quad (5.18)$$

Finally, we calculated the fat and water ratios

$$f_{wat} = \frac{|\hat{S}_W|}{|\hat{S}_W| + |\hat{S}_F|} \quad \text{and} \quad f_{fat} = \frac{|\hat{S}_F|}{|\hat{S}_W| + |\hat{S}_F|}. \quad (5.19)$$

Exemplary images of f_{wat} and f_{fat} are shown in Fig. 5.16. Based on these values of the ratios the signal of the DW-PSIF of both components can be calculated separately and is afterwards combined to the vBM signal given by

$$S_{vBM} = f_{wat}S_{wat} + f_{fat}S_{fat} = f_{wat}S_{wat} + (1 - f_{wat})S_{fat}. \quad (5.20)$$

In the last step, we used $f_{wat} + f_{fat} = 1$ and we will only refer to f_{wat} in the following analysis. The mean values and the standard deviations of f_{wat} are summarized in Table 5.5. Values for f_{wat} in the iVDs were not determined, since no measurable amount of fat resides there. Furthermore a box-plot of the measured f_{wat} in normal-appearing vBM as well as in vCFs is shown in Fig. 5.17. We found that the fat content in the vCFs was significantly decreased compared to normal-appearing vBM (malignant: 96 vs. 57 %, osteoporotic: 88 vs. 48 %). The values in normal-appearing vBM and vCFs deviated significantly between both patient groups. The decrease of f_{wat} in normal-appearing vBM of patients with osteoporosis agrees with the results of Griffith et al. and Schellinger et al. [148, 149, 150], who found a significant correlation between the decrease of the bone mineral density and the increase of the fat content in patients with osteoporosis. In general, the fat content shows strong changes with age and also depends on the sex of the patients [151].

Pathology	Osteoporosis		Malignant	
Region	vBM	vCF	vBM	vCF
Mean value [%]	48	88	57	96
Std. dev. [%]	13	12	16	4

Table 5.5: Summary of the mean values and standard deviations of f_{wat} .

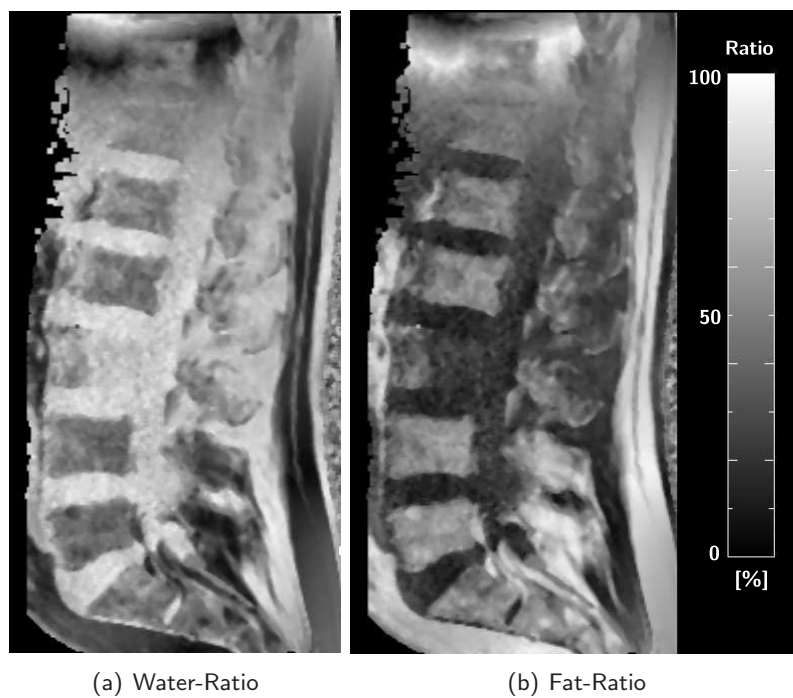


Figure 5.16: Maps of the (a) water- and (b) fat-ratio determined with the phase-corrected two-point Dixon method in a patient with a malignant vCF in L3. Values are given in percent.

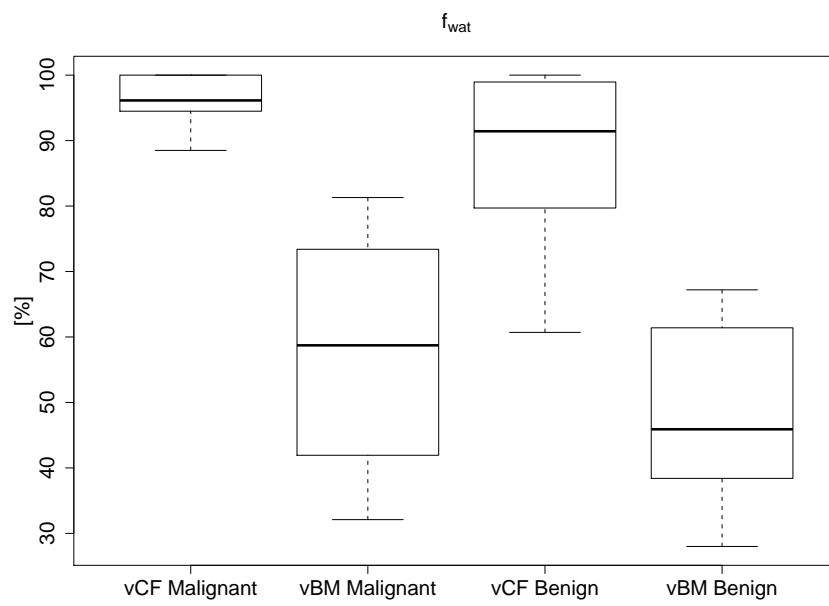


Figure 5.17: Box-plots of f_{wat} values in normal-appearing vBM and vCFs.

5.8 Signal Simulations

In section 4.4, we derived the signal of the DW-PSIF sequence for a single tissue. In this section, we want to investigate the sensitivity of the signal to changes of the different parameters that enter the signal function. In Fig. 4.9, we already showed that the signal for a fixed δ is decreasing with increasing T_1 . The strength of the decrease is inversely proportional to δ . In the case of T_2 , the signal increases with increasing T_2 . As for T_1 , the strength of the increase is inversely proportional to δ . As expected, the signal as a function of the ADC is decreasing with increasing δ .

In vBM, the situation is more complicated. First, the signal is a combined function of the signals of fat and water. Second, as shown in the section 5.7, the relative phase between the fat and water component determined by T_E plays an important role for the signal characteristics. Furthermore, with increasing T_E the T_2^* -weighting leads to a different signal attenuation of vCFs and normal appearing vBM. The combined signal is given by

$$S_{vBM} = [f_{wat} S_{wat} \exp(-T_E/T_{2wat}^*) + (1 - f_{wat}) S_{fat} \exp(-i\Delta\omega_{fw} T_E) \exp(-T_E/T_{2fat}^*)], \quad (5.21)$$

where S refers to the signal of the DW-PSIF sequence, Eq. (4.91). In Fig. 5.18, simulations of the signal as a function of T_E and f_{wat} are shown.

It can be seen that there is a strong dependence on f_{wat} . The signal amplitude of the water component for $\delta = 3$ ms is only about 50 % of the fat signal. For equal signal amplitudes, the signal would drop to 0 for a f_{wat} of 50 % and $T_E = 7.17$ ms, see Fig. 5.18.a. In vBM, due to the different signal amplitudes, the signals cancel each other for an f_{wat} of ≈ 71 %. Unfortunately, apart of Byun et al. [97] who measured at $T_E = 5$ ms corresponding more or less to the in-phase situation, there is no information provided with regard to the T_E in the literature [19, 13, 152, 85]. Even in the case of Byun the information about T_E remains unclear, since the authors also report a duration of the diffusion gradient of 5 ms and probably confused δ and T_E . As we will demonstrate in the following, this is, however, a critical parameter for a potential contrast between vCFs and normal-appearing vBM. Different choices of T_E might partially be responsible for the contradictory results reported in the literature with regard to the differentiation of benign and malignant lesions, see section 3.3.3. In the following simulations and for the measurements, T_E was set to 7.17 ms, since previous studies [18, 87, 12] have shown that this value provides an excellent differentiation between the different types of vCFs.

We showed in section 5.7 that the fat component is very small in the vCFs. How-

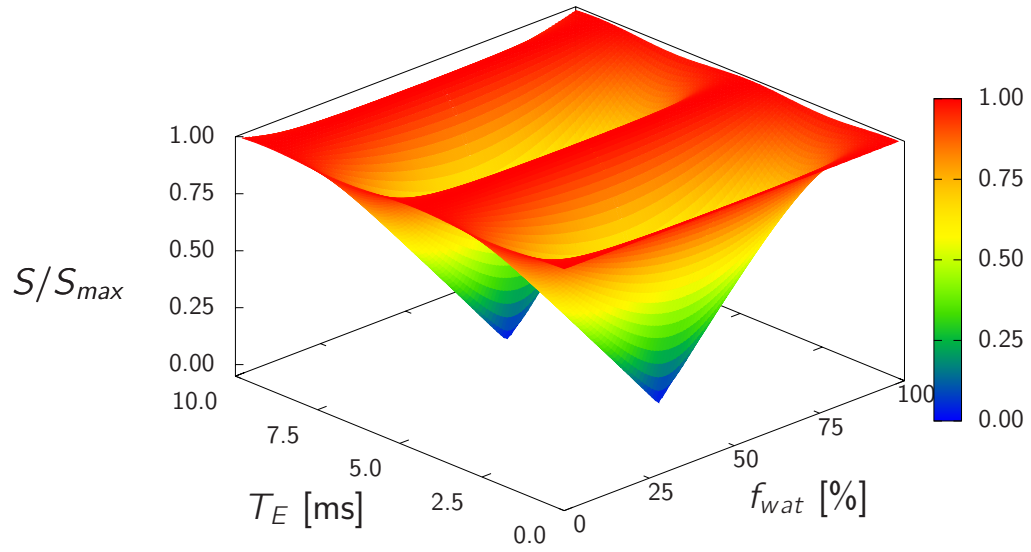
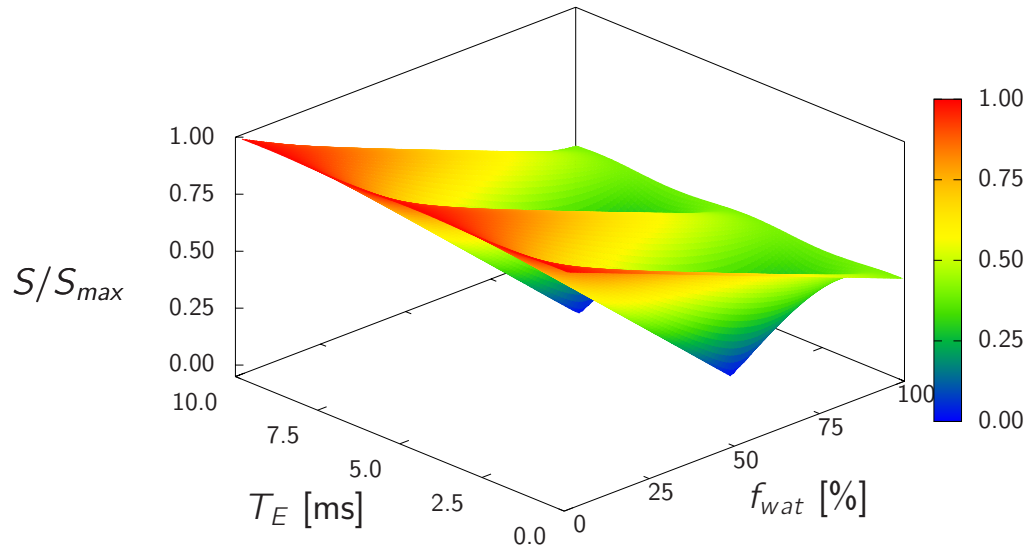
(a) $S_{wat} = S_{fat}$ (b) $S_{wat} \neq S_{fat}$

Figure 5.18: Simulation of the DW-PSIF signal as a function of T_E and f_{wat} . In (a) we assumed that the signal of fat and water are equal, while in (b) we used the parameters derived before for f_{wat} and f_{fat} . The simulated signals correspond to a δ of 3 ms.

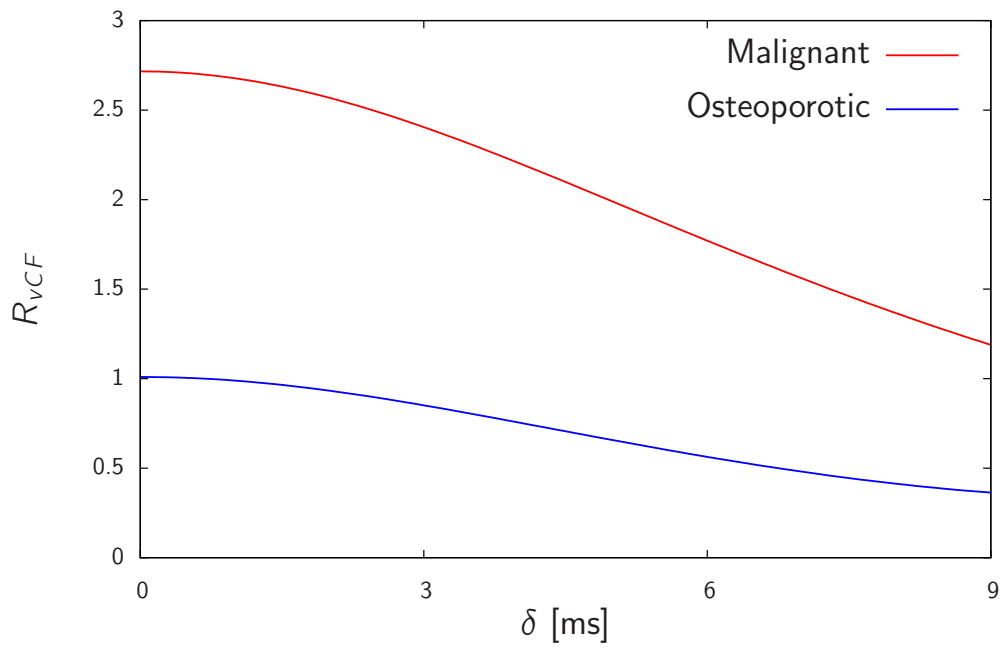
ever, in normal-appearing vBM, the mean values of the water ratio are 48 % in the case of patients with osteoporosis and 57 % in the case of patients with malignant infiltrations. Hence, the fat component is most important for the signal analysis in normal-appearing vBM and effects the characterization of the vCF via the relative contrast between vCF and normal-appearing vBM. Based on the values derived in the previous sections we simulated the signal ratios between vCFs and normal-appearing vBM and compared the signal behavior between the in- and opposed-phase situation. At higher diffusion weightings, the signal is dominated by noise. Therefore, the simulated signal was superimposed by a noise signal. Based on the measurements in healthy volunteers, the amplitude of the noise was defined as 2/3 of the DW-PSIF signal of vBM at the lowest diffusion weighting in the opposed- and 1/2 in the in-phase situation. The simulated signal corresponds to

$$S_{sim} = \sqrt{|S_{vBM}|^2 + |S_{noise}|^2}. \quad (5.22)$$

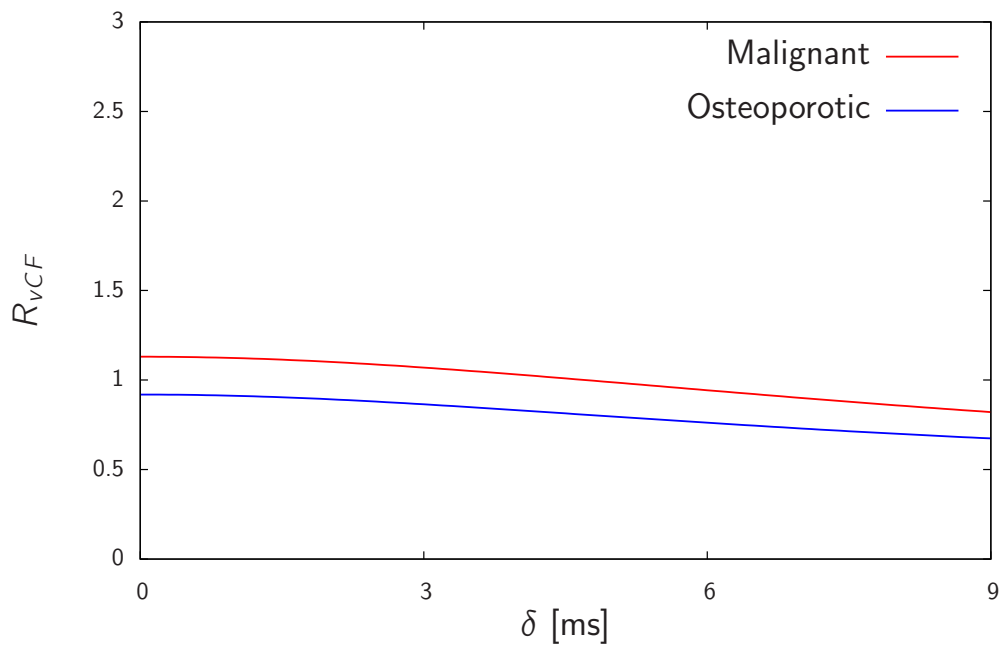
In Fig. 5.19, the simulated evolution of the signal ratios between the signal in the vCF and normal-appearing vBM as a function of δ is shown for the in- and opposed-phase scenario. This ratio is a quantitative measure corresponding to the qualitative assessment of tissue contrast in terms of hyper- (> 1), iso- (≈ 1) and hypo-intensity (< 1). In the following we will refer to this ratio as $R_{vCF} = S_{vCF}/S_{vBM}$. These simulations clearly indicate, that while in the opposed-phase scenario the signal ratio of the malignant vCF is significantly increased compared to that of the osteoporotic vCF, in the case of the in-phase situation almost no difference between both pathologies is present.

In Fig. 5.20 the signal behavior of normal-appearing vBM and the vCF for the parameters in both patient groups are shown. The signal in the iVDs are comparable in both groups. In contrast the signal in normal appearing vBM is increased by a factor of ≈ 2 in the osteoporotic group compared to the malignant group. The signal of the vCFs in the osteoporotic group is $\approx 2/3$ of the signal in the malignant group. These results already indicate that the differences of the R_{vCF} s is not only caused by the different signal characteristics of the vCFs, but also by the normal-appearing vBM. Furthermore the signal contrast is not only caused by the diffusion weighting, since the ADCs in normal appearing vBM were almost equal in both groups. Since the signal of the iVDs in both patient groups is almost equal, it will serve as a normalizing reference for the signals in vBM and vCFs in the following analysis.

These simulations already indicate that f_{wat} is a very important parameter with regard to the signal behavior. Acquiring images in the opposed-phase situation ap-

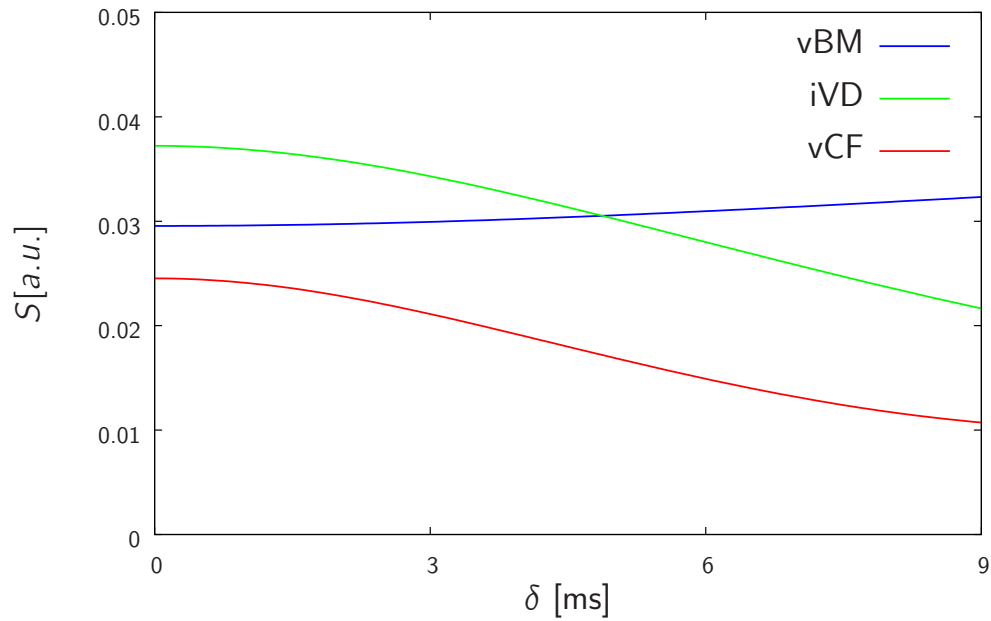


(a) Opposed-Phase

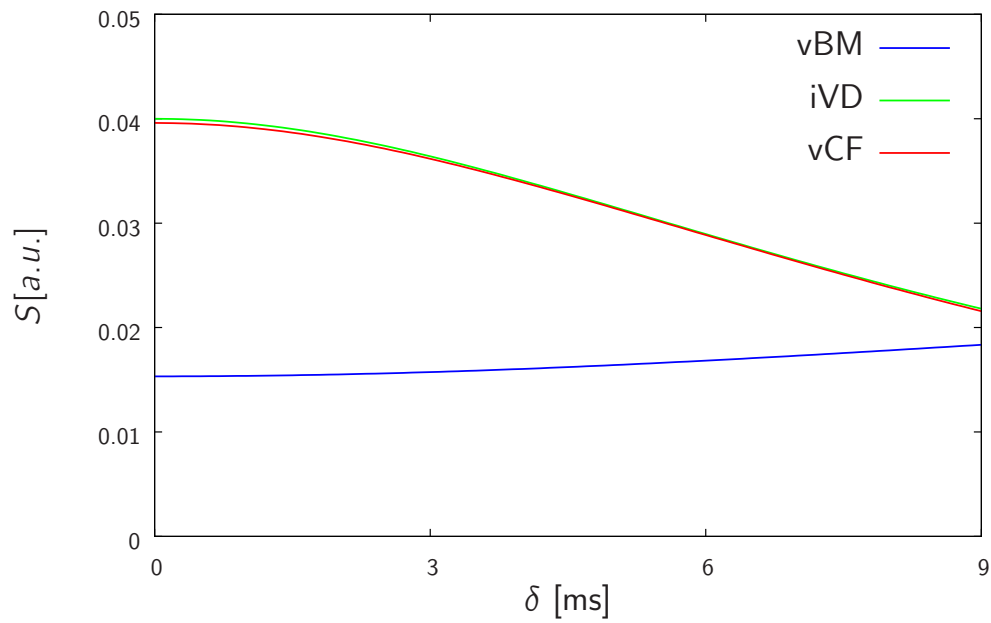


(b) In-Phase

Figure 5.19: Simulation of the ratio between the DW-PSIF signal of a vCF and a normal-appearing vBM, R_{vCF} , as a function of δ . Shown are the scenarios for the (a) opposed-phase and (b) in-phase situation. The parameters for the simulations were set to the values determined in the previous sections.



(a) Osteoporotic vCF



(b) Malignant vCF

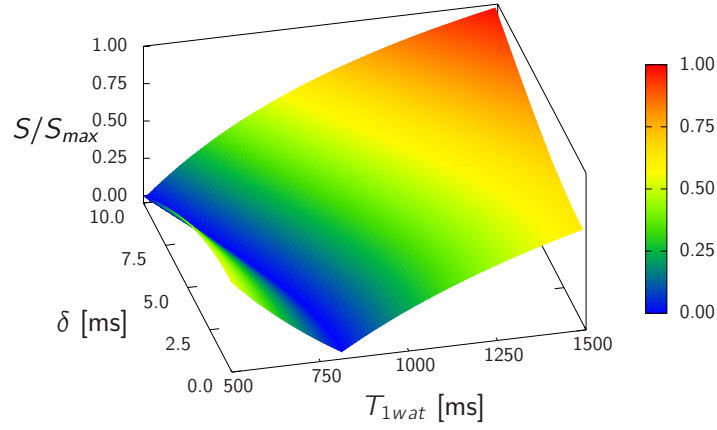
Figure 5.20: Simulation of the DW-PSIF signal in normal-appearing vBM (blue line), intervertebral disc (green line) and vCF (red line) of (a) patients with an osteoporotic vCF and (b) patients with malignant infiltrations.

appears to provide a superior contrast between normal-appearing vBM and vCFs. To identify the parameters that have the greatest influence on the signal of the DW-PSIF sequence in vBM, we performed several simulations varying the various input parameters. First we analyzed the influence of the relaxation times and the ADC_{wat} . The parameters of the fat component were set to $T_{1fat} = 300$ ms, $T_{2fat} = 150$ ms, $ADC_{fat} = 0.0$ and $f_{wat} = 70$ %. In Fig. 5.21.a, the dependence on T_{1wat} is shown, and it can be seen that in contrast to the single-tissue case in Fig. 4.9 the decrease of the signal with increasing T_1 only happens up to a certain value. Above this critical value the fat signal begins to become the dominant component and the signal increases as the signal of the water component decreases. With increasing δ , the water signal is further attenuated and hence the transition point between the water- and fat-dominated regime is shifted to lower values of T_{1wat} . The same effect can be seen in Fig. 5.21.b showing the dependence on T_{2wat} . In contrast to T_{1wat} , the transition point is shifted to higher values of T_{2wat} for an increasing δ . In Fig. 5.21.c illustrating the influence of the ADC_{wat} , it can be seen that for the particular f_{wat} the signal is increasing with an increasing δ (paradoxical diffusion behavior) and that this increase is the stronger the higher the ADC_{wat} . For the ADC_{wat} of 0.58×10^{-3} mm²/s in normal-appearing vBM the increase was found to be ≈ 400 %.

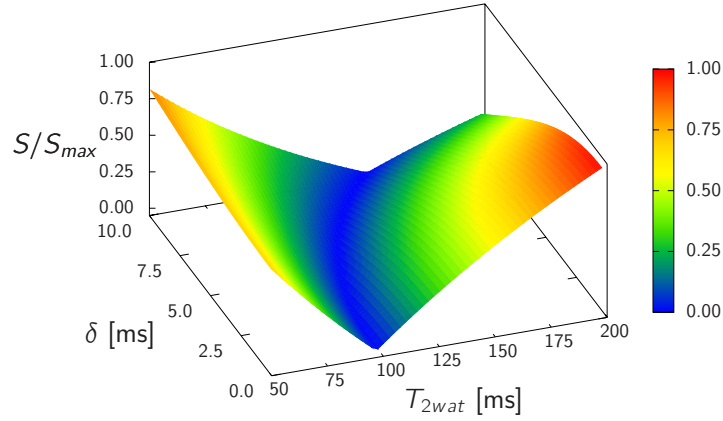
Afterwards, the behavior of the signal under the variation of the relaxation times of the fat component was simulated, keeping the parameters of the water component fixed at $T_{1wat} = 925$ ms, $T_{2wat} = 85$ ms, $ADC_{wat} = 0.6 \times 10^{-3}$ mm²/s and $f_{wat} = 70$ %. For an increasing T_{1fat} , the signal amplitude of the fat component and of the combined signal decreases, see Fig. 5.22.a. Under variation of T_{2fat} for a small δ , the signal decreases until the transition point is reached. For higher values of δ , the fat component is always dominant and the signal increases over the whole spectrum of T_{2fat} .

Furthermore, we investigated the change of the influence of the various parameters as a function of f_{wat} . In the region of values of f_{wat} that we found in the measurements, the influence of T_{1fat} (Fig. 5.23.b), is smaller than the effect of changes of T_{1wat} (Fig. 5.23.a). E.g. at $f_{wat} = 70$ %, an increase of 10 % of T_{1wat} leads to an increase of the signal of ≈ 30 %, while an increase of 10 % of T_{1fat} yields a decrease of ≈ 10 %. The changes caused by variations of T_{2wat} and T_{2fat} are bigger than those caused by the T_1 relaxation times (Fig. 5.23.c, 5.23.d). The effect of changes of T_{2wat} are more important than those of T_{2fat} at $f_{wat} = 70$ %, e.g. an increase of 10 % of T_{2wat} leads to an decrease of the signal of ≈ 36 %, while an increase of 10 % of T_{2fat} yields a increase of ≈ 23 %.

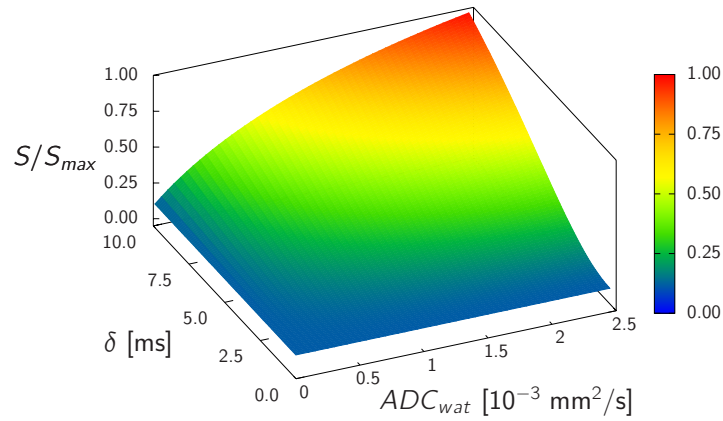
The evolution of R_{VCF} under variation of the T_2^* -values in the lesions and in



(a) $T_{2wat} = 85$ ms and $ADC_{wat} = 0.6 \times 10^{-3}$ mm²/s

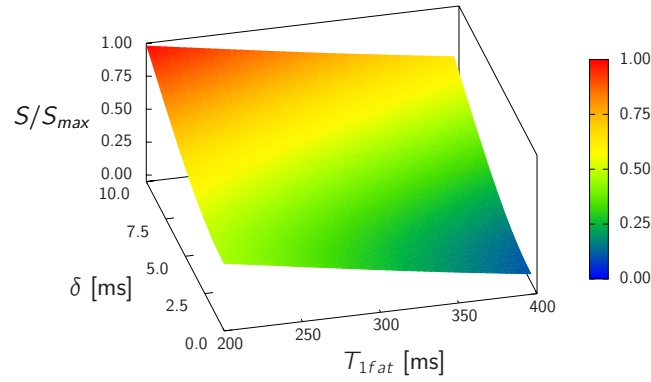


(b) $T_{1wat} = 925$ ms and $ADC_{wat} = 0.6 \times 10^{-3}$ mm²/s

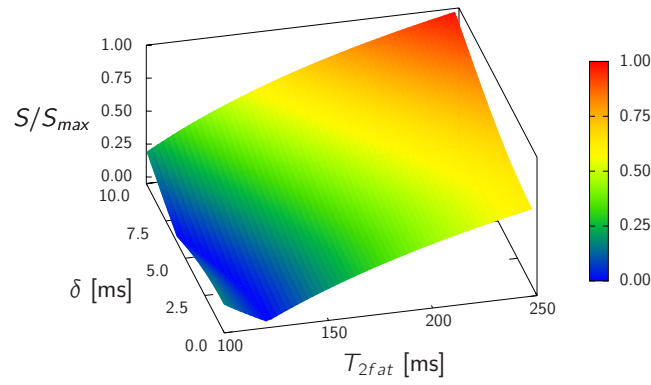


(c) $T_{1wat} = 925$ ms and $T_{2wat} = 85$ ms

Figure 5.21: Simulations of the DW-PSIF signal under variation of δ and the parameters of the water component, (a) T_{1wat} , (b) T_{2wat} and (c) ADC_{wat} . f_{wat} was set to 70%.

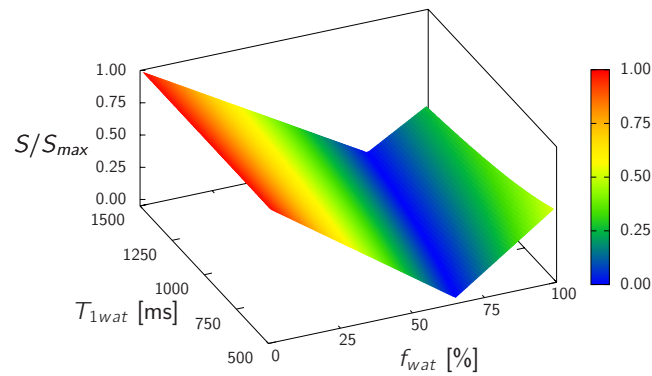


(a) $T_{2fat} = 150$ ms and $ADC_{fat} = 0.0 \times 10^{-3} \text{ mm}^2/\text{s}$

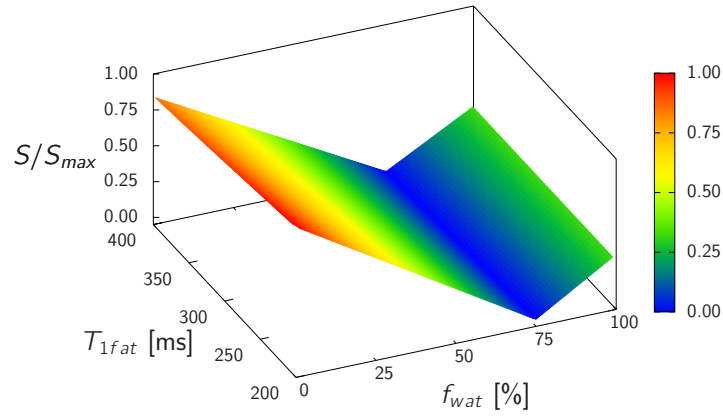


(b) $T_{1fat} = 300$ ms and $ADC_{fat} = 0.0 \times 10^{-3} \text{ mm}^2/\text{s}$

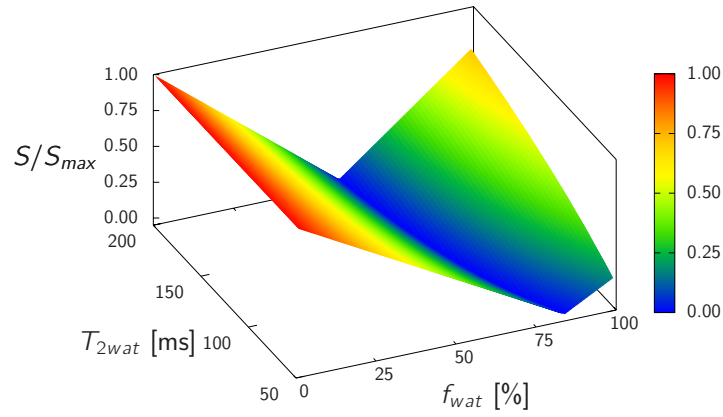
Figure 5.22: Simulations of the DW-PSIF signal under variation of δ and the parameters of the fat component, (a) T_{1fat} and (b) T_{2fat} . f_{wat} was set to 70%.



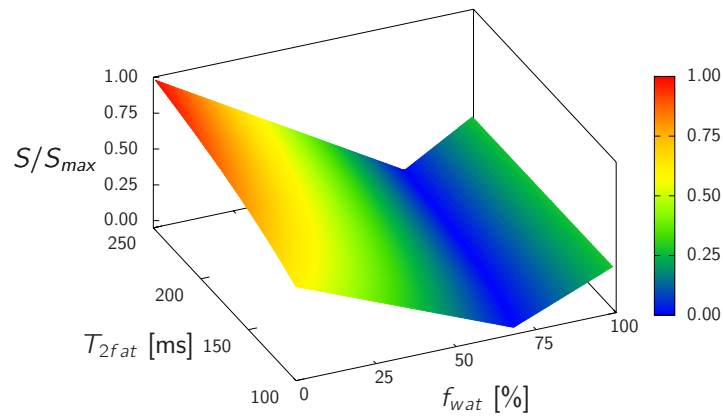
(a) $T_{2wat} = 85$ ms and $ADC_{wat} = 0.6 \times 10^{-3} \text{ mm}^2/\text{s}$



(b) $T_{2fat} = 150$ ms and $ADC_{fat} = 0.0 \times 10^{-3} \text{ mm}^2/\text{s}$



(c) $T_{1wat} = 925$ ms and $ADC_{wat} = 0.6 \times 10^{-3} \text{ mm}^2/\text{s}$



(d) $T_{1fat} = 300$ ms and $ADC_{fat} = 0.0 \times 10^{-3} \text{ mm}^2/\text{s}$

Figure 5.23: Simulations of the DW-PSIF signal under variation of the parameters of the water and fat component and f_{wat} . δ was set to 3 ms.

normal-appearing vBM are shown in Fig. 5.24. At a value of $T_{2vCF}^* = 21$ ms, that we found in the malignant infiltrations, a variation of T_{2vBM}^* about ± 50 % around the mean value leads to a decrease of 11 % or an increase of 43 % of R_{vCF} . At a value of $T_{2vCF}^* = 10$ ms, that we assumed for normal-appearing vBM, a variation of T_{2vCF}^* about ± 50 % around the mean value leads to decrease of 50 % or an increase of 27 % of R_{vCF} .

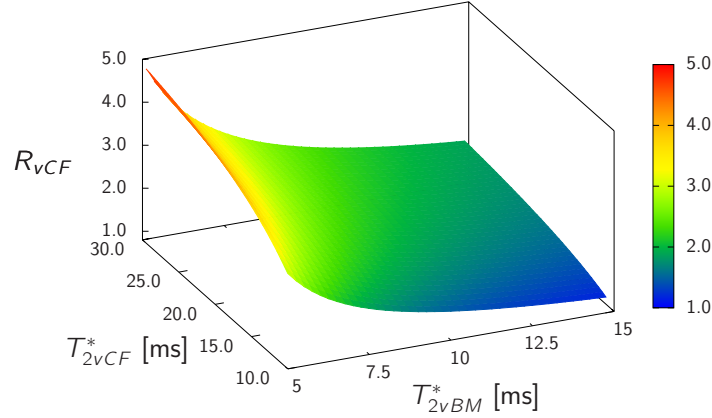


Figure 5.24: Simulations of R_{vCF} under variation of T_{2vBM}^* and T_{2vCF}^* . The other parameters are set to the mean values found in the patient group with malignant infiltrations and $T_E = 7.17$ ms.

In summary, the most important factors for the signal behavior at a T_E of 7.17 ms are f_{wat} , T_{2vCF}^* and T_{2vBM}^* . The effects of these parameters are most prominent in normal-appearing vBM. The effect of f_{wat} could be reduced by acquiring the signal in the in-phase situation. However, it was shown that this dramatically diminishes the difference between the R_{vCF} s of both patient groups. The effect of the relaxation times of both components as well as of the ADC of the water component is of course also related to the distribution pattern of fat and water. The larger the ratio of the water component the more sensitive the signal is to changes of the parameters of the water component. The effects of changes of the transversal relaxation times are larger than those of the longitudinal relaxation times. In contrast to other diffusion-weighted sequences, the influence of the ADC is not the only parameter responsible for the contrast behavior. At the diffusion weightings applied in the studies in the literature ($\delta = 3 - 5$ ms), the contrast is actually dominated by the effects of the other parameters, see Fig. 4.9. The signal of the DW-PSIF sequence is therefore not only diffusion-weighted, but rather experiences a combined weighting defined by ADC, T_1 ,

T_2 , f_{fat} and T_2^* . The main reason for the observed signal contrast between normal-appearing vBM and vCFs reported in the literature is not caused by differences of the ADCs, but rather by the differences of the T_2^* relaxation times and the distribution pattern of fat and water, especially in normal appearing vBM. In the following section we will compare the theoretically derived signal intensities for certain input parameters with the measured results of the signal behaviour of the DW-PSIF in vCFs as well as in normal-appearing vBM.

5.9 Signal Analysis

For the experimental analysis of the signal behavior of the DW-PSIF sequence, we acquired a sagittal slice (corresponding to the slice selected for the quantitative measurements described in the previous sections) with 5 different diffusion weightings. The amplitude of the diffusion gradient was kept constant at 23 mT/m, while the duration of the diffusion gradient was varied ($\delta = 0.5, 1.5, 3.0, 5.0, 7.4$ ms). The other sequence parameters were set as follows: a 256×192 matrix, $T_E = 7.17$ ms, corresponding to the opposed-phase situation, $T_R = 25$ ms, slice thickness 5 mm, a bandwidth of 100Hz/pixel and a FOV of 300×225 mm². The T_E of the sequence is rather an inverse T_E , corresponding to the time between the center of the readout of k-space and the RF pulse, as shown in Fig. 5.25. The acquisition time per image was 0:31 min resulting in a total acquisition time of 2:35 min.

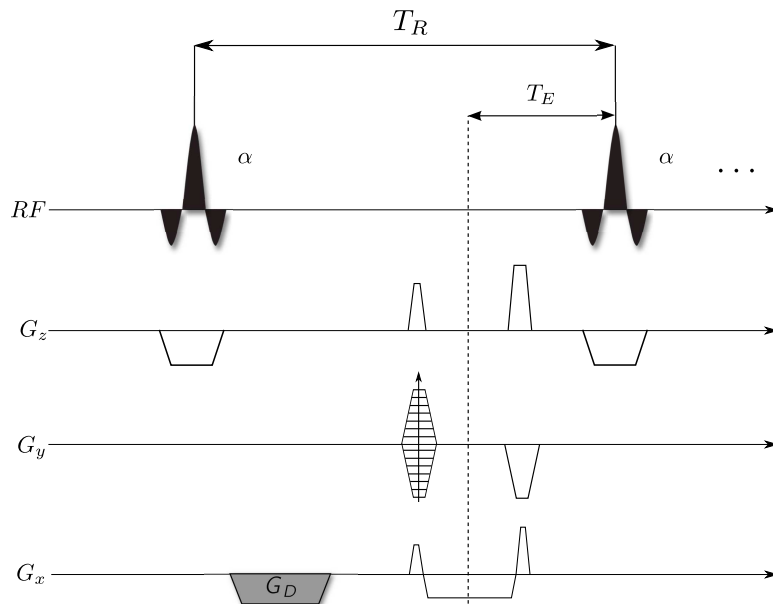
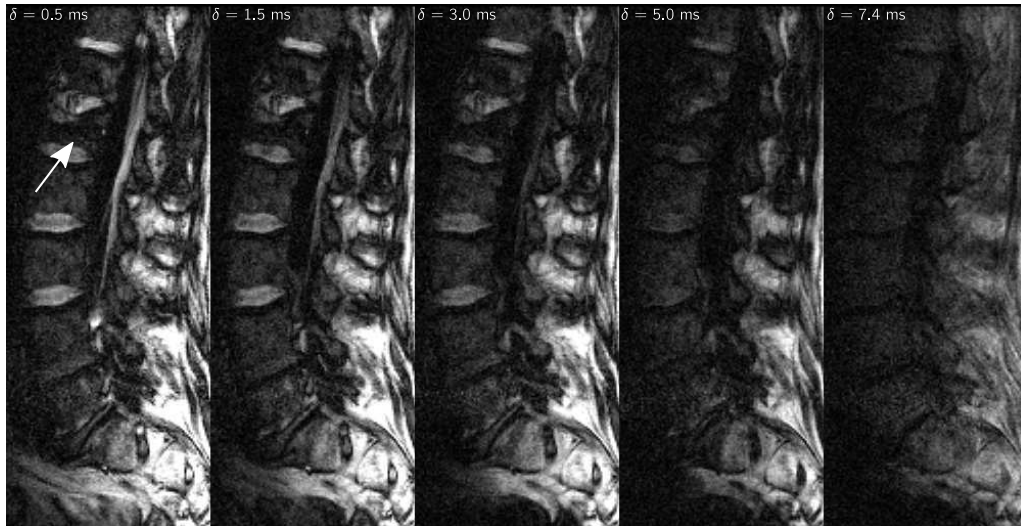


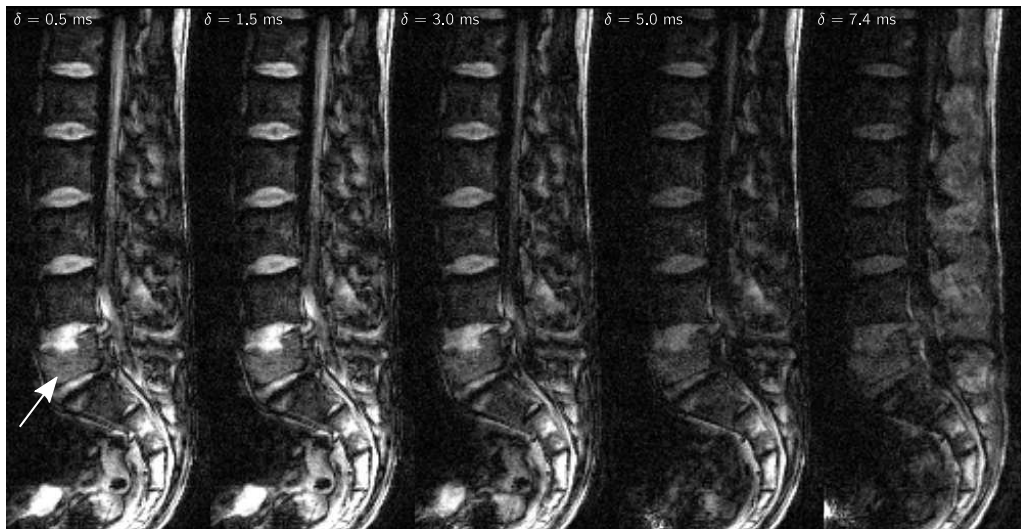
Figure 5.25: Sequence diagram of the DW-PSIF sequence.

Exemplary images with varying duration δ of the diffusion gradient are shown in Fig. 5.26. As already discussed in section 3.3.3, the fracture caused by a malignant infiltration appears hyperintense compared to the normal-appearing adjacent vertebrae, while the osteoporotic vCF appears hypointense.

In order to investigate the signal behaviour of the DW-PSIF sequence, we selected ROIs in normal-appearing vBM as well as in the vCF. The ROIs were matched with the ROIs selected for determination of the relaxation times and ADCs. Exemplary signal curves of the DW-PSIF as a function of δ for normal-appearing vBM and a



(a) Osteoporotic vCF



(b) Malignant vCF

Figure 5.26: DW-PSIF images of (a) a patient with an osteoporotic vCF in L1 and (b) a patient with a malignant vCF in L5 (arrows point at the vCFs). Images were acquired with a constant amplitude of the diffusion gradient and a variable duration δ .

vCF are shown for a patient with a malignant infiltration, Fig. 5.27, and a patient with an osteoporotic vCF, Fig. 5.28. In Fig. 5.29, we show the comparison of the ratio between the signal in the vCF and the corresponding normal-appearing vBM as a function of δ for the highlighted ROIs in these patients. In Fig. 5.30 the ratio between the vCF or normal-appearing vBM and the iVD are shown, respectively.

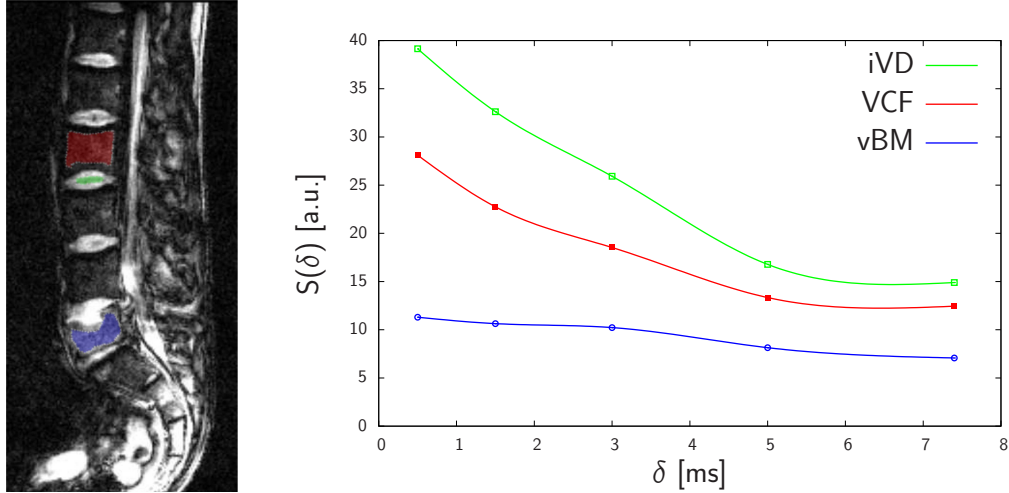


Figure 5.27: Reference image and the corresponding signal data as a function of δ for a patient with a malignant lesion in L5. Shown are the data for the lesion and for normal-appearing vBM in L2 and the adjacent iVD.

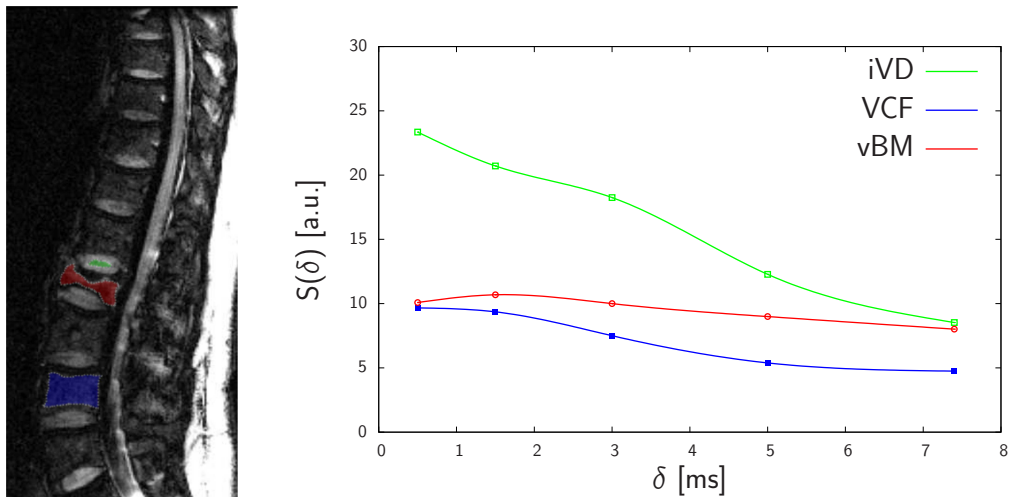


Figure 5.28: Reference image and the corresponding signal data as a function of δ for a patient with an osteoporotic lesion in L1. Shown are the data for the lesion and for normal-appearing vBM in L3 and the adjacent iVD.

As a first step we determined R_{vCF} for each δ in each patient. We calculated

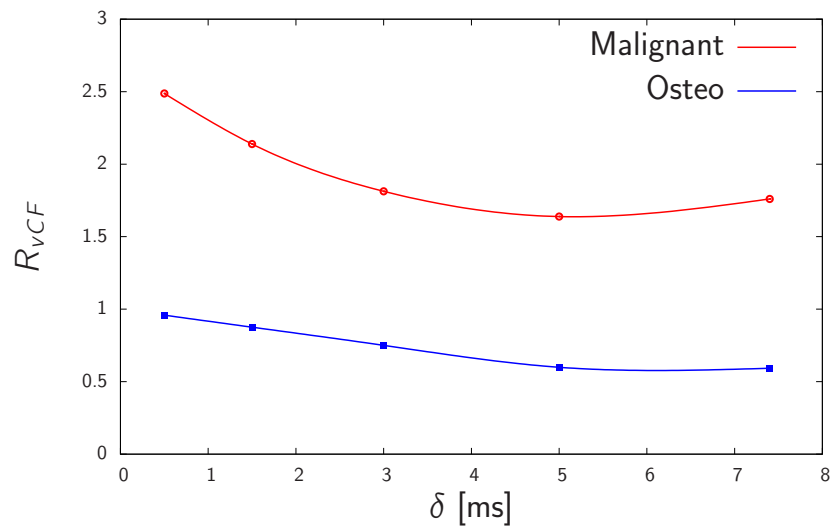


Figure 5.29: R_{vCF} for the patients shown in Fig. 5.27 and 5.28 as a function of δ .

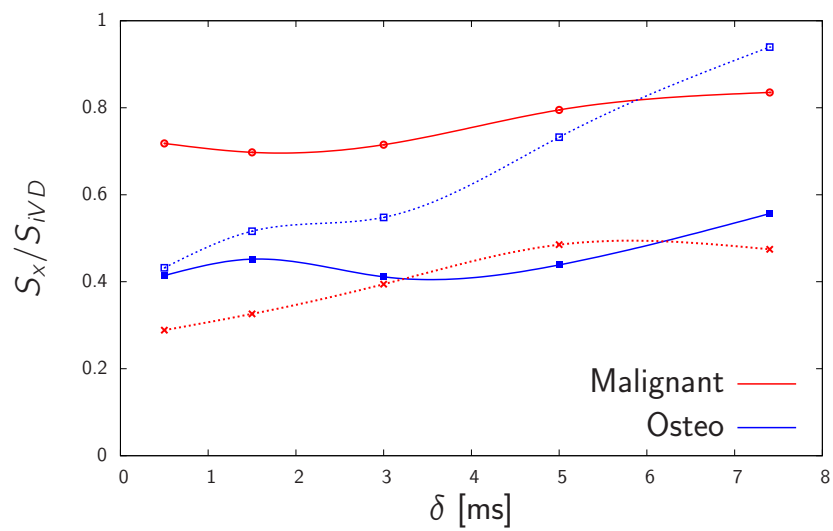


Figure 5.30: Ratios between the signal in the vCF and the iVD (solid line) and normal-appearing vBM and the iVD (dotted line) for the patients shown in Fig. 5.27 and 5.28 as a function of δ .

the mean values and standard deviations for each patient group and the results are summarized in Table 5.6. At each δ we investigated the significance of the differences of R_{vCF} between both patient groups, using a two-tailed unpaired t-test. A significant difference with $p < 0.001$ was found for each δ . For each δ we calculated the sensitivities, specificities and accuracies with regard to the diagnose of a malignant lesion based on the R_{vCF} . The criteria for the choice of the cut-off value was the maximization of the accuracy. In previous studies, the classification was performed using a qualitative criterion, i.e. the relative signal contrast, and therefore the results cannot be compared directly. Still, the cut-off value of 1.52, found at $\delta = 3.0$ ms, agrees more or less with the qualitative result that hypo- and iso-intensity of the vCFs are an indicator for a benign cause. The highest sensitivities and specificities were found at a δ of 1.5 and 3.0 ms. The results are summarized in Table 5.7.

R_{vCF}	Osteoporosis	Malignant
$\delta = 0.5$ ms	1.01 (0.38)	3.43 (1.93)*
$\delta = 1.5$ ms	0.97 (0.38)	3.40 (1.81)*
$\delta = 3.0$ ms	0.85 (0.31)	2.80 (1.42)*
$\delta = 5.0$ ms	0.69 (0.20)	2.06 (0.84)*
$\delta = 7.4$ ms	0.69 (0.19)	1.23 (0.42)*

Table 5.6: Summary of the mean values and standard deviations (shown in parentheses) of R_{vCF} for patients with osteoporotic and malignant vCF. A * indicates a significant difference ($p < 0.05$) between the values in both patient groups.

R_{vCF}	Cut-off	Sensitivity	Specificity	Accuracy
$\delta = 0.5$ ms	1.85	85	100	93
$\delta = 1.5$ ms	1.82	95	100	98
$\delta = 3.0$ ms	1.52	90	100	95
$\delta = 5.0$ ms	1.29	85	100	93
$\delta = 7.4$ ms	0.98	79	95	87

Table 5.7: Summary of the cut-offs, sensitivities, specificities and accuracies for the diagnose of a malignant lesion based on R_{vCF} .

In the previous sections, we derived the relaxation times and the ADCs and as

shown in Fig. 5.19.a we already simulated the signal behaviour of R_{vCF} for these parameters at a T_E of 7.17 ms. In Fig. 5.31, we show the correspondence between these simulations and the measured mean values of R_{vCF} . The R_{vCF} is influenced

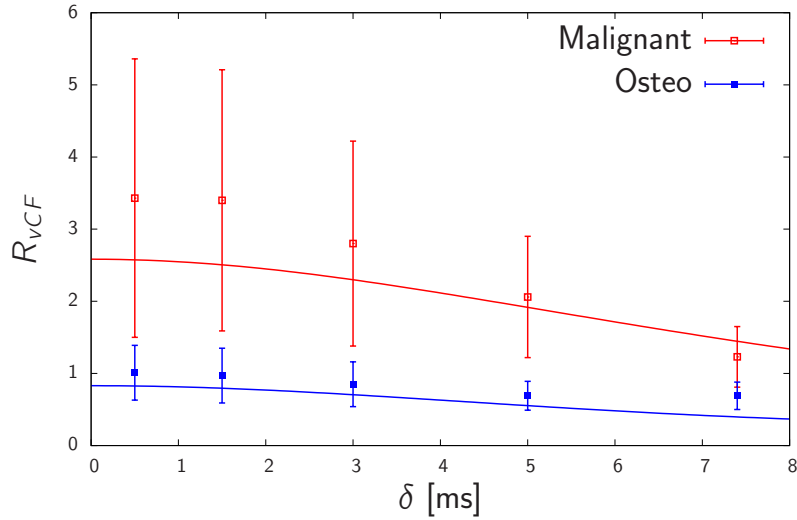


Figure 5.31: Comparison between the mean values of R_{vCF} (squares with errorbars) and the simulation (solid lines) based on the parameters. The length of the errorbars corresponds to twice the standard deviation.

by the signal in normal-appearing vBM and the signal in the vCFs. Both signals were found to deviate between the patient groups. The mean signal intensities in the iVDs of both patient groups were found to be comparable, in agreement with the simulations. Hence, the signal in the iVDs can be used to normalize the signal intensities of normal-appearing vBM and the vCFs separately. The results of the measured and simulated ratios between normal-appearing vBM and accordingly vCF and the iVD are shown in Fig. 5.32. It can be seen in Fig. 5.32.a, that the signal in the malignant vCFs is ≈ 50 % higher compared to osteoporotic vCFs, if we assume the signal of the iVDs to be equal. On the other hand, in Fig. 5.32.b, it is demonstrated that in the case of normal-appearing vBM the situation is reverse, the signal in the osteoporotic group is ≈ 40 % higher than in the group with malignant infiltrations. These opposed effects explain the significant difference between the R_{vCF} s. Apart of the signal ratio between normal-appearing vBM and the iVD, in the osteoporotic group the simulations and the measured data agree within the $2\text{-}\sigma$ environment of the measured data. Possible reasons for the disagreement in the case of osteoporotic normal-appearing vBM might be an underestimation of f_{wat} or an overestimation of T_{2vBM}^* .

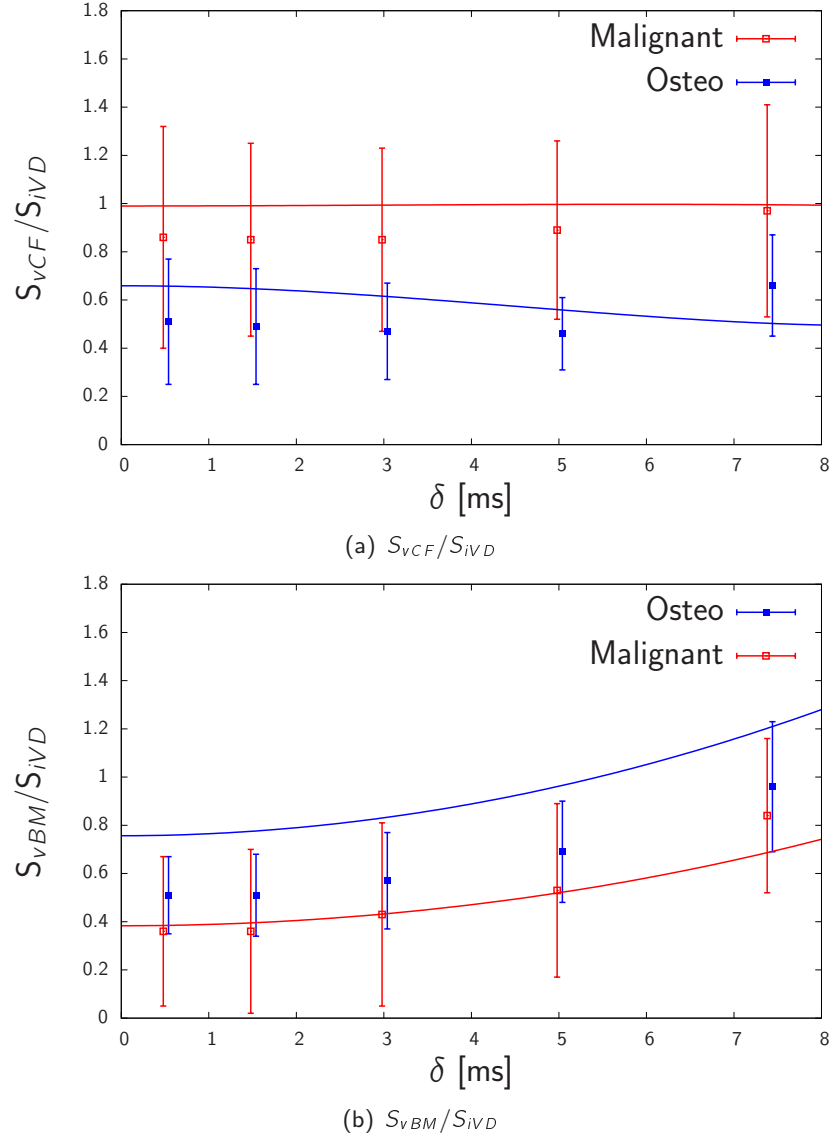
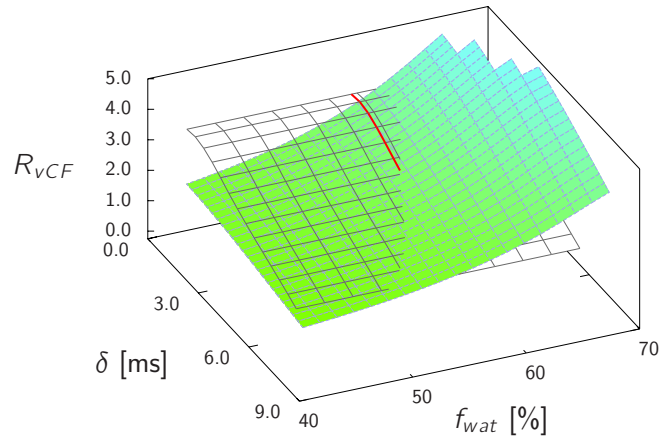
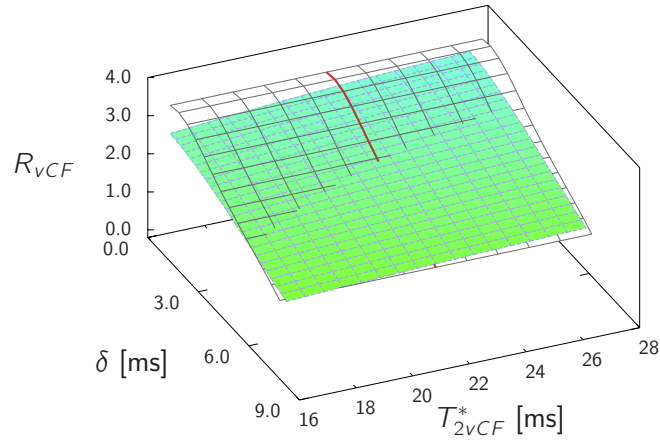
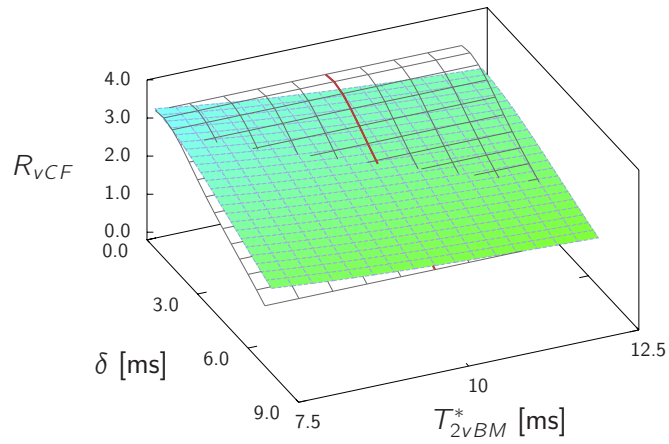


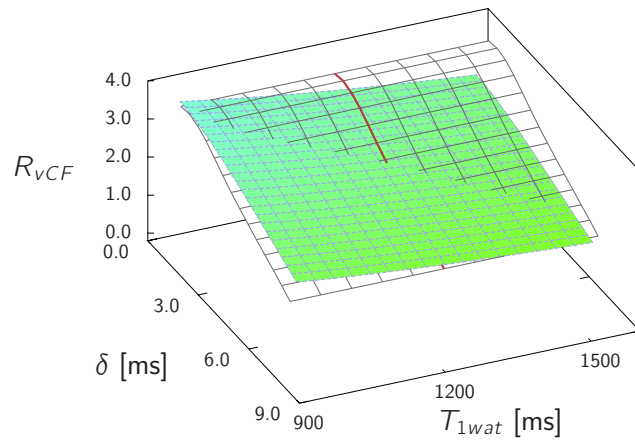
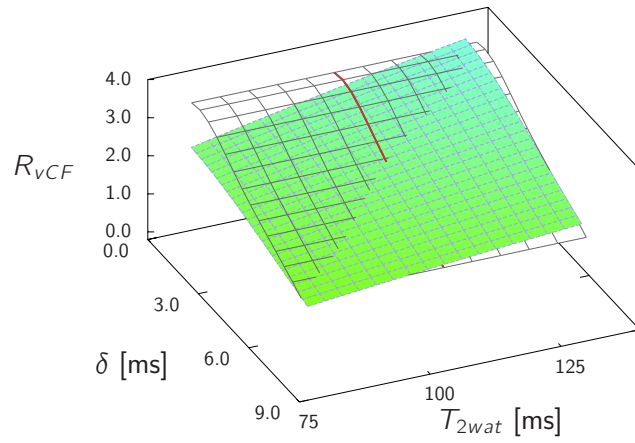
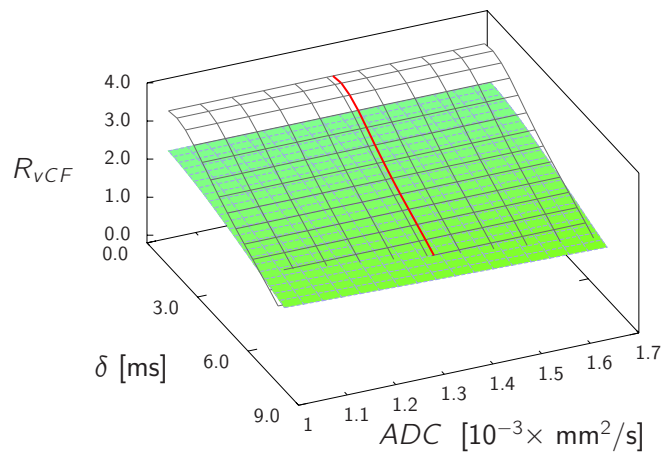
Figure 5.32: Comparison between the mean values of S_X/S_{iVD} (squares with errorbars) and the simulation based on the parameters, where X is vCF in (a) and normal-appearing vBM in (b). The length of the errorbars corresponds to twice the standard deviation.

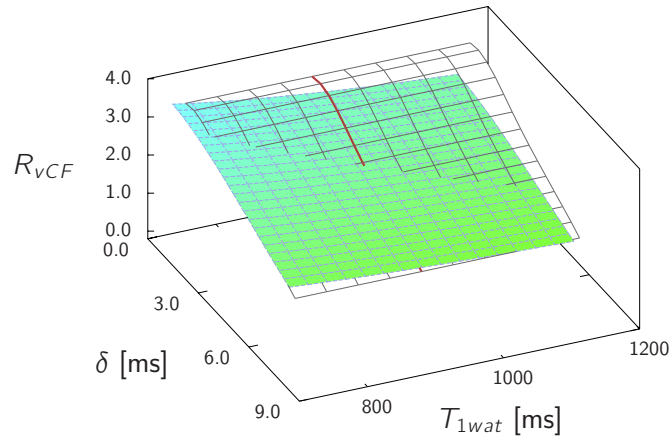
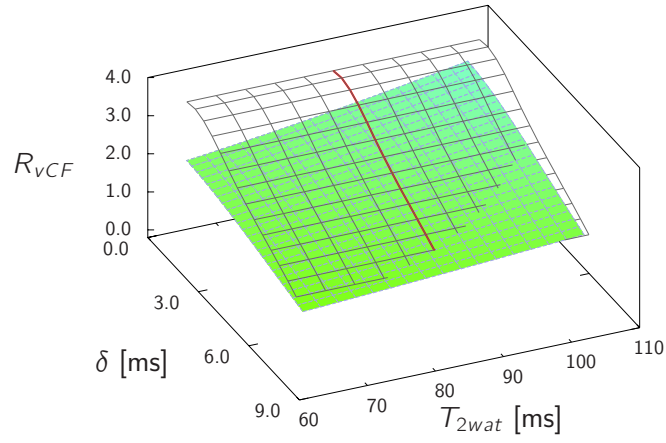
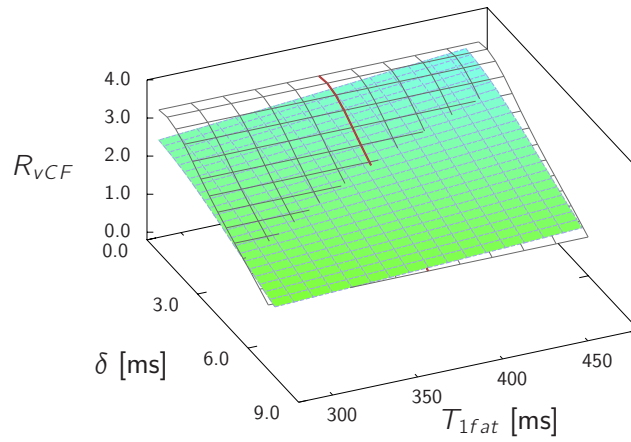
We performed additional simulations to investigate, which variations of the input parameters, corresponding to potential measurements errors, lead to a better agreement between the measured and simulated data. For the patient group with malignant infiltrations, we varied each parameter individually in a range of $\pm 25\%$ about the mean value, keeping the other parameters fixed at the mean values determined before. As can be seen in Fig. 5.33.a, a small increase of f_{wat} already causes a transformation of the simulated curve, leading to a potentially better agreement between simulation and data. The best agreement was found for a f_{wat} of 61 %. For the rest of the parameters, the variations lead to smaller transformations of the simulated signal curve. Hence, only very large measurement errors could explain the disagreement. The biggest effects were found for the T_2 -values in Fig. 5.33.e, 5.33.h and 5.33.j. The influence of the ADCs is negligible, see Fig. 5.33.f and 5.33.k, especially at the values of δ where the sensitivities and specificities were found to be the highest.

In addition, we compared the measured signal of the DW-PSIF sequence with the signal model for each patient individually. The comparison of the simulated and measured signal ratios is shown in Fig. 5.34. In some cases, the simulated values deviate strongly from the measured values. This might partially be caused by singularities in the denominator, happening when f_{wat} of normal-appearing vBM is close to or at the transition point between the water- and fat-dominated regime. In order to avoid these singularities, we also calculated the signal difference between the vCF and normal-appearing vBM and normalized it by the sum of both. The measured and simulated values of the normalized differences are shown in Fig. 5.35.

In summary, the evolution of the signal in the simulations agrees quite well with the values of the measurements. Comparing the signal ratios between normal-appearing vBM and the iVDs and vCFs and iVDs, we could show for the measurements, that the signal contrast between osteoporotic and malignant lesions is caused by two effects. First, the signal in normal-appearing vBM of patients with osteoporosis is increased compared to the patient group with malignant infiltrations. Second, the signal in the malignant vCFs is higher than in the osteoporotic vCFs. Both effects lead to an increase of the R_{vCF} in the malignant group compared to the osteoporotic group. As we saw in the last sections, the parameters showing the biggest differences between both patient groups in normal-appearing vBM were f_{wat} , T_{2fat} and T_{1fat} . As shown in the signal simulations, the changes caused by variations of the relaxation times are small compared to f_{wat} . Hence, the contrast originating from normal-appearing vBM is not diffusion-weighted, since the ADCs are almost equal, but rather fat-weighted. The decrease of f_{wat} in normal-appearing vBM of patients with osteoporosis agrees

(a) Variation of f_{wat} (b) Variation of T_{2VCF}^* (c) Variation of T_{2VBM}^*

(d) Variation of T_{1wat} of the lesion(e) Variation of T_{2wat} of the lesion(f) Variation of ADC_{wat} of the lesion

(g) Variation of T_{1wat} of normal-appearing vBM(h) Variation of T_{2wat} of normal-appearing vBM(i) Variation of T_{1fat} of normal-appearing vBM

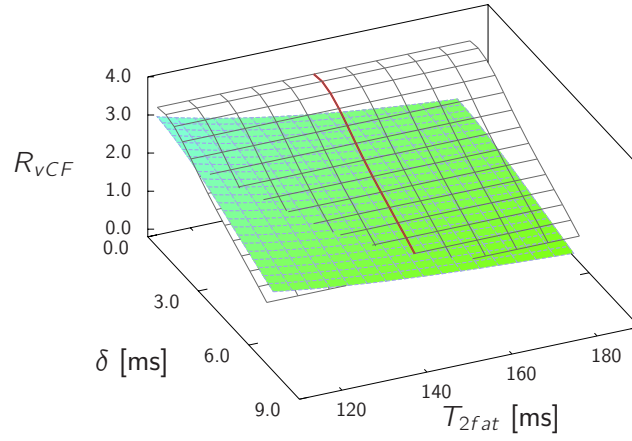
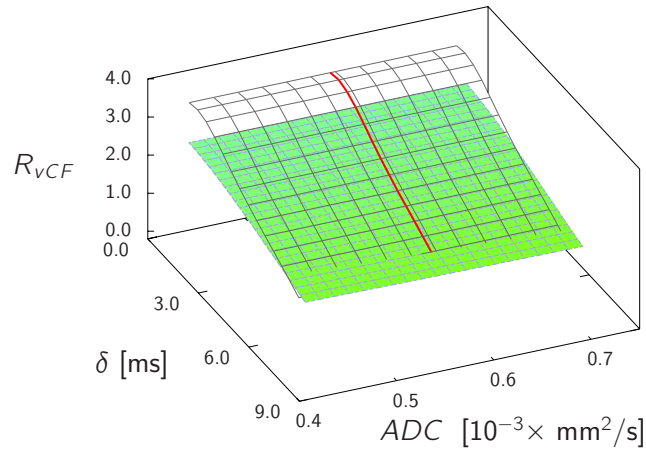
(j) Variation of T_{2fat} of normal-appearing vBM(k) Variation of ADC_{wat} of normal-appearing vBM

Figure 5.33: Evaluation of the simulated R_{VCF} as a function of δ and one parameter (shown as the colored area) for a variation of $\pm 25\%$ about the mean value in the patient collective with malignant lesions. For reference the gray lattice shows the measured R_{VCF} . The red line shows the evolution at the mean value of the varied parameter.

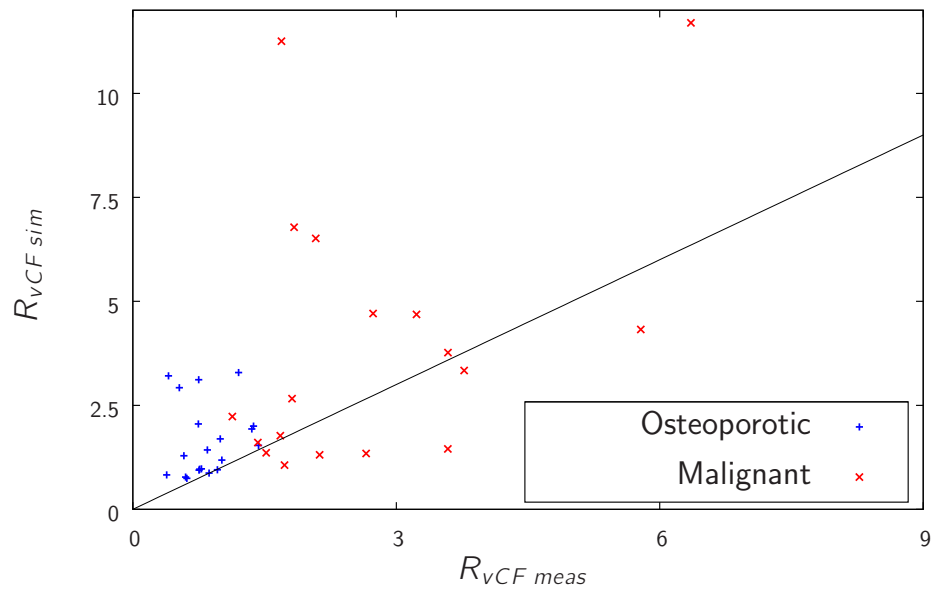


Figure 5.34: Individual comparison between the simulated and measured values of R_{vCF} . For better orientation, a diagonal line corresponding to $R_{vCF\ sim} = R_{vCF\ meas}$ has been added to the plot.

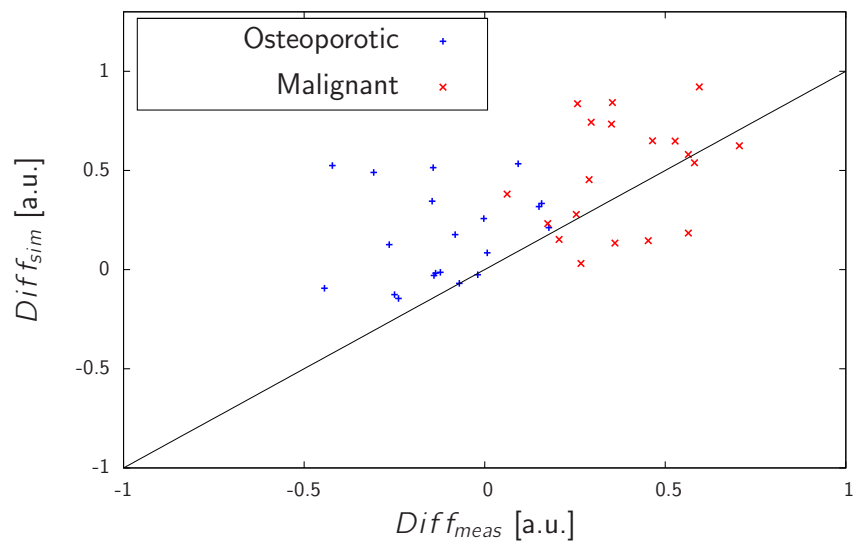


Figure 5.35: Individual comparison between the simulated and measured values of the normalized differences between the signal in normal-appearing vBM and vCF. For better orientation, a diagonal line corresponding to equal values for the simulations and measurements has been added to the plot.

well with the literature [150, 149]. It was also reported by Yeung et al. [99] that while f_{wat} decreased significantly in patients with osteoporosis, no significant change of the ADC compared to healthy patients was found. In the vCFs the signal difference is partially explained by the different ADCs. But in addition to the diffusion weighting, the contrast is also T_2^* -weighted and fat-weighted. At a δ of 3 ms the signal decrease in the osteoporotic vCFs caused by the ADC is $\approx 3\%$. The contrast caused by the decreased T_2^* in the osteoporotic patient group leads to a signal decrease of $\approx 22\%$ compared to the malignant group. The decrease of f_{wat} in the osteoporotic vCFs causes a decline of the signal of $\approx 30\%$. Hence, the diffusion weighting is negligible compared to the other parameters. Combining both effects, the observed signal contrast between both patient groups at a small δ is not diffusion-weighted as it was described in the literature, but is rather fat- and T_2^* -weighted.

Of course, the diffusion-weighting could be increased, if the signal ratios at a larger δ were compared. However, an increase of δ , leads to a significant loss of SNR, and a reliable evaluation of the images is not possible anymore. If it is desirable to obtain pure diffusion-weighted images, a DW-EPI or DW-ssTSE sequence should be preferred. Nevertheless, the sequence allowed for the differentiation of the lesions with a very high accuracy. Since the diffusion weighting seems to be negligible for the DW-PSIF at small δ , it might be better to omit the diffusion gradient. To increase the sensitivity to the fat-weighting, images could be obtained at a shorter T_E (e.g. 2.38 ms) to increase the SNR. Yet, this effect would be partially counterbalanced by a decreased bandwidth. For an increased T_2^* -weighting, images should be acquired in the in-phase situation to increase the signal amplitudes and at longer T_E . It should be verified in future studies, which of the potential sequence modifications provides a better lesion differentiation. On the other hand, the high sensitivity and specificity obtained with the current sequence settings indicate, that the combined contrast due to T_2^* - and fat-weighting is possibly the best choice, if combined with the correct interpretation.

Chapter 6

Summary

A very important question in MRI of the spine that arises in clinical practice is the differential diagnosis between benign osteoporotic and pathological vertebral compression fractures. Based on the contrast of conventional MRI sequences, this is a complicated task, since both entities are characterized by an easily confusable appearance on MR images, i.e. a hypointense signal on T_1 -weighted images and a hyperintense signal on T_2 -weighted or STIR images. Diffusion-weighted imaging has shown to be a very promising technique to serve as a tool for the differentiation of these two entities. In previous studies of DWI of the spine, in particular, a certain type of a diffusion-weighted steady-state-free-precession sequence, namely the DW-PSIF sequence, has shown to be very valuable. The qualitative assessment of the DW-PSIF images showed that in general, osteoporotic fractures appeared hypo- to isointense, while pathological fractures appeared hyperintense [12]. Yet, contradictory results were reported for the differential diagnosis based on this contrast. While Baur et al. [18] reported a sensitivity of 100 % and a specificity of 93 %, Castillo et al. [19] found no advantages of DWI compared with conventional imaging. So far a physical understanding of the signal contrast observed on DW-PSIF images in the spine is still lacking. This PhD thesis addresses this problem, performing an extensive quantitative analysis of the signal formation.

In order to perform a theoretical analysis of the signal formation it is necessary to analyze the exact signal function of the DW-PSIF sequence. In chapter 4, we reviewed the derivation of the signal function of the DW-PSIF sequence. In contrast to a simple diffusion-weighted spin-echo sequence, the DW-PSIF signal is a complicated function of the T_1 and T_2 relaxation times as well as of the apparent diffusion coefficient.

This model correctly describes the situation in most tissues of the body. Yet, in vertebral bone marrow the situation is more involved. First, the signal is effectively

the combination of two signals, the water and fat signal, which are both of the same order of magnitude. Hence, it is required to know the exact distribution pattern of both components to be able to properly model the signal behavior. Furthermore, the signal derivation was based on the hypothetical assumption that the signal is acquired directly at the application of the RF pulse. In a realistic measurement the time span between the image acquisition and the application of the RF pulse has to be incorporated by adding a T_2^* -weighting factor to the signal model. In most parts of the body typical T_2^* relaxation times are so long that for short T_E s, as used in the DW-PSIF, this effect can be neglected. However, the difference in susceptibility between trabecular bone and bone marrow results in a strong reduction of T_2^* in vertebral bone marrow and the T_2^* -weighting has to be considered. In chapter 5, we developed a signal model of the DW-PSIF sequence in vertebral bone marrow, incorporating both effects. Overall, we found that this signal model depends on 9 parameters.

To understand the signal contrast, it was necessary to model the signal in vertebral fractures of patients with benign osteoporotic and pathological fractures, but also in normal vertebral bone marrow. Since reference values for most of the parameters did not exist in the literature, this required to determine these parameters in separate measurements. In a patient collective of 20 patients with benign osteoporotic and 20 patients with pathological fractures, all parameters were determined separately. It was found that most of the parameters differed significantly between the fractured and non-fractured vertebrae. Furthermore, parameters like T_2^* , ADC and the water fraction also differed significantly between both fracture types. Interestingly, the water fraction also differed significantly between non-fractured vertebrae of both patient collectives, in agreement with previous studies that showed a correlation between the degree of osteoporosis in terms of the bone mineral density and the decrease of the water fraction. Based on the mean values of the parameters, simulations of the signal ratio of neighboring fractured and normal-appearing vertebrae were performed. These simulations demonstrated that especially the choice of the echo time, T_E , has a strong effect on the contrast behavior. While in the in-phase situation the signal ratios for both types of fractures were very similar, a very strong separation was found in the opposed-phase situation.

We compared the simulated signal behavior with DW-PSIF measurements in the patients and a good agreement was found. Hence, the model seems to correctly describe the signal characteristics in vertebral bone marrow. The measurements also confirmed the excellent differentiation between both types of fractures reported in previous studies. The signal ratio alone does not allow to identify whether a change of

the contrast is caused by the fractured or the neighboring normal-appearing vertebrae. Using the signal of the intervertebral disc as a normalizing reference, we could show that the difference of the signal ratio is caused by two effects. First, the signal in the normal-appearing vertebrae of the osteoporotic group is significantly higher than in the pathological group. This increase is mainly caused by a decreased water fraction in the osteoporotic group, i.e. this is a fat-weighted contrast. Second, the signal in the pathological fractures is significantly higher than in the osteoporotic fractures. This increase is mainly caused by an increased water fraction and T_2^* in the pathological fractures, while the influence of the ADC is negligible. Both effects together are responsible for the different signal ratios, i.e. hypo- to isointensity of osteoporotic and hyperintensity of pathological fractures. At the diffusion weightings that provided the best qualitative differentiation, the influence of the ADC on the signal ratio is negligible compared to T_2^* and the water fraction. Hence, the observed contrast in the case of vertebral fractures is a combined effect of the fat- and T_2^* -weighting rather than a diffusion-weighted contrast.

In summary, we provide for the first time a detailed theoretical and experimental analysis of the diffusion-weighted signal in patients with vertebral fractures. We could show that our theoretical model describes the signal in vertebral bone marrow reasonably well. We confirmed that the DW-PSIF sequence provides an excellent differentiation between benign osteoporotic and pathological vertebral fractures. In contrast to the usual assumption that this differentiation is mainly caused by the different diffusion properties of the fractures, we demonstrated that the diffusion weighting has only a minor effect on the observed signal contrast. We showed that the main cause for the signal contrast is the fat-weighting and to a lesser degree the T_2^* -weighting. Hence, the signal strongly depends on the choice of the T_E , which might also be responsible for the inconsistent results published in the literature.

Zusammenfassung

Eine wichtige Fragestellung, die sich bei Anwendung der Magnetresonanztomographie im Bereich der Wirbelsäule ergibt, ist die Differentialdiagnose zwischen osteoporotischen und malignen Wirbelkörperfrakturen. Die Differenzierung mit Hilfe der konventionellen MRT ist nicht immer eindeutig, da beide Frakturtypen durch sehr ähnliches Signalverhalten charakterisiert sind. Beide zeigen ein hypointenses Signal auf T_1 -gewichteten Bildern und ein hyperintenses Signal auf T_2 -gewichteten oder STIR-Bildern. In den letzten Jahren zeigte sich, dass die diffusionsgewichtete MR-Bildgebung ein vielversprechendes Verfahren zur Differentialdiagnostik dieser beiden Frakturtypen darstellt. Dabei erwies sich in früheren Studien insbesondere eine spezielle diffusionswichtende SSFP-Sequenz, die DW-PSIF-Sequenz, als besonders geeignet. Die qualitative Analyse der mit der DW-PSIF-Sequenz aufgenommenen Bilder zeigte, dass im Allgemeinen osteoporotische Frakturen ein hypo- bis isointenses Signal und maligne Frakturen ein hyperintenses Signal aufweisen [12]. Im Einzelnen sind die Ergebnisse hinsichtlich der sicheren Erkennbarkeit pathologischer Frakturen jedoch durchaus uneinheitlich. Einerseits konnten Baur et al. [18] bei ihrer Auswertung ein Sensitivität von 100 % und eine Spezifität von 93 % erzielen, andererseits ergab sich beispielsweise in einer Studie von Castillo et al. [19], dass der diffusionsgewichtete Kontrast keine verbesserte Differenzierung im Vergleich zur konventionellen Bildgebung ermöglichte. Bislang mangelte es an einem tieferen physikalischen Verständnis des mit der DW-PSIF-Sequenz beobachteten Signalkontrastes. Die vorliegende Dissertation setzt sich mit dieser Fragestellung auseinander. Dazu wurde eine ausführliche theoretische Analyse der Signalbildung der DW-PSIF-Sequenz in Wirbelkörpern durchgeführt.

Für die Durchführung dieser theoretischen Analyse ist eine genaue Kenntnis der exakten Signalfunktion der DW-PSIF-Sequenz erforderlich. In Kapitel 4 wurde deshalb kurz die mathematische Herleitung der Signalfunktion dargestellt. Im Gegensatz zu einer einfachen diffusionswichtenden Spin-Echo-Sequenz zeichnet sich die Signalfunktion der DW-PSIF-Sequenz durch eine komplizierte Abhängigkeit von den T_1 -

und T_2 -Relaxationszeiten sowie dem Diffusionskoeffizienten aus.

Dieses Modell liefert im überwiegenden Teil des menschlichen Körpers eine korrekte Beschreibung des Signals. Im vertebrealen Knochenmark ist die Signalbildung jedoch komplizierter. Im Wirbelkörper wird ein effektives Signal gemessen, das sich aus der Summe des Fett- und Wassersignals ergibt. Im Knochenmark liegen die Anteile beider Komponenten und somit auch deren Signalintensitäten in der gleichen Größenordnung und eine genaue Quantifizierung der relativen Anteile der beiden Signalkomponenten ist deshalb für die Signalanalyse notwendig. Darüber hinaus basiert das Signalmodell auf der hypothetischen Annahme, dass die Bilder unmittelbar vor der Applikation des folgenden HF-Pulses aufgenommen werden. In der Praxis sind die Signalakquisition und die Applikation des HF-Pulses jedoch durch eine kurze Zeitspanne, die Echozeit T_E , voneinander getrennt. Diese zeitliche Trennung führt zu einer zusätzlichen Abschwächung des Signals durch die T_2^* -Relaxation. In den meisten Gewebearten sind die typischen T_2^* -Zeiten so lang, dass diese Abschwächung vernachlässigt werden kann. Im Wirbelkörper jedoch führt der große Unterschied zwischen den Suszeptibilitäten der Trabekel und des Knochenmarks zu einer starken Reduktion der T_2^* -Zeit und die T_2^* -Relaxation muss in Form eines zusätzlichen Faktors in der Signalgleichung berücksichtigt werden. In Kapitel 5 wurde ein erweitertes Signalmodell der DW-PSIF-Sequenz entwickelt, das diese Effekte miteinbezieht und somit eine korrekte Analyse des Signals im vertebrealen Knochenmark erlaubt. Insgesamt wird das Signalverhalten im kompletten Signalmodell durch 9 unterschiedliche Parameter beeinflusst.

Um den beobachteten Signalkontrast zu verstehen muss das Signal sowohl in osteoporotischen und pathologischen Wirbelkörperfrakturen als auch in normalem Knochenmark simuliert werden. Für die meisten der Parameter existieren keine Referenzwerte in der Literatur und sie mussten deshalb in separaten Messungen bestimmt werden. In einem Patientenkollektiv, bestehend aus 20 Patienten mit osteoporotischen und 20 Patienten mit pathologischen Frakturen wurden alle 9 Parameter separat für normales Knochenmark und in den Frakturen bestimmt. Dabei zeigte sich, dass fast alle Parameter signifikante Unterschiede zwischen normalem Knochenmark und den Frakturen aufwiesen. Im Falle von T_2^* , dem Diffusionskoeffizienten und dem Fettanteil fanden sich auch zwischen den beiden Frakturtypen signifikante Unterschiede. Interessanterweise ergab sich für den Fettanteil in normalem Knochenmark auch eine signifikante Abweichung zwischen den beiden Patientengruppen. Dies bestätigte die Ergebnisse früherer Studien, in denen eine signifikante Korrelation zwischen dem Grad einer osteoporotischen Erkrankung, bestimmt durch eine Knochendichtemessung, und dem Ansteigen des Fettanteils gefunden wurde. Unter Verwendung der Mittelwerte der gemessenen Parameter wurde dann eine Simulation des Signalverhältnisses zwi-

schen frakturierten und normalen Wirbelkörpern durchgeführt. In diesen Simulationen zeigte sich, dass insbesondere die genaue Wahl der Echozeit T_E einen erheblichen Einfluss auf das Kontrastverhalten hat. Während sich im In-Phase-Zustand die Signalverhältnisse beider Frakturtypen ähneln, ergab sich im Opposed-Phase-Zustand ein signifikanter Unterschied.

Der Vergleich der simulierten Signalkurven mit in den Patienten durchgeführten DW-PSIF-Messungen zeigte eine gute Übereinstimmung; dies deutet darauf hin, dass das Signalmodell eine korrekte Beschreibung des Signalverhaltens liefert. Die in der Vergangenheit beschriebene exzellente Differenzierbarkeit der Frakturtypen konnte durch unsere Messungen bestätigt werden. Das Signalverhältnis alleine erlaubt jedoch keine Rückschlüsse darauf, ob der Kontrast durch die benachbarten normalen Wirbelkörper oder die Frakturen selbst entsteht. Unter Verwendung des Signals der Bandscheiben als normierender Referenz konnte gezeigt werden, dass der Kontrast im Wesentlichen durch zwei Effekte bestimmt wird. Zunächst ist das Signal der normalen Wirbelkörper in Patienten mit Osteoporose signifikant höher als bei Patienten mit malignen Infiltrationen. Die Hauptgrund für die erhöhte Signalintensität liegt dabei im erhöhten Fettanteil der osteoporotischen Wirbelkörpern begründet. Darüber hinaus ist das Signal in den pathologischen Frakturen im Vergleich zu den osteoporotischen Frakturen signifikant erhöht. In diesem Fall wird der Signalunterschied vor allem durch den verminderten Fettanteil und die erhöhte T_2^* -Relaxationszeit in den pathologischen Frakturen verursacht. Der Einfluss des erhöhten Diffusionskoeffizienten in den osteoporotischen Frakturen ist dagegen vernachlässigbar. Das Zusammenspiel dieser Effekte ist letztlich für die signifikant unterschiedlichen Signalverhältnisse, d.h. hypo- bis isointenses Signal in den osteoporotischen und hyperintenses Signal in den pathologischen Frakturen, verantwortlich. Im Falle derjenigen Diffusionswichtungen, bei denen die qualitative Analyse die beste Differentialdiagnose ermöglichte, ist der Effekt der unterschiedlichen Diffusionskoeffizienten gegenüber den durch unterschiedliche T_2^* -Werte und Fettanteile verursachten Effekten vernachlässigbar. Insgesamt lässt sich damit feststellen, dass es sich bei dem beobachteten Kontrast um einen kombinierten T_2^* - und fettgewichteten Kontrast, und weniger um einen diffusionsgewichteten Kontrast handelt.

In dieser Arbeit wurde erstmals eine theoretische und experimentelle Analyse des diffusionsgewichteten Signals in Patienten mit Wirbelkörperfrakturen durchgeführt. Es konnte gezeigt werden, dass das entwickelte Signalmodell eine gute Beschreibung des gemessenen Signalverhaltens in vertebralem Knochenmark liefert. Die Ergebnisse früherer Studien, die basierend auf dem Signalkontrast der DW-PSIF-Sequenz eine exzellente Differentialdiagnose zwischen pathologischen und osteoporotischen Wirbel-

körperfrakturen ermöglichten, bestätigten sich in unserer Arbeit. Im Gegensatz zur bisherigen Annahme, dass diese Differenzierung vor allem in den unterschiedlichen Diffusionscharakteristika der Frakturen begründet liegt, konnten wir zeigen, dass die Diffusionswichtung nur einen untergeordneten Einfluss auf den Signalkontrast hat. Unsere Analyse zeigte eindeutig, dass die Hauptursache für den unterschiedlichen Signalkontrast der Frakturen hauptsächlich durch die Fett- und T_2^* -Wichtung verursacht wird.

Bibliography

- [1] O. Johnell and J. A. Kanis. An estimate of the worldwide prevalence and disability associated with osteoporotic fractures. *Osteoporos Int*, 17(12):1726–1733, Dec 2006.
- [2] L. J. Melton, E. A. Chrischilles, C. Cooper, A. W. Lane, and B. L. Riggs. Perspective. how many women have osteoporosis? *J Bone Miner Res*, 7(9):1005–1010, Sep 1992.
- [3] B. Häussler, H. Gothe, D. Göl, G. Glaeske, L. Pientka, and D. Felsenberg. Epidemiology, treatment and costs of osteoporosis in germany—the boneEVA study. *Osteoporos Int*, 18(1):77–84, Jan 2007.
- [4] B. A. Porter, A. F. Shields, and D. O. Olson. Magnetic resonance imaging of bone marrow disorders. *Radiol Clin North Am*, 24(2):269–289, Jun 1986.
- [5] D. Frager, C. Elkin, M. Swerdlow, and S. Bloch. Subacute osteoporotic compression fracture: misleading magnetic resonance appearance. *Skeletal Radiol*, 17(2):123–126, 1988.
- [6] R. E. Rupp, N. A. Ebraheim, and R. J. Coombs. Magnetic resonance imaging differentiation of compression spine fractures or vertebral lesions caused by osteoporosis or tumor. *Spine (Phila Pa 1976)*, 20(23):2499–503; discussion 2504, 1995.
- [7] W. T. Yuh, C. K. Zachar, T. J. Barloon, Y. Sato, W. J. Sickels, and D. R. Hawes. Vertebral compression fractures: distinction between benign and malignant causes with MR imaging. *Radiology*, 172(1):215–218, 1989.
- [8] L. L. Baker, S. B. Goodman, I. Perkas, B. Lane, and D. R. Enzmann. Benign versus pathologic compression fractures of vertebral bodies: assessment with conventional spin-echo, chemical-shift, and STIR MR imaging. *Radiology*, 174(2):495–502, Feb 1990.
- [9] A. Baur, A. Stäbler, S. Arbogast, H. R. Duerr, R. Bartl, and M. Reiser. Acute osteoporotic and neoplastic vertebral compression fractures: fluid sign at MR imaging. *Radiology*, 225(3):730–735, Dec 2002.
- [10] M. E. Moseley, Y. Cohen, J. Mintorovitch, L. Chileuitt, H. Shimizu, J. Kucharczyk, M. F. Wendland, and P. R. Weinstein. Early detection of regional cerebral ischemia in cats: comparison of diffusion- and T2-weighted MRI and spectroscopy. *Magn Reson Med*, 14(2):330–346, 1990.

- [11] T. A. Huisman. Diffusion-weighted imaging: basic concepts and application in cerebral stroke and head trauma. *Eur Radiol*, 13(10):2283–2297, Oct 2003.
- [12] A. Baur, A. Stäbler, R. Brüning, R. Bartl, A. Krödel, M. Reiser, and M. Deimling. Diffusion-weighted MR imaging of bone marrow: differentiation of benign versus pathologic compression fractures. *Radiology*, 207(2):349–356, 1998.
- [13] E. Spuentrup, A. Buecker, G. Adam, J. J. van Vaals, and R. W. Guenther. Diffusion-weighted MR imaging for differentiation of benign fracture edema and tumor infiltration of the vertebral body. *AJR Am J Roentgenol*, 176(2):351–358, 2001.
- [14] W. M. Byun, S. O. Shin, Y. Chang, S. J. Lee, J. Finsterbusch, and J. Frahm. Diffusion-weighted MR imaging of metastatic disease of the spine: assessment of response to therapy. *AJNR Am J Neuroradiol*, 23(6):906–912, 2002.
- [15] A. M. Herneth, J. Naude, M. Philipp, R. Beichel, S. Trattinig, and H. Imhof. The value of diffusion-weighted MRT in assessing the bone marrow changes in vertebral metastases. *Radiologe*, 40(8):731–736, 2000.
- [16] X. J. Zhou, N. E. Leeds, G. C. McKinnon, and A. J. Kumar. Characterization of benign and metastatic vertebral compression fractures with quantitative diffusion MR imaging. *AJNR Am J Neuroradiol*, 23(1):165–170, 2002.
- [17] J. H M Chan, W. C G Peh, E. Y K Tsui, L. F. Chau, K. K. Cheung, K. B. Chan, M. K. Yuen, E. T H Wong, and K. P C Wong. Acute vertebral body compression fractures: discrimination between benign and malignant causes using apparent diffusion coefficients. *Br J Radiol*, 75(891):207–214, 2002.
- [18] A. Baur, A. Huber, H. R. Dürr, K. Nikolaou, A. Stäbler, M. Deimling, and M. Reiser. Differentiation of benign osteoporotic and neoplastic vertebral compression fractures with a diffusion-weighted, steady-state free precession sequence. *Rofo*, 174(1):70–75, 2002.
- [19] M. Castillo, A. Arbelaez, J. K. Smith, and L. L. Fisher. Diffusion-weighted MR imaging offers no advantage over routine noncontrast MR imaging in the detection of vertebral metastases. *AJNR Am J Neuroradiol*, 21(5):948–953, 2000.
- [20] J. B. Vogler and W. A. Murphy. Bone marrow imaging. *Radiology*, 168:679–693, 1988.
- [21] B. C. Vande Berg, J. Malghem, F. E. Lecouvet, and B. Maldague. Magnetic resonance imaging of the normal bone marrow. *Skeletal Radiol*, 27(9):471–483, 1998.
- [22] J. Pfeilschifter and I. J. Diel. Osteoporosis due to cancer treatment: pathogenesis and management. *J Clin Oncol*, 18(7):1570–1593, 2000.
- [23] W. Berning, J. Freyschmidt, and H. Ostertag. Percutaneous bone biopsy, techniques and indications. *Eur Radiol*, 6(6):875–881, 1996.

- [24] I. S. Fyfe, A. P. Henry, and R. C. Mulholland. Closed vertebral biopsy. *J Bone Joint Surg Br*, 65(2):140–143, 1983.
- [25] N. Ghanem, M. Uhl, I. Brink, O. Schäfer, T. Kelly, E. Moser, and M. Langer. Diagnostic value of MRI in comparison to scintigraphy, PET, MS-CT and PET/CT for the detection of metastases of bone. *Eur J Radiol*, 55(1):41–55, 2005.
- [26] D. G. Mitchell, D. L. Burk, S. Vinitski, and M. D. Rifkin. The biophysical basis of tissue contrast in extracranial MR imaging. *AJR Am J Roentgenol*, 149(4):831–837, 1987.
- [27] F. W. Wehrli, J. R. MacFall, D. Shutts, R. Breger, and R. J. Herfkens. Mechanisms of contrast in NMR imaging. *J Comput Assist Tomogr*, 8(3):369–380, 1984.
- [28] Gary D Fullerton. *Physiologic basis of magnetic relaxation*, chapter 5, pages 36–55. Mosby, St. Louis, 1988.
- [29] A. Biffar, A. Baur-Melnyk, G. P. Schmidt, M. F. Reiser, and O. Dietrich. Multiparameter MRI assessment of normal appearing and diseased vertebral bone marrow. *European Radiology*, article in press, 2010.
- [30] F. W. Wehrli, J. C. Ford, M. Attie, H. Y. Kressel, and F. S. Kaplan. Trabecular structure: preliminary application of MR interferometry. *Radiology*, 179(3):615–621, 1991.
- [31] K. P. Soila, M. Viamonte, and P. M. Starewicz. Chemical shift misregistration effect in magnetic resonance imaging. *Radiology*, 153(3):819–820, 1984.
- [32] P. Lang, R. Fritz, S. Majumdar, M. Vahlensieck, C. Peterfy, and H. K. Genant. Hematopoietic bone marrow in the adult knee: spin-echo and opposed-phase gradient-echo MR imaging. *Skeletal Radiol*, 22(2):95–103, 1993.
- [33] R. T. Constable, R. C. Smith, and J. C. Gore. Signal-to-noise and contrast in fast spin echo (FSE) and inversion recovery FSE imaging. *J Comput Assist Tomogr*, 16(1):41–47, 1992.
- [34] G. H. Sebag and S. G. Moore. Effect of trabecular bone on the appearance of marrow in gradient-echo imaging of the appendicular skeleton. *Radiology*, 174(3 Pt 1):855–859, 1990.
- [35] R. Erlemann, M. F. Reiser, P. E. Peters, P. Vasallo, B. Nommensen, C. R. Kusnierz-Glaz, J. Ritter, and A. Roessner. Musculoskeletal neoplasms: static and dynamic Gd-DTPA-enhanced MR imaging. *Radiology*, 171:767–773, 1989.
- [36] S. G. Moore, G. S. Bisset, M. J. Siegel, and J. S. Donaldson. Pediatric musculoskeletal MR imaging. *Radiology*, 179(2):345–360, 1991.
- [37] A. Saifuddin, K. Bann, J. P. Ridgway, and W. P. Butt. Bone marrow blood supply in gadolinium-enhanced magnetic resonance imaging. *Skeletal Radiol*, 23(6):455–457, 1994.

- [38] C. A. Cuénod, J. D. Laredo, S. Chevet, B. Hamze, J. F. Naouri, X. Chapaux, J. M. Bondeville, and J. M. Tubiana. Acute vertebral collapse due to osteoporosis or malignancy: appearance on unenhanced and gadolinium-enhanced MR images. *Radiology*, 199(2):541–549, 1996.
- [39] S. W. Park, J. H. Lee, S. Ehara, Y. B. Park, S. O. Sung, J. A. Choi, and Y. E. Joo. Single shot fast spin echo diffusion-weighted MR imaging of the spine; is it useful in differentiating malignant metastatic tumor infiltration from benign fracture edema? *Clin Imaging*, 28(2):102–108, 2004.
- [40] G. Savelli, A. Chiti, G. Grasselli, M. Maccauro, M. Rodari, and E. Bombardieri. The role of bone SPET study in diagnosis of single vertebral metastases. *Anticancer Res*, 20(2B):1115–1120, 2000.
- [41] B. J. McNeil. Value of bone scanning in neoplastic disease. *Semin Nucl Med*, 14(4):277–286, 1984.
- [42] R. H. Daffner, A. R. Lupetin, N. Dash, Z. L. Deeb, R. J. Sefczek, and R. L. Schapiro. MRI in the detection of malignant infiltration of bone marrow. *AJR Am J Roentgenol*, 146(2):353–358, 1986.
- [43] R. K. Breger, A. L. Williams, D. L. Daniels, L. F. Czervionke, L. P. Mark, V. M. Haughton, R. A. Papke, and M. Coffey. Contrast enhancement in spinal MR imaging. *AJR Am J Roentgenol*, 153(2):387–391, 1989.
- [44] M. Vahlensieck, P. Lang, K. Seelos, D. Yang-Ho Sze, S. Grampp, and M. Reiser. Musculoskeletal MR imaging: turbo (fast) spin-echo versus conventional spin-echo and gradient-echo imaging at 0.5 tesla. *Skeletal Radiol*, 23(8):607–610, 1994.
- [45] A. Einstein. über die von der molekularkinetischen theorie der wärme geforderte bewegung von in ruhenden flüssigkeiten suspendierten teilchen. *Ann. Phys.*, 322(8):549–560, 1905.
- [46] Marian Smoluchowski. Zur kinetischen Theorie der Brownschen Molekularbewegung und der Suspensionen. *Ann. Phys.*, 326(14):756–780, 1906.
- [47] W. J. C. Orr and J. A. V. Butler. The rate of diffusion of deuterium hydroxide in water. *J. Chem. Soc.*, pages 1273–1277, 1935.
- [48] J. H. Wang, C. V. Robinson, and I. S. Edelman. Self-diffusion and structure of liquid water. iii. measurement of the self-diffusion of liquid water with H₂, H₃ and O₁₈ as tracers. *Journal of the American Chemical Society*, 75(2):466–470, 1953.
- [49] H. Y. Carr and E. M. Purcell. Effects of diffusion on free precession in nuclear magnetic resonance experiments. *Phys. Rev.*, 94(3):630–638, 1954.
- [50] E. L. Hahn. Spin echoes. *Phys. Rev.*, 80(4):580–594, 1950.

- [51] E. O. Stejskal and J. E. Tanner. Spin diffusion measurements: Spin echoes in the presence of a time-dependent field gradient. *The Journal of Chemical Physics*, 42(1):288–292, 1965.
- [52] H. C. Torrey. Bloch equations with diffusion terms. *Phys. Rev.*, 104(3):563–565, 1956.
- [53] A. Abragam. *Principles of Nuclear Magnetism (International Series of Monographs on Physics)*. Oxford University Press, USA, reprint edition, 1983.
- [54] O. Dietrich, A. Biffar, A. Baur-Melnyk, and M. F. Reiser. Technical aspects of MR diffusion imaging of the body. *Eur J Radiol*, 2010.
- [55] K. Merboldt, W. Hänicke, and J. Frahm. Self-diffusion NMR imaging using stimulated echoes. *Journal of Magnetic Resonance (1969)*, 64(3):479 – 486, 1985.
- [56] D. G. Taylor and M. C. Bushell. The spatial mapping of translational diffusion coefficients by the NMR imaging technique. *Phys Med Biol*, 30(4):345–349, Apr 1985.
- [57] D. Le Bihan, E. Breton, D. Lallemand, P. Grenier, E. Cabanis, and M. Laval-Jeantet. MR imaging of intravoxel incoherent motions: application to diffusion and perfusion in neurologic disorders. *Radiology*, 161(2):401–407, 1986.
- [58] R. Turner, D. Le Bihan, J. Maier, R. Vavrek, L. K. Hedges, and J. Pekar. Echo-planar imaging of intravoxel incoherent motion. *Radiology*, 177(2):407–414, Nov 1990.
- [59] D. G. Norris, P. Börnert, T. Reese, and D. Leibfritz. On the application of ultra-fast RARE experiments. *Magn Reson Med*, 27(1):142–164, 1992.
- [60] K. O. Lövblad, P. M. Jakob, Q. Chen, A. E. Baird, G. Schlaug, S. Warach, and R. R. Edelman. Turbo spin-echo diffusion-weighted MR of ischemic stroke. *AJNR Am J Neuroradiol*, 19(2):201–8; discussion 209, 1998.
- [61] K. L. Miller, B. A. Hargreaves, G. E. Gold, and J. M. Pauly. Steady-state diffusion-weighted imaging of in vivo knee cartilage. *Magn Reson Med*, 51(2):394–398, 2004.
- [62] R. B. Buxton. The diffusion sensitivity of fast steady-state free precession imaging. *Magnetic Resonance in Medicine*, 29(2):235–243, 1993.
- [63] S. C. L. Deoni, T. M. Peters, and B. K. Rutt. Quantitative diffusion imaging with steady-state free precession. *Magn Reson Med*, 51(2):428–433, 2004.
- [64] A. E. Baird and S. Warach. Magnetic resonance imaging of acute stroke. *J Cereb Blood Flow Metab*, 18(6):583–609, 1998.
- [65] J. Kucharczyk, J. Mintorovitch, H. S. Asgari, and M. Moseley. Diffusion/perfusion MR imaging of acute cerebral ischemia. *Magn Reson Med*, 19(2):311–315, 1991.
- [66] D. C. Tong, M. A. Yenari, G. W. Albers, M. O'Brien, M. P. Marks, and M. E. Moseley. Correlation of perfusion- and diffusion-weighted MRI with NIHSS score in acute (<6.5 hour) ischemic stroke. *Neurology*, 50(4):864–870, 1998.

- [67] J. Zhong, O. A. Petroff, J. W. Prichard, and J. C. Gore. Changes in water diffusion and relaxation properties of rat cerebrum during status epilepticus. *Magn Reson Med*, 30(2):241–246, 1993.
- [68] K. Takano, L. L. Latour, J. E. Formato, R. A. Carano, K. G. Helmer, Y. Hasegawa, C. H. Sotak, and M. Fisher. The role of spreading depression in focal ischemia evaluated by diffusion mapping. *Ann Neurol*, 39(3):308–318, 1996.
- [69] H. Benveniste, L. W. Hedlund, and G. A. Johnson. Mechanism of detection of acute cerebral ischemia in rats by diffusion-weighted magnetic resonance microscopy. *Stroke*, 23(5):746–754, 1992.
- [70] T. Niendorf, R. M. Dijkhuizen, D. G. Norris, M. van Lookeren Campagne, and K. Nicolay. Biexponential diffusion attenuation in various states of brain tissue: implications for diffusion-weighted imaging. *Magn Reson Med*, 36(6):847–857, 1996.
- [71] D. G. Norris, T. Niendorf, and D. Leibfritz. Health and infarcted brain tissues studied at short diffusion times: the origins of apparent restriction and the reduction in apparent diffusion coefficient. *NMR Biomed*, 7(7):304–310, 1994.
- [72] J. A. Goodman, J. H. Ackerman, and J. J. Neil. $C_s + ADC$ in rat brain decreases markedly at death. *Magn Reson Med*, 59(1):65–72, 2008.
- [73] A. Schwarcz, P. Bogner, P. Meric, J. L. Correze, Z. Berente, J. Pál, F. Gallyas, T. Doczi, B. Gillet, and J. C. Beloeil. The existence of biexponential signal decay in magnetic resonance diffusion-weighted imaging appears to be independent of compartmentalization. *Magn Reson Med*, 51(2):278–285, 2004.
- [74] T. Q. Duong, J. J. Ackerman, H. S. Ying, and J. J. Neil. Evaluation of extra- and intracellular apparent diffusion in normal and globally ischemic rat brain via ^{19}F NMR. *Magn Reson Med*, 40(1):1–13, 1998.
- [75] M. A. Jacobs, R. Ouwerkerk, K. Petrowski, and K. J. Macura. Diffusion-weighted imaging with apparent diffusion coefficient mapping and spectroscopy in prostate cancer. *Top Magn Reson Imaging*, 19(6):261–272, 2008.
- [76] S. Sinha and U. Sinha. Functional magnetic resonance of human breast tumors: diffusion and perfusion imaging. *Ann N Y Acad Sci*, 980:95–115, 2002.
- [77] B. Taouli and D. M. Koh. Diffusion-weighted MR imaging of the liver. *Radiology*, 254(1):47–66, 2010.
- [78] S. Kim, M. Naik, E. Sigmund, and B. Taouli. Diffusion-weighted MR imaging of the kidneys and the urinary tract. *Magn Reson Imaging Clin N Am*, 16(4):585–96, vii–viii, 2008.
- [79] A. M. Herneth, H. Ringl, M. Memarsadeghi, B. Fueger, K. M. Friedrich, C. Krestan, and H. Imhof. Diffusion weighted imaging in osteoradiology. *Top Magn Reson Imaging*, 18(3):203–212, 2007.

- [80] T. Takahara, Y. Imai, T. Yamashita, S. Yasuda, S. Nasu, and M. Van Cauteren. Diffusion weighted whole body imaging with background body signal suppression (DWIBS): technical improvement using free breathing, STIR and high resolution 3D display. *Radiat Med*, 22(4):275–282, 2004.
- [81] T. C. Kwee, T. Takahara, R. Ochiai, R. A. J. Nievelstein, and P. R. Luijten. Diffusion-weighted whole-body imaging with background body signal suppression (DWIBS): features and potential applications in oncology. *Eur Radiol*, 18(9):1937–1952, 2008.
- [82] D. Koh, T. Takahara, Y. Imai, and D. J. Collins. Practical aspects of assessing tumors using clinical diffusion-weighted imaging in the body. *Magn Reson Med Sci*, 6(4):211–224, 2007.
- [83] P. Mürtz, C. Krautmacher, F. Träber, J. Gieseke, H. H. Schild, and W. A. Willinek. Diffusion-weighted whole-body MR imaging with background body signal suppression: a feasibility study at 3.0 tesla. *Eur Radiol*, 17(12):3031–3037, 2007.
- [84] A. Gutzeit, A. Dört, J. M. Froehlich, B. P. Eckhardt, A. Meili, P. Scherr, D. T. Schmid, N. Graf, C. A. Von Weymarn, E. M. M. Willemse, and C. A. Binkert. Comparison of diffusion-weighted whole body MRI and skeletal scintigraphy for the detection of bone metastases in patients with prostate or breast carcinoma. *Skeletal Radiol*, 39(4):333–343, 2010.
- [85] T. Hackländer, C. Scharwächter, R. Golz, and H. Mertens. Value of diffusion-weighted imaging for diagnosing vertebral metastases due to prostate cancer in comparison to other primary tumors. *Rofo*, 178(4):416–424, 2006.
- [86] M. Yasumoto, Y. Nonomura, R. Yoshimura, K. Haraguchi, S. Ito, I. Ohashi, and H. Shibuya. MR detection of iliac bone marrow involvement by malignant lymphoma with various MR sequences including diffusion-weighted echo-planar imaging. *Skeletal Radiol*, 31(5):263–269, 2002.
- [87] A. Baur, A. Huber, B. Ertl-Wagner, R. Dürr, S. Zysk, S. Arbogast, M. Deimling, and M. F. Reiser. Diagnostic value of increased diffusion weighting of a steady-state free precession sequence for differentiating acute benign osteoporotic fractures from pathologic vertebral compression fractures. *AJNR Am J Neuroradiol*, 22(2):366–372, 2001.
- [88] O. Dietrich, A. Biffar, M. F. Reiser, and A. Baur-Melnyk. Diffusion-weighted imaging of bone marrow. *Semin Musculoskelet Radiol*, 13(2):134–144, 2009.
- [89] R. Mills. Self-diffusion in normal and heavy water in the range 1–45 deg. *The Journal of Physical Chemistry*, 77(5):685–688, 1973.
- [90] A. Lehnert, J. Machann, G. Helms, C. D. Claussen, and F. Schick. Diffusion characteristics of large molecules assessed by proton MRS on a whole-body MR system. *Magn Reson Imaging*, 22(1):39–46, 2004.

- [91] Z. Q. Ababneh, H. Beloeil, C. B. Berde, A. M. Ababneh, S. E. Maier, and R. V. Mulkern. In vivo lipid diffusion coefficient measurements in rat bone marrow. *Magn Reson Imaging*, 27(6):859–864, 2009.
- [92] R. Ward, S. Caruthers, C. Yablon, M. Blake, M. DiMasi, and S. Eustace. Analysis of diffusion changes in posttraumatic bone marrow using navigator-corrected diffusion gradients. *AJR Am J Roentgenol*, 174(3):731–734, 2000.
- [93] O. Dietrich, A. Herlihy, W. R. Dannels, J. Fiebach, S. Heiland, J. V. Hajnal, and K. Sartor. Diffusion-weighted imaging of the spine using radial k-space trajectories. *MAGMA*, 12(1):23–31, 2001.
- [94] R. Bammer, A. M. Herneth, S. E. Maier, K. Butts, R. W. Prokesch, H. M. Do, S. W. Atlas, and M. E. Moseley. Line scan diffusion imaging of the spine. *AJNR Am J Neuroradiol*, 24(1):5–12, 2003.
- [95] A. Y. Oner, T. Tali, F. Celikyay, A. Celik, and P. Le Roux. Diffusion-weighted imaging of the spine with a non-carr-purcell-meiboom-gill single-shot fast spin-echo sequence: initial experience. *AJNR Am J Neuroradiol*, 28(3):575–580, 2007.
- [96] J. G. Raya, O. Dietrich, C. Birkenmaier, J. Sommer, M. F. Reiser, and A. Baur-Melnyk. Feasibility of a RARE-based sequence for quantitative diffusion-weighted MRI of the spine. *Eur Radiol*, 17(11):2872–2879, 2007.
- [97] W. M. Byun, H. W. Jang, S. W. Kim, S. H. Jang, S. H. Ahn, and M. W. Ahn. Diffusion-weighted magnetic resonance imaging of sacral insufficiency fractures: comparison with metastases of the sacrum. *Spine (Phila Pa 1976)*, 32(26):E820–E824, 2007.
- [98] A. M. Herneth, M. O. Philipp, J. Naude, M. Funovics, R. R. Beichel, R. Bammer, and H. Imhof. Vertebral metastases: assessment with apparent diffusion coefficient. *Radiology*, 225(3):889–894, 2002.
- [99] D. K. W. Yeung, S. Y. S. Wong, J. F. Griffith, and E. M. C. Lau. Bone marrow diffusion in osteoporosis: evaluation with quantitative MR diffusion imaging. *J Magn Reson Imaging*, 19(2):222–228, 2004.
- [100] M. H. Pui, A. Mitha, W. I. D. Rae, and P. Corr. Diffusion-weighted magnetic resonance imaging of spinal infection and malignancy. *J Neuroimaging*, 15(2):164–170, 2005.
- [101] H. G. Hatipoglu, A. Selvi, D. Ciliz, and E. Yuksel. Quantitative and diffusion MR imaging as a new method to assess osteoporosis. *AJNR Am J Neuroradiol*, 28(10):1934–1937, 2007.
- [102] T. Sugimoto, N. Tanigawa, K. Ikeda, N. Ohmura, M. Maehara, S. Kariya, H. Kojima, A. Komemushi, S. K. Ha-Kawa, Y. Saito, A. Tajika, T. Kinoshita, and S. Sawada. Diffusion-weighted imaging for predicting new compression fractures following percutaneous vertebroplasty. *Acta Radiol*, 49(4):419–426, 2008.

- [103] M. Maeda, H. Sakuma, S. E. Maier, and K. Takeda. Quantitative assessment of diffusion abnormalities in benign and malignant vertebral compression fractures by line scan diffusion-weighted imaging. *AJR Am J Roentgenol*, 181(5):1203–1209, 2003.
- [104] E. Balliu, J. C. Vilanova, I. Peláez, J. Puig, S. Remollo, C. Barceló, J. Barceló, and S. Pedraza. Diagnostic value of apparent diffusion coefficients to differentiate benign from malignant vertebral bone marrow lesions. *Eur J Radiol*, 69(3):560–566, 2009.
- [105] D. Le Bihan. Intravoxel incoherent motion imaging using steady-state free precession. *Magnetic Resonance in Medicine*, 7(3):341–351, 1988.
- [106] S. M. Kealey, T. Aho, D. Delong, D. P. Barboriak, J. M. Provenzale, and J. D. Eastwood. Assessment of apparent diffusion coefficient in normal and degenerated intervertebral lumbar disks: initial experience. *Radiology*, 235(2):569–574, 2005.
- [107] L. Kerttula, M. Kurunlahti, J. Jauhiainen, A. Koivula, J. Oikarinen, and O. Tervonen. Apparent diffusion coefficients and T2 relaxation time measurements to evaluate disc degeneration. a quantitative MR study of young patients with previous vertebral fracture. *Acta Radiol*, 42(6):585–591, 2001.
- [108] R. Arun, B. J. C. Freeman, B. E. Scammell, D. S. McNally, E. Cox, and P. Gowland. 2009 ISSLS prize winner: What influence does sustained mechanical load have on diffusion in the human intervertebral disc?: an in vivo study using serial postcontrast magnetic resonance imaging. *Spine (Phila Pa 1976)*, 34(21):2324–2337, 2009.
- [109] O. Dietrich, J. G. Raya, J. Sommer, M. Deimling, M. F. Reiser, and A. Baur-Melnyk. A comparative evaluation of a RARE-based single-shot pulse sequence for diffusion-weighted MRI of musculoskeletal soft-tissue tumors. *Eur Radiol*, 15(4):772–783, 2005.
- [110] H. Einarsdóttir, M. Karlsson, J. Wejde, and H. C. F. Bauer. Diffusion-weighted MRI of soft tissue tumours. *Eur Radiol*, 14(6):959–963, 2004.
- [111] A. Haase, J. Frahm, D. Matthaei, W. Hänicke, and K. D. Merboldt. FLASH imaging. rapid NMR imaging using low flip-angle pulses. *Journal of Magnetic Resonance (1969)*, 67(2):258 – 266, 1986.
- [112] F. W. Wehrli, T. G. Perkins, A. Shimakawa, and F. Roberts. Chemical shift-induced amplitude modulations in images obtained with gradient refocusing. *Magn Reson Imaging*, 5(2):157–158, 1987.
- [113] A. P. Crawley, M. L. Wood, and R. M. Henkelman. Elimination of transverse coherences in FLASH MRI. *Magn Reson Med*, 8(3):248–260, 1988.
- [114] Y. Zur, M. L. Wood, and L. J. Neuringer. Spoiling of transverse magnetization in steady-state sequences. *Magn Reson Med*, 21(2):251–263, 1991.
- [115] H. Y. Carr. Steady-state free precession in nuclear magnetic resonance. *Phys. Rev.*, 112(5):1693–1701, 1958.

- [116] R. R. Ernst and W. A. Anderson. Application of fourier transform spectroscopy to magnetic resonance. *Review of Scientific Instruments*, 37(1):93–102, 1966.
- [117] R. Freeman and H. D. W. Hill. Phase and intensity anomalies in fourier transform NMR. *Journal of Magnetic Resonance (1969)*, 4(3):366 – 383, 1971.
- [118] Y. Zur, S. Stokar, and P. Bendel. An analysis of fast imaging sequences with steady-state transverse magnetization refocusing. *Magn Reson Med*, 6(2):175–193, 1988.
- [119] M. L. Gyngell. The steady-state signals in short-repetition-time sequences. *Journal of Magnetic Resonance (1969)*, 81(3):474 – 483, 1989.
- [120] W. Hänicke and H. U. Vogel. An analytical solution for the SSFP signal in MRI. *Magn Reson Med*, 49(4):771–775, 2003.
- [121] H. Bruder, H. Fischer, R. Graumann, and M. Deimling. A new steady-state imaging sequence for simultaneous acquisition of two MR images with clearly different contrasts. *Magn Reson Med*, 7(1):35–42, 1988.
- [122] A. Oppelt, R. Graumann, H. Barfuss, H. Fischer, W. Hartl, and W. Shajor. FISP: Eine neue schnelle Puls-Sequenz für die Kernspintomographie. *Electromedica*, 54:15–18, 1986.
- [123] K. Scheffler and S. Lehnhardt. Principles and applications of balanced SSFP techniques. *Eur Radiol*, 13(11):2409–2418, 2003.
- [124] M. E. Haacke, R. W. Brown, M. R. Thompson, and R. Venkatesan. *Magnetic Resonance Imaging: Physical Principles and Sequence Design*. Wiley-Liss, 1999.
- [125] R. Kaiser, E. Bartholdi, and R. R. Ernst. Diffusion and field-gradient effects in NMR fourier spectroscopy. *The Journal of Chemical Physics*, 60(8):2966–2979, 1974.
- [126] K. Merboldt, W. Hänicke, M. L. Gyngell, J. Frahm, and H. Bruhn. Rapid NMR imaging of molecular self-diffusion using a modified CE-FAST sequence. *Journal of Magnetic Resonance (1969)*, 82(1):115 – 121, 1989.
- [127] D. Le Bihan, R. Turner, and J. R. MacFall. Effects of intravoxel incoherent motions (IVIM) in steady-state free precession (SSFP) imaging: application to molecular diffusion imaging. *Magn Reson Med*, 10(3):324–337, 1989.
- [128] E. X. Wu and R. B. Buxton. Effect of diffusion on the steady-state magnetization with pulsed field gradients. *Journal of Magnetic Resonance (1969)*, 90(2):243 – 253, 1990.
- [129] C. E. Carney, S. T. Wong, and S. Patz. Analytical solution and verification of diffusion effect in SSFP. *Magn Reson Med*, 19(2):240–246, 1991.
- [130] D. E. Woessner. Effects of diffusion in nuclear magnetic resonance spin-echo experiments. *The Journal of Chemical Physics*, 34(6):2057–2061, 1961.

- [131] K. Scheffler. A pictorial description of steady-states in rapid magnetic resonance imaging. *Concepts in Magnetic Resonance*, 11(5):291–304, 1999.
- [132] P. A. Bottomley, T. H. Foster, R. E. Argersinger, and L. M. Pfeifer. A review of normal tissue hydrogen NMR relaxation times and relaxation mechanisms from 1-100 MHz: dependence on tissue type, NMR frequency, temperature, species, excision, and age. *Med Phys*, 11(4):425–448, 1984.
- [133] H. H. Hu and K. S. Nayak. Change in the proton T1 of fat and water in mixture. *Magn Reson Med*, 63(2):494–501, 2010.
- [134] F. Träber, W. Block, G. Layer, G. Bräucker, J. Gieseke, S. Kretzer, I. Hasan, and H. H. Schild. Determination of 1H relaxation times of water in human bone marrow by fat-suppressed turbo spin echo in comparison to MR spectroscopic methods. *J Magn Reson Imaging*, 6(3):541–548, 1996.
- [135] G. E. Gold, E. Han, J. Stainsby, G. Wright, J. Brittain, and C. Beaulieu. Musculoskeletal MRI at 3.0 T: relaxation times and image contrast. *AJR Am J Roentgenol*, 183(2):343–351, Aug 2004.
- [136] K. Sugimura, K. Yamasaki, H. Kitagaki, Y. Tanaka, and M. Kono. Bone marrow diseases of the spine: differentiation with T1 and T2 relaxation times in MR imaging. *Radiology*, 165(2):541–544, Nov 1987.
- [137] M. Ito, K. Hayashi, M. Uetani, Y. Kawahara, M. Ohki, M. Yamada, H. Kitamori, M. Noguchi, and M. Ito. Bone mineral and other bone components in vertebrae evaluated by QCT and MRI. *Skeletal Radiol*, 22(2):109–113, 1993.
- [138] C. A. Davis, H. K. Genant, and J. S. Dunham. The effects of bone on proton NMR relaxation times of surrounding liquids. *Invest Radiol*, 21(6):472–477, Jun 1986.
- [139] S. Majumdar, D. Thomasson, A. Shimakawa, and H. K. Genant. Quantitation of the susceptibility difference between trabecular bone and bone marrow: experimental studies. *Magn Reson Med*, 22(1):111–127, Nov 1991.
- [140] P. F. Beattie, P. S. Morgan, and D. Peters. Diffusion-weighted magnetic resonance imaging of normal and degenerative lumbar intervertebral discs: a new method to potentially quantify the physiologic effect of physical therapy intervention. *J Orthop Sports Phys Ther*, 38(2):42–49, Feb 2008.
- [141] W. T. Dixon. Simple proton spectroscopic imaging. *Radiology*, 153(1):189–194, Oct 1984.
- [142] D. G. Disler, T. R. McCauley, L. M. Ratner, C. D. Kesack, and J. A. Cooper. In-phase and out-of-phase MR imaging of bone marrow: prediction of neoplasia based on the detection of coexistent fat and water. *AJR Am J Roentgenol*, 169(5):1439–1447, Nov 1997.

- [143] V. Zampa, M. Cosottini, C. Michelassi, S. Ortori, L. Bruschini, and C. Bartolozzi. Value of opposed-phase gradient-echo technique in distinguishing between benign and malignant vertebral lesions. *Eur Radiol*, 12(7):1811–1818, Jul 2002.
- [144] D. C. Zajick, W. B. Morrison, M. E. Schweitzer, J. A. Parellada, and J. A. Carrino. Benign and malignant processes: normal values and differentiation with chemical shift MR imaging in vertebral marrow. *Radiology*, 237(2):590–596, Nov 2005.
- [145] B. D. Coombs, J. Szumowski, and W. Coshov. Two-point dixon technique for water-fat signal decomposition with B0 inhomogeneity correction. *Magn Reson Med*, 38(6):884–889, Dec 1997.
- [146] A. Biffar, G. Schmidt, A. Baur-Melnyk, M. F. Reiser, and O. Dietrich. Assessment of benign and malignant vertebral fractures based on the measurement of the fat-fraction. *Proceedings 18th Scientific Meeting ISMRM, Stockholm, Sweden*, 18:#3208, 2010.
- [147] J. Szumowski, W. R. Coshov, F. Li, and S. F. Quinn. Phase unwrapping in the three-point dixon method for fat suppression MR imaging. *Radiology*, 192(2):555–561, Aug 1994.
- [148] J. F. Griffith, D. K. Yeung, G. E. Antonio, S. Y. Wong, T. C. Kwok, J. Woo, and P. C. Leung. Vertebral marrow fat content and diffusion and perfusion indexes in women with varying bone density: MR evaluation. *Radiology*, 241:831–838, 2006.
- [149] J. F. Griffith, D. K. Yeung, G. E. Antonio, F. K. Lee, A. W. Hong, S. Y. Wong, E. M. Lau, and P. C. Leung. Vertebral bone mineral density, marrow perfusion, and fat content in healthy men and men with osteoporosis: dynamic contrast-enhanced MR imaging and MR spectroscopy. *Radiology*, 236:945–951, 2005.
- [150] D. Schellinger, C. S. Lin, J. Lim, H. G. Hatipoglu, J. C. Pezzullo, and A. J. Singer. Bone marrow fat and bone mineral density on proton mr spectroscopy and dual-energy x-ray absorptiometry: their ratio as a new indicator of bone weakening. *AJR Am J Roentgenol*, 183(6):1761–1765, Dec 2004.
- [151] D. Schellinger, C. S. Lin, D. Fertikh, J. S. Lee, W. C. Lauerman, F. Henderson, and B. Davis. Normal lumbar vertebrae: anatomic, age, and sex variance in subjects at proton MR spectroscopy—initial experience. *Radiology*, 215(3):910–916, Jun 2000.
- [152] R. Abanoz, B. Hakyemez, and M. Parlak. Diffusion-weighted imaging of acute vertebral compression: Differential diagnosis of benign versus malignant pathologic fractures. *Tani Girisim Radyol*, 9(2):176–183, 2003.

Curriculum Vitae

Persönliche Daten

Name: Andreas Ferdinand Biffar
Geburtsdatum: 16.06.1981
Geburtsort: Heidelberg
Staatsangehörigkeit: Deutsch

Promotion

04/2007 – 04/2010 Wissenschaftlicher Mitarbeiter am Institut für Klinische Radiologie Universitätsklinikum der LMU München, Großhadern
Thema "Quantitative Analyse der diffusionsgewichteten MRT-Bildgebung in der Wirbelsäule"

Studium

VWL 04/2007 – 01/2010 im Rahmen des wirtschaftswissenschaftlichen Zusatzstudienganges für Naturwissenschaftler
Hochschule Fernuniversität Hagen
Fachrichtung Statistik
Diplomarbeit "Optionspreisbewertung mit Hilfe von Pfadintegralen"
Abschlussnote 2,0

Physik	10/2000 – 09/2006
Hochschule	Technische Universität München
Fachrichtung	Allgemeine Physik (Astroteilchenphysik)
Diplomarbeit	"Thermal interactions in inflationary quintessence models"
Abschlussnote	1,0

Wissenschaftliche Veröffentlichungen

- 06/2009 Dietrich O, **Biffar A**, Reiser MF, Baur-Melnyk A
Diffusion-weighted imaging of bone marrow
 Seminars in Musculoskeletal Radiology 2009 Jun;13(2):134-44.
- 09/2009 Sourbron S, Heilmann M, **Biffar A** et al.
Bolus-tracking with simultaneous T1- and T2-measurement*
 Magnetic Resonance in Medicine 2009 Sep;62(3):672-81.
- 03/2010 Dietrich O, **Biffar A**, Baur-Melnyk A, Reiser MF
Technical Aspects of MR diffusion imaging of the body
 European Journal of Radiology, published online ahead of print
- 04/2010 **Biffar A**, Dietrich O, Sourbron S et al.
Diffusion and Perfusion imaging of bone marrow
 European Journal of Radiology, published online ahead of print
- ??/2010 **Biffar A**, Sourbron S, Schmidt G et al.
Measurement of Perfusion and Permeability from Dynamic-Contrast-Enhanced MR Imaging in Normal and Pathological Vertebral Bone Marrow
 Magnetic Resonance in Medicine, published online ahead of print
- ??/2010 **Biffar A**, Baur-Melnyk A, Schmidt G et al.
Multiparameter MRI Assessment of Normal Appearing and Diseased Vertebral Bone Marrow
 European Radiology, in press
- ??/2010 **Biffar A**, Sourbron S, Dietrich O et al.
Combined Diffusion-weighted and Dynamic Contrast-Enhanced Imaging

of Patients with Acute Osteoporotic vertebral fractures
European Journal of Radiology, in press

- ??/2010 **Biffar A**, Schmidt G, Sourbron S et al.
Quantitative Analysis of vertebral bone marrow perfusion using dynamic-contrast-enhanced MRI: Initial results in osteoporotic patients with acute vertebral fracture
European Radiology, in press
- ??/2010 Haneder S, Attenberger U, **Biffar A** et al.
Gadofosveset: Parameter Optimization for Steady-state Imaging of the Thoracic and Abdominal Vasculature
Investigative Radiology
-

Wissenschaftliche Vorträge

- 02/2009 Quantitative DCE-MRI of The Spine
 ISMRM Workshop on Advances in Musculoskeletal Magnetic Resonance Imaging
 San Francisco, CA, USA
- 10/2009 I. Multiparametric assessment of healthy and diseased vertebral bone marrow
 II. DCE-MRI in vertebral bone marrow - a fully quantitative approach
 III. Quantitative DCE-MRI at high temporal resolution in healthy and pathological vertebral bone marrow
 ESMRMB 2009
 Antalya, Turkey
- 12/2009 Quantitative Dynamic Contrast-enhanced MRI in Vertebral Bone Marrow
 RSNA 2009
 Chicago, IL, USA

Danksagung

An erster Stelle möchte ich mich bei Herrn Prof. Maximilian Reiser dafür bedanken, dass er mir die Möglichkeit gegeben hat am *Institut für Klinische Radiologie* wissenschaftlich tätig zu sein und für die fortwährende Unterstützung während der Durchführung meiner Doktorarbeit. Während meiner Zeit als Promotionsstudent in Großhadern empfand ich insbesondere das interdisziplinäre Umfeld im Rahmen der Zusammenarbeit mit meinen medizinischen Kollegen und die sich daraus ergebenden breit gefächerten wissenschaftlichen Herausforderungen als besonders motivierend und inspirierend.

Ganz besonders möchte ich mich bei meinem wissenschaftlichen Betreuer Herrn Dr. Olaf Dietrich bedanken. Dank seiner ausgezeichneten Kenntnisse im Bereich der MR-Physik konnte ich bei vielen Fragestellungen in großem Maße von seinen Ratschlägen und Ideen profitieren. Seine unermüdliche und stets zielgerichtete Unterstützung war für das Gelingen meiner Doktorarbeit von entscheidender Bedeutung.

Mein besonderer Dank gilt auch Frau PD Dr. Andrea Baur-Melnyk für die medizinische Betreuung meiner Forschung. Ihre medizinische Expertise und die interessanten Diskussionen über Fragen im Bereich der medizinischen Bildgebung waren eine große Bereicherung bei der Erstellung dieser Arbeit. Darüber hinaus möchte ich mich herzlich bei Herrn Dr. Steven Sourbron und Herrn Dr. José Raya für ihre Betreuung im Bereich der medizinischen Bildverarbeitung bedanken. Bei Herrn Dr. Gerwin Schmidt bedanke ich mich für die Zusammenarbeit bei Patientenuntersuchungen und der Erstellung von wissenschaftlichen Veröffentlichungen.

Ich möchte mich bei Herrn Dr. Michael Peller für seine Unterstützung bei fachlichen und insbesondere auch bei administrativen Problemen bedanken. Bei allen bereits erwähnten Personen und darüber hinaus bei meinen Kollegen aus der Physik-Gruppe (Felix, Linus, Lucianna, Michi) bedanke ich mich für die angenehme Arbeitsatmosphäre und die unvergesslichen Erfahrungen während unserer Reisen zu wissenschaftlichen Kongressen. Dieser Dank gilt ebenfalls allen Radiologen mit denen ich während meiner Promotion zusammenarbeitete, insbesondere meinen Bürokollegen

Dr. Daniel Theisen, Dr. Torleif Sandner und Dr. Natalie Wöhrle.

Neben meiner Arbeitszeit hatte ich bisweilen auch Zeit die Freuden des Lebens in einer so wunderschönen Stadt wie München genießen zu dürfen. Ich danke all meinen Freunden für die unvergesslichen Erfahrungen und die gemeinsame Zeit die wir miteinander verbracht haben, die den perfekten Ausgleich zu meinem Arbeitsalltag bot. Besonders möchte ich mich bei Dr. Benjamin Tuschy für seine Freundschaft und seine Geduld bei der Verbesserung meines laienhaften medizinischen Wissens bedanken. Bei Dr. Florian Hahn-Woernle bedanke ich mich für die gegenseitige Motivation und Unterstützung, die es uns beiden erlaubte neben der Promotion ein zweites Studium zu absolvieren, ohne dabei gänzlich auf die angenehmen Seiten des Lebens verzichten zu müssen. Ein ganz herzlicher Dank gilt auch meinen Nachbarn (Milla, Steffi und Felix Wunderle), die sowohl an meinem kulinarischen als auch seelischen Wohlergehen großen Anteil hatten.

Zuletzt möchte ich mich bei meinen Eltern, meiner Großmutter und dem Rest meiner Familie für all Ihre Unterstützung und Zuneigung vor allem in den schweren Momenten während der Zeit meiner Doktorarbeit bedanken. Meiner Schwester Lucia danke ich darüber hinaus für das Korrekturlesen meiner Dissertation.